LBL-25456 c.2

Lawrence Berkeley Laboratory
UNIVERSITY OF CALIFORNIA

Engineering Division

RECEIVED
LAWRENCE
BERKELEY LABORATORY

JAN 25 1989

LIBRARY AND
DOCUMENTS SECTION

Characterization and Applications of Neutron Transmutation Doped Germanium

I.-S. Park
(Ph.D. Thesis)

May 1988

TWO-WEEK LOAN COPY
This is a Library Circulating Copy
which may be borrowed for two weeks.

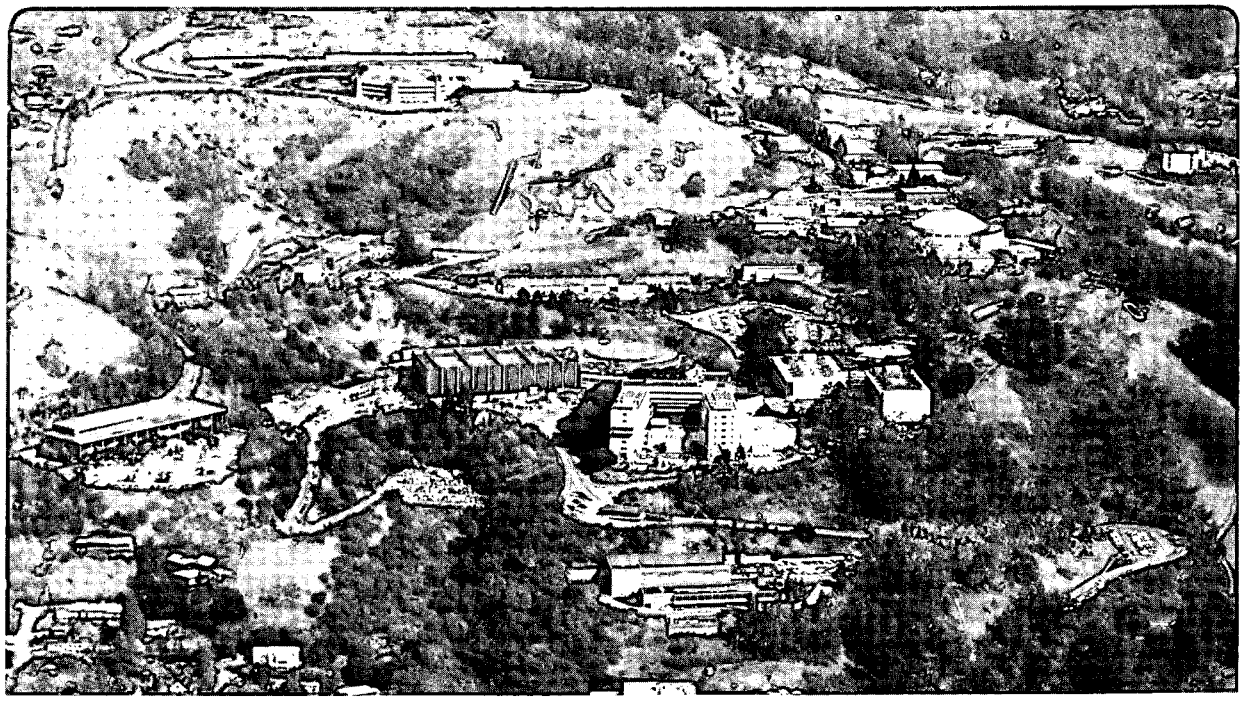

Prepared for the U.S. Department of Energy under Contract Number DE-AC03-76SF00098.

LBL-25456 c.2

DISCLAIMER

This document was prepared as an account of work sponsored by the United States Government. While this document is believed to contain correct information, neither the United States Government nor any agency thereof, nor the Regents of the University of California, nor any of their employees, makes any warranty, express or implied, or assumes any legal responsibility for the accuracy, completeness, or usefulness of any information, apparatus, product, or process disclosed, or represents that its use would not infringe privately owned rights. Reference herein to any specific commercial product, process, or service by its trade name, trademark, manufacturer, or otherwise, does not necessarily constitute or imply its endorsement, recommendation, or favoring by the United States Government or any agency thereof, or the Regents of the University of California. The views and opinions of authors expressed herein do not necessarily state or reflect those of the United States Government or any agency thereof or the Regents of the University of California.

LBL-25456

Characterization and Applications of Neutron Transmutation Doped Germanium

I.-S. Park
(Ph.D. Thesis)

Engineering Division
Lawrence Berkeley Laboratory
1 Cyclotron Road
Berkeley, California 94720
USA

May 1988

Characterization and Applications of Neutron Transmutation Doped Germanium

In-Shik Park

Abstract

Thermal neutron irradiation of germanium leads to gallium acceptors, arsenic and selenium donors, as well as radiation defects. Unlike other neutron transmutation doped (NTD) semiconductors in which only donor impurities are introduced, NTD germanium contains both types of dopant impurities in the ratio of acceptor:donor = 3:1.

Radiation defects and the evolution of each impurity as a function of time in NTD germanium were investigated by Hall effect measurements and infrared absorption spectroscopy. The presence of radiation defects in an unannealed NTD germanium sample was clearly shown by measuring the net carrier concentration of annealed and unannealed samples as a function of time after neutron irradiation. Most of the radiation defects were removed by annealing above 400°C for 1 hr. Using IR spectroscopy with bandedge light illumination, it was shown that transmutation-produced gallium acceptors were electrically active without annealing after NTD, while arsenic donors were not. Further evidence showed that group V donors in irradiated germanium formed complexes with vacancies. These complexes were formed between substitutional donors and vacancies as shown by IR spectroscopy on neurtron-irradiated, phosphorus-doped germanium. It was concluded

that vacancies diffuse to the substitutional donor sites to form complexes. The possibility of the complex formation between interstitial donors (arsenic) and vacancies was not ruled out. Deep level defects in NTD germanium were studied after high temperature annealing (> 200°C) by deep level transient spectroscopy. Results showed that although the concentrations were very small ($< 10^{11}$ cm^{-3}), two hole traps at $E_v + 0.22$ eV and at $E_v +$ 0.30 eV were present even after annealing at 500°C. In neutron irradiated n-type germanium, two electron traps were also observed by DLTS after annealing at 700°C. These electron traps were located at $E_c - 0.20$ eV and at $E_c - 0.35$ eV. Again the concentration of these traps was less than 10^{11} cm^{-3}. High resolution transmission electron micrographs of neutron irradiated and unannealed germanium samples showed disordered regions. The diameter of the disordered regions was estimated to be ~ 100 atomic spacings.

NTD germanium has been used as a material for cryogenic bolometers because of its unique characteristics: uniform doping and fixed compensation ratio. Bolometers made of NTD germanium have shown excellent performance in many areas. Our data shows clearly that the resistivity depends on the inverse of the square root of the absolute temperature in the hopping conduction region in accordance with Efros' theory of hopping conduction. NTD germanium was also used in the development of FIR heterodyne mixers. Detectors have been evaluated in an intermediate frequency range of up to 100 MHz and have shown bandwidths of up to 60 MHz. The dependence of bandwidth on bias is discussed and compared with theoretical expectations. From the

dependence of bandwidth on compensating impurity concentraion, a recombination cross section of 3.2×10^{-13} cm^2 was obtained.

Acknowledgements

I would like to express my heartfelt thanks to my advisor, Professor Eugene Haller. His guidence has been invaluable to me throughout this thesis work, and nothing could have been done without his careful supervision. I would also like to thank Professor E. Weber and Professor B. Sadoulet for their comments on this work.

It has been wonderful to work in this group and I am indebted to many of the students and former students who I have worked with: Dr. Nancy Haegel, in my early days, helped me with most of my laboratory work. Dr. Joseph Kahn taught me much, and gave me advice in the laboratory. He also built the spectrometer used in this work. Dr. Robert McMurray, Jr. has been a constant advisor in almost every experimental and theoretical problem. I also thank Dr. David Nolte, who has helped me use the DLTS apparatus.

Our staff members; Paul Luke, Jeff Beeman, William Hansen, and Richard Davis, have helped in many aspects of this work. I thank Lynne Dory for her help in publishing papers, arrangements for trips and all the other things.

I am indebted to Dr. J. Farmer at Missouri Research Reactor Facility and Dr. T. Lim at Berkeley Research Reactor for neutron irradiation of germanium samples.

I appreciate the concern and support of my parents throughout the

course of my study. I am also grateful to Ministry of Education of Korea which has supported my four years of study in the United States.

Lastly but most heartfully, I cherish the time spent with my wife Wonhee during all these years. She has been the most helpful, and her support has been invaluable.

This work has been supported by NASA contract No. W-14,606 under Interagency Agreement with the Director's Office of Energy Research, Office of Health and Environmental Research, U.S. Department of Energy under Contract No. DE-AC03-76SF00098.

Table of Contents

page

Part I. Synthesis and Characterization of Neutron Transmutation Doped Germanium

1. Introduction 1

1.1 Theory of Shallow Impurity States 2

1.2 Neutron Transmutation Doping of Germanium 8

1.2.1 NTD Process in Germanium 10

1.2.2 Compensation Ratio of NTD Germanium 12

1.2.3 Radiation Defects in NTD Germanium 17

1.2.3.1 Radiation Defects in Semiconductors 19

1.2.3.2 Recovery of Radiation Defects 21

2. Experimental Techniques 23

2.1 Hall Effect Measurements 23

2.1.1 Hall Effect Measurements at 77 K 27

2.1.2 Variable Temperature Hall Effect Measurements 29

2.2 Infrared Absorption Spectroscopy 32

2.2.1 Photothermal Ionization Spectroscopy and Linear Absorption Spectroscopy 33

2.2.2 Fourier Transform Spectroscopy 36

2.2.3 Experimental Setup 44

2.3 Deep Level Transient Spectroscopy 52

2.3.1 Calculation of Trap Energy 54

2.3.2 Trap Capture Cross Section 55

2.3.3 Trap Concentration 56

3. Results and Discussion 58

3.1 Hall Effect Measurements: Free Carrier Concentration and Mobility 58

3.1.1 Determination of the Compensation Ratio of NTD Germanium 58

3.1.2 Free Carrier Concentration of NTD Germanium 62

3.1.3 Free Carrier Mobility of NTD Germanium 67

3.1.4 Freeze-Out Curves of NTD Germanium with Radiation Defects 68

3.2 Infrared Absorption Spectroscopy 70

3.2.1 Calibration of Absorption Peaks of Shallow Impurities in Germanium 70

3.2.2 Absorption Spectra of NTD Germanium 73

3.2.3 Absorption Spectra of Phosphorus-doped, NTD Germanium 81

3.3 Deep Level Transient Spectroscopy 85

3.3.1 Deep Level Defects in NTD Germanium (P-type) 86

3.3.2 N-type Germanium 90

3.4 Direct Observation of Neutron-Induced Defects in Germanium 95

4. Summary and Conclusions 98

Part II. Development of Far-Infrared Detectors using NTD Germanium

5. Introduction to Infrared Detectors 100

6. NTD Germanium Bolometers 101

6.1 Basic Operation Mechanism 103

6.2 Detector Fabrication 106

6.3 Resistivity Measurement 108

6.4 Discussion of Hopping Conduction 114

7. Far-Infrared Mixers 119

7.1 Basic Operation Mechanisms 121

7.1.1 Photoconductors 121

7.1.2 Mixers 125

7.2 Detector Fabrication 127

7.2.1 Single Crystal Growth 129

7.2.2 Neutron Transmutation Doping (Counter Doping) 133

7.2.3 Contact Preparation and Size of Detectors 134

7.3 Measurement of Detector Performance 136

3.3.1 Direct Photoconductivity Measurements 136

3.3.2 Heterodyne Measurements 144

7.4 Discussion of Results 147

8. Summary and Conclusions 155

References 158

Part I: Synthesis and Characterization of Neutron Transmutation Doped Germanium

1. Introduction

Neutron transmutation doping (NTD) has become a very important technique for achieving uniform doping of semiconductors. Especially in the development and production of high power, high voltage silicon devices, NTD has become the doping technique of choice [1]. NTD germanium also has found many uses such as in the study of hopping conduction [2], in the development of far-infrared detectors -- bolometers [3,4] and heterodyne mixers [5,6], and in the study of radiation defects in semiconductors [7].

The main advantages of the NTD technique are its extreme homogeneity and reproducibility. The process consists of thermal neutron irradiation and, upon capturing the neutrons, certain isotopes of a semiconductor decay into doping elements. Because of the uniform mixture of isotopes in the semiconductor and because of the small absorption of thermal neutrons in the incoming flux, the NTD process produces very uniform doping throughout the sample. The concentration of doping impurities is determined by the product of the thermal neutron capture cross section for the specific host isotope, the natural abundance of the dopant producing isotope, and the thermal neutron dose. Therefore, the doping concentration can be fully controlled by the total dose of thermal neutrons. The capture cross section for thermal neutrons in semiconductors is very small and the

thermal neutrons can penetrate many cm into the sample. Therefore, samples up to a few cm thick can easily be doped with this technique.

It is well known, however, that neutron irradiation in semiconductors also introduces radiation defects. The main cause for defect generation are the fast neutrons. Fast neutrons which do not contribute to the doping process unavoidably accompany the thermal neutron flux. They knock out host atoms producing defect clusters containing vacancies and interstitials. Numerous studies have dealt with the characterization of radiation defects in semiconductors but the radiation defects in NTD germanium were not studied in detail because of the complicated nature of fast neutron damage [8].

In this thesis work, an effort was made to understand the nature and the annealing of radiation defects in germanium produced by neutron irradiation using Hall effect measurements, infrared absorption spectroscopy, deep level transient spectroscopy, and transmission electron microscopy.

In part II, applications of NTD germanium in the fabrication of far-infrared detectors -- cryogenic bolometers and heterodyne mixers -- are illustrated and discussed.

1.1 Theory of Shallow Impurity States

Impurities in an otherwise perfect semiconductor can play an important role in the magnitude and the type of conductivity. The mastery of crystal growth and the introduction of known impurities in controlled amounts have proved to be the crucial factors in the

remarkable range of semiconductor devices invented in the past quarter of a century. Defects introduced either during crystal growth or by particle irradiation are another important factor in the electrical properties of semiconductors. Therefore, there have been many studies concentrating on revealing the nature of defects as well as to either introduce or remove them from a semiconductor.

We consider first the effect of impurities in elemental group IV semiconductor. Consider the group V impurity phosphorus in germanium. Four out of five valence electrons of phosphorus are used to form covalent bonds with its four nearest neighbors. The fifth electron, not incorporated in this bonding, is donated to the conduction band and the phosphorus is called "donor". However, at sufficiently low temperature the electron remains bound to the P^+ ion by the Coulomb attraction. The potential energy of the donor electron must take into account the adjustment of the charge density of the host in the field of the positively charged donor. The evaluation of this potential is a many-body problem. However, for distances r large compared to the lattice spacing a, this adjustment can be viewed as a polarization of the host described by its static dielectric constant ε. In this limit the potential is:

$$U(r) = -\frac{e^2}{\varepsilon r} \tag{1.1}$$

where e is the electron charge. In a crystal the electrons behave under an external field as particles with an effective mass m^*

satisfying the force equation:

$$F = m^* a = \hbar^2 \left(\frac{d^2E}{dk^2}\right)^{-1} \tag{1.2}$$

The effective mass m^* is different from the free electron mass m, being of the order of 0.1 m. Under these assumptions, the donor electron will have hydrogen-like bound states given by:

$$E_n = \frac{m^* e^4}{2\hbar^2 \varepsilon^2 n^2} \tag{1.3}$$

and a ground state Bohr radius:

$$a^* = \frac{\hbar^2 \varepsilon}{m^* e^2} \tag{1.4}$$

For example, in germanium, $m^* = 0.12$ m and $\varepsilon = 15.8$ yielding an binding energy E ~ 10 meV and the corresponding Bohr radius of ~ 80 Å for the ground state.

In an analogous fashion one can develop a model for substitutional group III impurities in germanium which bind the hole created in the valence band resulting from the formation of the covalent bond with its nearest neighbors. These impurities which have accepted an electron from the valence to complete the bonding scheme with its four nearest neighbors are called "acceptors".

This simple "hydrogenic" model based on the effective mass theory

(EMT) which was introduced by Kittel and Mitchel [9] and by Luttinger and Kohn [10] needs to be modified in two respects to explain the actual situation in semiconductors: i) the ground state binding energies of different group III (or V) impurities in germanium and silicon are different and ii) the effective mass m^* for many semiconductors is a tensor rather than a scalar, reflecting the nature of the valence (or conduction) band. EMT predicts the ionization energies of the shallow impurities quite well and works as a rough estimate for the properties of shallow impurities in semiconductors.

The binding energies of the excited states of shallow impurities in semiconductors calculated by effective mass theory are shown in Fig. 1.1 (group III acceptors in germanium [11,12]) and Fig. 1.2 (group V donors in germanium [13]) along with experimentally measured values [14]. Because the wavefunctions of p-like excited states have a node at $r = 0$, the binding energies of the p-like excited states do not depend upon the chemical species of the impurities in a semiconductor. The s-like ground state on the other hand has the largest probability density at the center of the nucleus ($r = 0$) and the binding energy of the ground state shows the dependence on the chemical species of the dopant impurities. The shift in the 1s ground state energy reflects the incomplete screening of the ionic charge by the core states in the vicinity of the impurity site. As r becomes smaller, the dielectric screening becomes less effective and as r becomes comparable to the size of the charged ion, the potential becomes $U(r) = - e^2/r$. This causes the binding energy of the electron to be somewhat higher than estimated by the effective mass

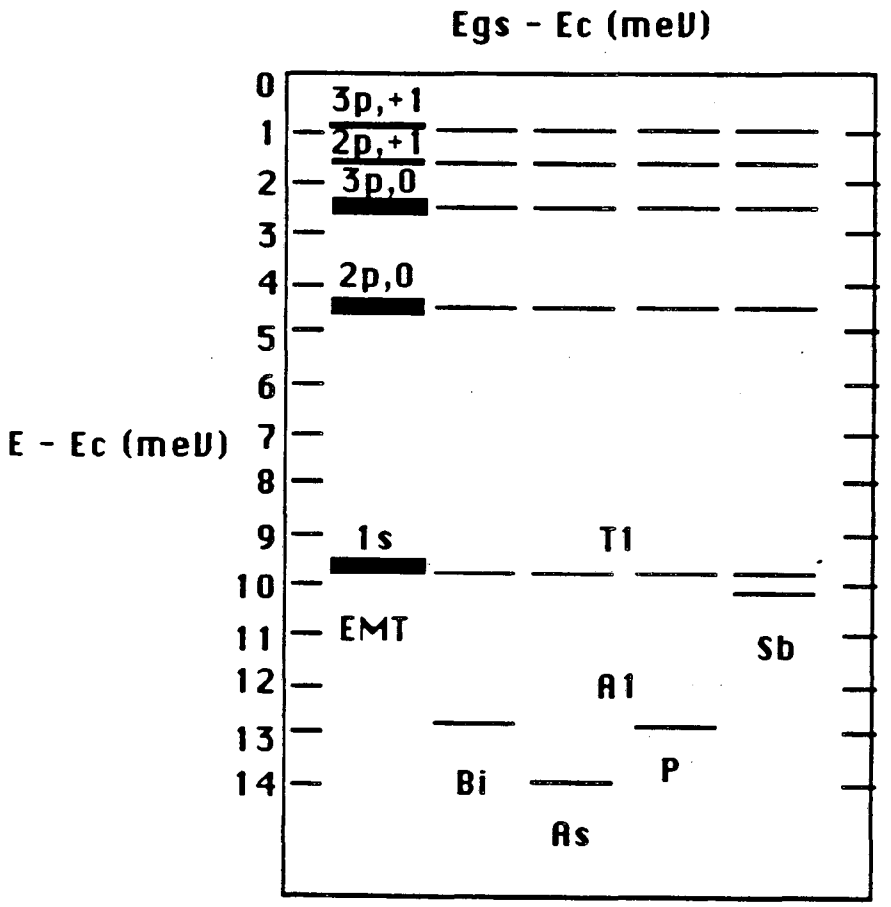

XBL 885-1657

Fig. 1.1 Energy diagram of bound excited states of group III impurities in germanium.

theory. And there is a general increase of the binding energy as the ionic radius of the impurity increases.

The ground state of a group V donor in germanium is more

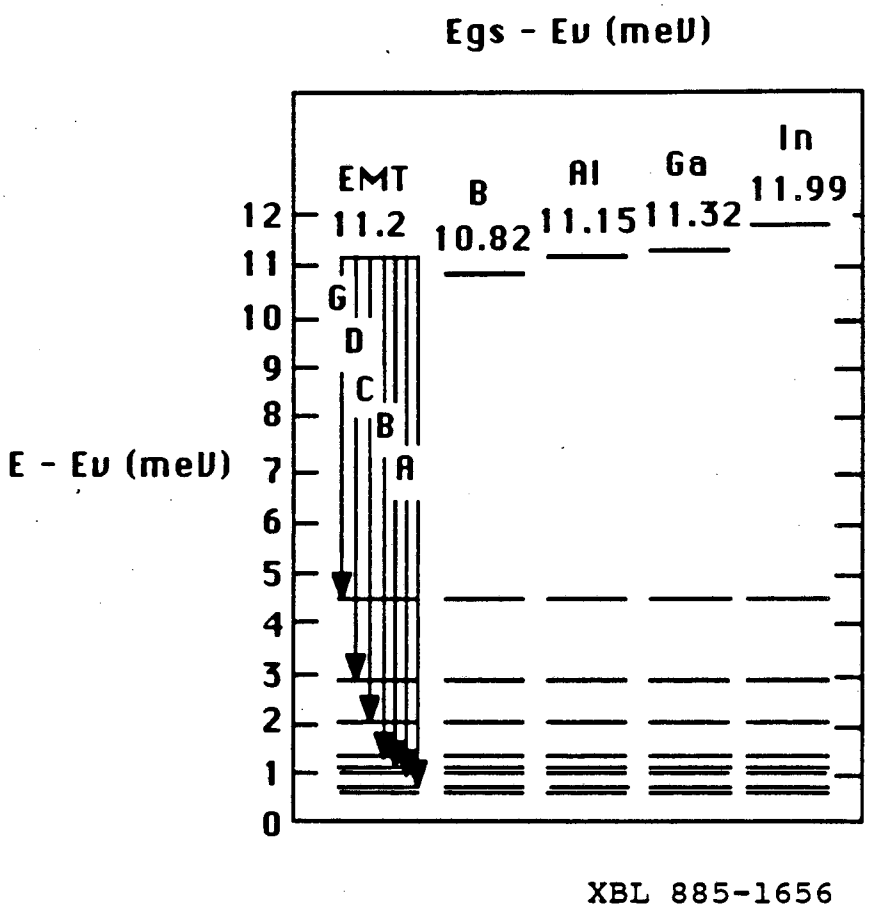

Fig. 1.2 Energy diagram of bound excited states of group V impurities in germanium.

complicated than is predicted by the effective mass theory [15]. Because of valley-orbit coupling it splits into a singlet and a triplet. The degree to which the actual ground-state levels differ

from the value given by the effective mass theory depends largely on the species of the group V impurity. The correction to the effective mass potential is usually considered as a perturbation whose effect is confined to the immediate vicinity of the donor impurities and hence only affects the s-like energy states.
The intensities of the absorption lines due to the transitions from the higher, triplet ground state decrease drastically as the sample temperature is lowered. At 4.2 K where the measurements of our study were performed, we can neglect the contributions from the triplet ground state because it is insignificantly thermally populated.

The shift in the binding energy of ground state of group III acceptors is proportional to the ionic radius of the impurity. This simple trend is not found for group V donors in both silicon and germanium.

Detailed discussions on shallow impurity levels in semiconductors have been reported in many articles [16 - 19]

1.2 Neutron Transmutation Doping of Germanium

In 1950, Cleland, Lark-Horovitz, and Pigg [20] investigated the effects of neutron irradiation on germanium. It was already known that neutron irradiation of germanium introduces acceptor levels. The reasons for the introduction of these acceptors were shown to be i) lattice displacements produced by fast neutrons and ii) impurity centers produced by the transmutations due to slow (thermal) neutrons. The proof of the second process was that prolonged

annealing of the irradiated sample failed to fully restore the original conductivity. (This argument, however, is not a perfect proof because fast diffusing acceptor impurities could enter the crystal during annealing.) This neutron irradiation technique has in the mean time become a well established method for doping bulk semiconductors.

Compared to the conventional doping techniques, NTD creates very uniform and reproducible doping of the sample. This uniformity and reproducibility was used in the study of impurity hopping conduction by Fritzsche [2]. In the development of cryogenic bolometers whose operation depends on the hopping conduction, NTD germanium is the prime candidate. Also in the special case of counter doping, the NTD technique can safely be used in combination with chemical impurity doping. We used this method in the fabrication of far-infrared heterodyne mixers as discussed in part II.

It is well known, however, that neutron irradiation on semiconductors produces radiation defects in addition to the dopant impurities. Due to the very complicated nature of the neutron irradiation damage, the radiation defects due to the neutron have not been studied in detail. Although it has been reported that annealing at about 400°C for several hr removes most of the radiation defects [21,22], the detailed nature of the defects and the annealing process are still in doubt.

1.2.1 NTD Process in Germanium

The NTD process in germanium is summarized in Table 1.2 with the isotopic fractions of all stable germanium isotopes, the neutron capture cross sections, and half-life of the decay reactions. There are five stable isotopes in germanium. Of those five isotopes, ^{72}Ge and ^{73}Ge just redistribute the isotopes of germanium and do not take part in the doping processes. However, ^{70}Ge becomes ^{71}Ge after capturing a thermal neutron which is unstable and decays into ^{71}Ga which is an acceptor. ^{74}Ge and ^{76}Ge become ^{75}Ge and ^{77}Ge, respectively, which are unstable, and decay into ^{75}As and ^{77}Se, both of which are donors. As is shown, the capture cross sections of the reactions are very small (1 barn = 10^{-24} cm^2). This makes the penetration of thermal neutrons into semiconductors easy and the absorption length can be as large as a few cm. Up to a few cm thick specimens can be doped with this technique.

The NTD process produces very uniform and reproducible doping. Since the isotopes of semiconductors are distributed randomly throughout the crystal, the transmutation created impurities are also uniformly distributed. And since the concentration of transmutation created impurities depends only upon the isotopic concentration, neutron capture cross section, and neutron fluence, the doping concentration can be controlled by just choosing the appropriate total neutron fluence.

The NTD processes for silicon and gallium arsenide are shown in

Table 1.1 NTD Process in Germanium

Isotopic Fraction	Reaction	σ_c(b)	$t_{1/2}$	Type
(20.5%)	${}^{70}_{32}Ge(n,\gamma)\ {}^{71}_{32}Ge \rightarrow {}^{71}_{31}Ga + EC$	3.25	11.2d	p
(36.5%)	${}^{74}_{32}Ge(n,\gamma)\ {}^{75}_{32}Ge \rightarrow {}^{75}_{33}As + \beta^-$	.52	82.2m	n
(7.8%)	${}^{76}_{32}Ge(n,\gamma)\ {}^{77}_{32}Ge \rightarrow {}^{77}_{33}As + \beta^-$	.16	11.3h	
	$\rightarrow {}^{77}_{34}Se + \beta^-$		38.8h	n

Table 1.2 NTD Process in Silicon and Gallium Arsenide

NTD Process in Silicon

Isotopic Fraction	Reaction	σ_c(b)	$t_{1/2}$	Type
(92.3%)	${}^{28}_{14}Si(n,\gamma)\ {}^{29}_{14}Si$			
(4.7%)	${}^{29}_{14}Si(n,\gamma)\ {}^{30}_{14}Si$			
(3.1%)	${}^{30}_{14}Si(n,\gamma)\ {}^{31}_{14}Si \rightarrow {}^{31}_{15}P + \beta^-$	0.108	2.62h	n

NTD Process in Gallium Arsenide

Isotopic Fraction	Reaction	σ_c(b)	$t_{1/2}$	Type
(60.1%)	${}^{69}_{31}Ga(n,\gamma)\ {}^{70}_{31}Ga \rightarrow {}^{70}_{32}Ge + \beta^-$	1.7	21.1m	n
(39.9%)	${}^{71}_{31}Ga(n,\gamma)\ {}^{72}_{32}Ga \rightarrow {}^{72}_{32}Ge + \beta^-$	4.6	14.1h	n
(100.0%)	${}^{75}_{33}As(n,\gamma)\ {}^{76}_{33}As \rightarrow {}^{76}_{34}Se + \beta^-$	4.4	26.3h	n

Table 1.2. One interesting fact here is that NTD germanium contains both acceptors and donors while NTD silicon and NTD gallium arsenide have n-type dopants only. NTD germanium is, therefore, compensated and the compensation ratio is fixed by the product of isotopic concentration and neutron capture cross section of dopant producing isotopes.

In the neutron irradiated semiconductors there are several causes for the formation of radiation damage. Of those, knock-on displacements of germanium atoms by fast neutrons are the primary cause. The fast neutrons do not participate in the doping process but always accompany the thermal neutron and produce radiation damage. This radiation damage is usually removed by thermal annealing. In germanium annealing up to about 400°C is necessary to remove most of the radiation damage. It is also commonly believed that the transmutation created impurities tend not to reside in the substitutional position where they are electrically active. Thermal annealing again helps to move these impurities into substitutional sites.

1.2.2 Compensation Ratio of NTD Germanium

As mentioned above, NTD germanium has both types of dopants and is self compensated. The concentration of each impurity produced by neutron irradiation is:

$$N_x = \rho_{Ge} X_x \sigma_x n \tag{1.5}$$

where ρ_{Ge} is the number density of germanium atoms (cm^{-3}), X_x the natural abundance of isotope x, σ_x the thermal neutron capture cross section (cm^2), and n the thermal neutron fluence (cm^{-2}). The compensation ratio is fixed by the product of isotopic fraction and neutron capture cross section of the dopant producing isotope. The compensation ratio, K, in NTD germanium is calculated as:

$$K = \frac{N_{As} + 2N_{Se}}{N_{Ga}} \tag{1.6}$$

here selenium is counted twice because it is a double donor compensating two holes. The values of the isotopic fractions of the stable germanium isotopes are well known and the deviations between reported values are small. The capture cross section for thermal neutrons, σ_c, is related to the energy of the incident neutron by:

$$\sigma_c \sim E^{-\frac{1}{2}} \sim \frac{1}{v} \tag{1.7}$$

for neutron energies up to ~ 10^4 eV [23]. Therefore, depending on the neutron energy spectrum of a particular reactor, the neutron capture cross section values change and compensation ratio values have been reported varying from 0.23 to 0.41 depending on the set of neutron capture cross section values which are used [24 - 32].

To find out the real compensation ratio of NTD germanium in our case, we conducted an experiment. As the half lifes for decay reactions are not the same, time dependence of net-carrier

concentration reveals important information. First of all, the half life of the gallium-producing reaction is 11.2 days, while those of arsenic and selenium producing reactions are 82.2 min and 38.8 hr (dominating process), respectively. Therefore, NTD germanium becomes n-type right after neutron irradiation because of very short half life of the arsenic producing reaction and then slowly changes towards p-type because the ultimate concentration of gallium after all the reaction have taken place is larger than the sum of the arsenic and twice the selenium concentrations. The time for the n- to p-type conversion is around 6 days after neutron irradiation, depending on the neutron capture cross section. The shortest time expected for type conversion is about 4 days and the longest time is approximately 8 days.

Figure 1.3 shows the expected evolution of each dopant impurity in NTD germanium using the neutron capture cross section values from reference [26]. As expected, the reaction for arsenic impurity formation is the fastest and is completed within a day after neutron irradiation. The selenium formation reaction is finished about 5 days after neutron irradiation and it takes a few weeks for gallium formation to be completed. The dotted curve is the change in the net dopant concentration. The curve crosses the $|N_A - N_D| = 0$ line at about 6 days in this case. Figure 1.4 shows the shift of the time for type conversion for different sets of neutron capture cross section values. In applying this method to find out the compensation values, one must be very careful about possible contamination of the sample by any electrically active impurities. Such a contamination may occur

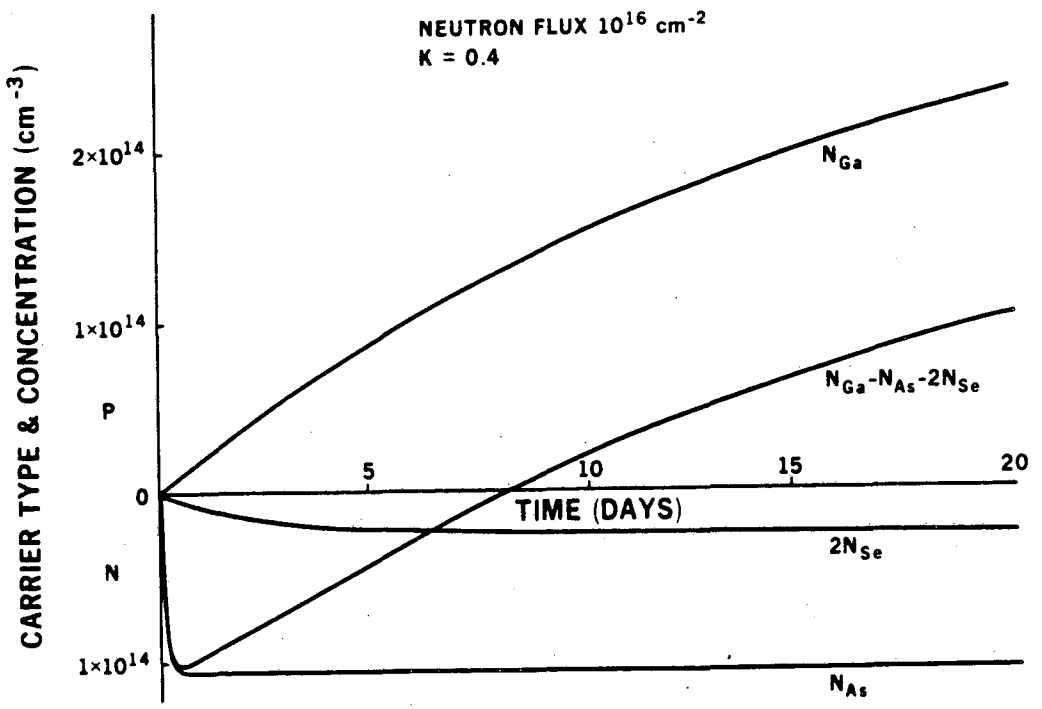

XBL 858 3768

Fig. 1.3 Time dependent evolution of each transmutation produced impurity in NTD germanium.

because the samples must be annealed after the neutron irradiation to remove the radiation damage and to activate the transmutation produced impurities. In this annealing process, fast diffusing elements such as copper may diffuse into the sample and contribute to the net-carrier concentration. Fig. 1.5 shows the effect of the contamination by the p-type impurity copper. The net doping concentration curve is now shifted towards the p-type side and one obtains the time to p-type conversion which is shorter than in the absence of copper acceptors. Contamination by a n-type impurity would have the opposite effect and

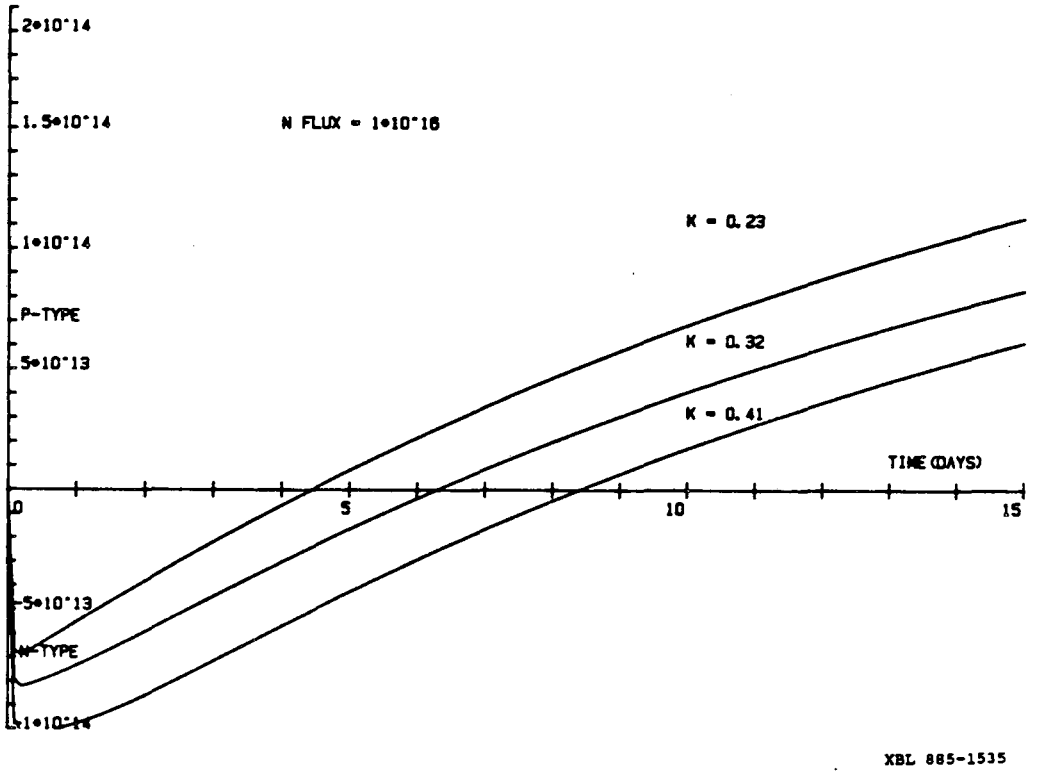

Fig. 1.4 Effect of neutron capture cross section of isotopes on the time for n- to p-type conversion in NTD germanium.

the time of conversion would be shifted towards longer times. To avoid this problem, one can do the same measurement on several samples irradiated with different amount of neutrons in the same location of a particular reactor. The expected results of such an experiment are shown in Fig. 1.6. The samples irradiated with different fluences of neutrons have different concentrations of net-carriers but the time or the NTD-related type conversion must be exactly the same. The curves cross at a time at which the NTD-related type conversion occurs. This time does not change even if the sample is contaminated by an impurity as long as the extent of contamination is the same in each sample,

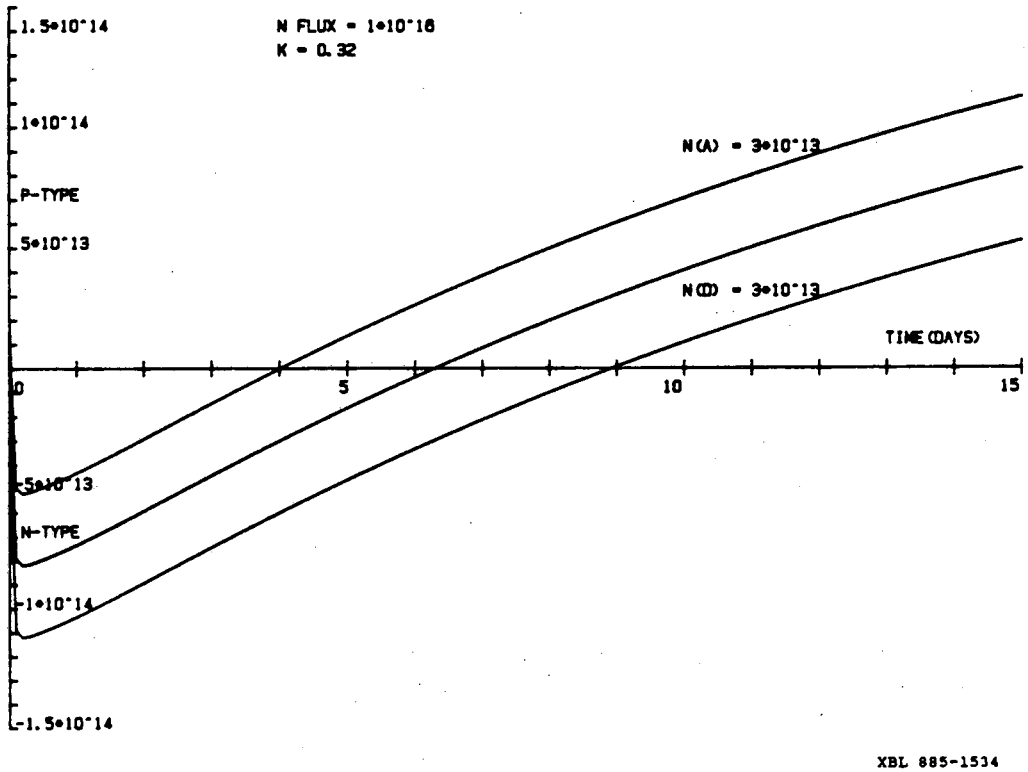

Fig. 1.5 Effect of contamination of electrically active impurities on the time for n- to p-type conversion in NTD germanium.

i.e., the samples must be processed in precisely the same way. The contamination shifts this crossing point to above or below the time axis ($N_A - N_D = 0$) as shown in Fig. 1.6.

1.2.3 Radiation Defects in NTD Germanium

Neutron irradiation of a semiconductor induces radiation defects as well as dopant impurities. The primary cause of radiation defects in NTD semiconductors is the presence of fast neutrons in the thermal

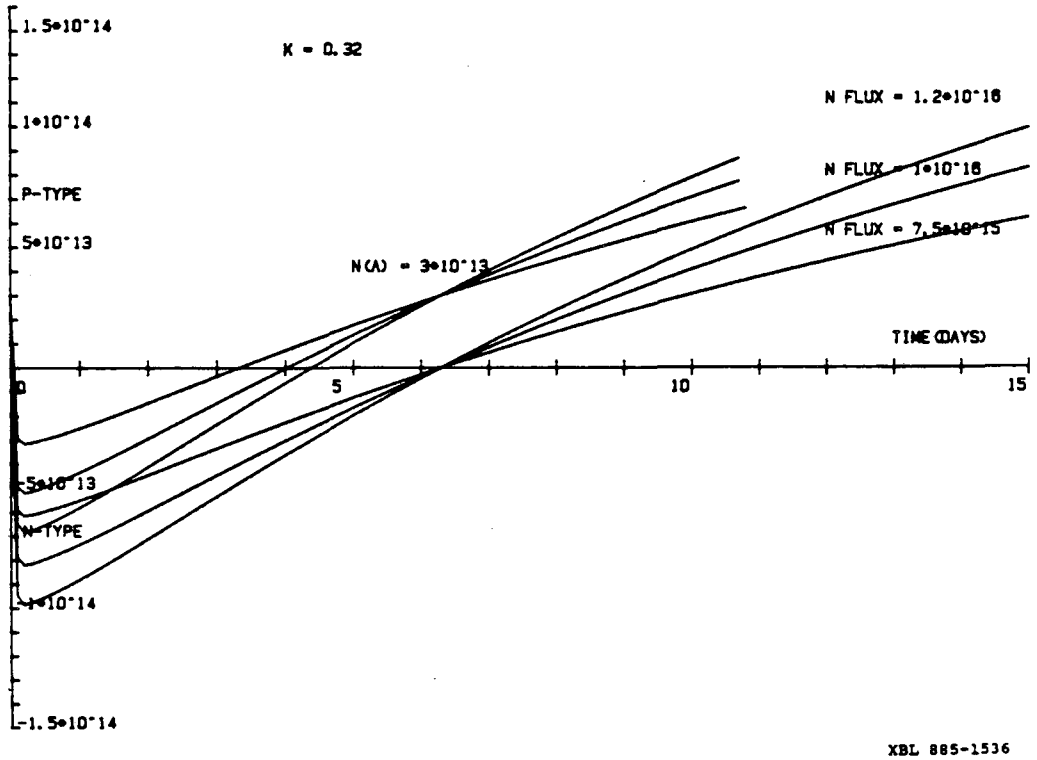

Fig. 1.6 Theoretical curves of evolution of transmutation produced impurities for different neutron fluence in NTD germanium.

neutron flux. These fast neutrons, which inevitably accompanies thermal neutrons, do not take part in the transmutation processes but produce damage by knocking out host atoms. Because of the high mass of neutrons, the radiation damage in neutron irradiated semiconductor is much more extended and complicated than in either electron or γ irradiated semiconductors. Characterization of radiation damage in NTD semiconductors by electrical method is usually very difficult because thermal neutron irradiation introduces electrically active dopant impurities in addition to radiation damages.

It is worth while to review some of the previous results on the study of irradiated semiconductors to improve the understanding of our results.

1.2.3.1 Radiation Defects in Semiconductors

The family of radiation defects in semiconductors is very large and includes everything from simple isolated Frenkel pairs, produced by energetic γ rays and electron irradiation, to very complex defect clusters produced by fast neutrons and other massive particles. The presence of these defects in irradiated semiconductors is most easily recognized by a change in electrical properties after irradiation. But more rigorous and detailed studies are needed to find out the precise nature of these radiation defects in semiconductors. The field of radiation defects in semiconductors has a very long history and we can only focus on a few topics specific to NTD.

Gossick [33] and Gossick and Crawford [34] proposed a model for the neutron-induced damage in n-type germanium. They described the damage as a p-type disordered region, encompassed by an insulating positive space charge region embedded in the n-type matrix. The presence of disordered regions with radii of ~ 100 Å was indicated by the results of Crawford and Cleland [35] who used this model to interprete their measurements of Hall mobility and conductivity in n-type germanium irradiated at room temperature with fast neutrons. Parsons et al [36] reported the direct observation of clusters in thin germanium films irradiated with neutrons using transmission electron

microscopy. These disordered regions were present at room temperature. The irradiation of 2 ~ 3 MeV electrons did not produce such damage.

Impurities present in a semiconductor before irradiation play an important role in the formation of radiation defect centers. One of the most extensively studied impurities in this respect is oxygen. Bond centered oxygen which is electrically inactive in silicon and germanium readily forms a complex with a vacancy which is called "A center" in silicon [37]. This A center is optically active and local vibrational modes are observed by IR absorption spectroscopy. Evidence for the presence of this complex in germanium have been found by IR absorption [37] and EPR [38] studies. Group V impurities also form complexes with vacancies in germanium and silicon. In silicon, such complexes are known as "E centers" [39]. The same complex has been identified in irradiated arsenic-doped [40,41] and antimony-doped [42] germanium. Such donor-vacancy complexes in irradiated germanium has been studied in detail by other workers [43,44].

The energy levels which are introduced by radiation defects or complexes in irradiated semiconductors affect the electrical properties. Blount [45] has proposed four energy levels due to isolated vacancies and interstitials in irradiated germanium. These levels are: $E_c - 0.2$ eV and $E_v + 0.07$ eV for interstitials and $E_v + 0.18$ eV and $E_v + \sim 0.01$ eV for vacancies. Recently, Nagesh and Farmer [46] reported results of a DLTS study of γ and neutron irradiated germanium. By comparing the defect levels in differently irradiated germanium samples, they temporarily assigned four deep

levels: the planar four-vacancy complex with an energy level at E_c - 0.09 eV, the divacancy level at E_c - 0.17 eV, the vacancy-oxygen complex level at E_c - 0.27 eV, and the donor-vacancy complex level at E_c - 0.35 eV. Radiation-induced energy levels in silicon have been reported by many works [35,47].

1.2.3.2 Recovery of Radiation Defects

In both germanium and silicon, it was found that the isolated vacancies (produced by particle irradiation) are mobile at very low temperatures. Based on infrared spectroscopy results [37], the free vacancies in n-type germanium were found to migrate at temperatures as low as 65 K. Vacancies in p-type germanium were found to be less mobile than those in n-type germanium. There is evidence of vacancy migration in p-type germanium near 200 K [18,48]. Vacancies in silicon were found to be mobile at 65 K in n-type and at 160 ~ 180 K in p-type material [39]. The divacancy in silicon is believed to diffuse at around 125 ~ 150°C [49]. Interstitials in germanium are mobile at 77 K or probably at lower temperatures. Substitutional-impurity to interstitial-impurity conversion has been shown to take place upon interstitial-substitutional host atom place exchange. This kick-out mechanism is prevalent for certain impurities in silicon [50].

From these facts we conclude that most of the simple defects recover at room temperature. Extended defects due to fast neutrons, on the other hand, are not expected to anneal out at room temperature.

At higher temperatures, vacancies and interstitials are produced by the dissociation of large defect clusters. They in turn will form other small complexes. Such a process has clearly been shown by annealing studies of oxygen-defect complexes in neutron-irradiated germanium by Whan [37].

Annealing studies of donor-vacancy complexes in γ irradiated germanium have been reported [44,51]. The temperature for complete annealing depends on the specific group V impurity which forms a complex with a vacancy. Early studies showed a general shift of the annealing temperature of defect complexes to higher temperatures for the neutron irradiated samples than energetic γ ray or electron irradiated samples [52]. It is believed that the radiation defects produced by neutron irradiation consist of point defects and large defect clusters rather than mono- or divavancies.

It was reported that annealing at 400°C removes most of the radiation defects in NTD germanium [21,22]. The reports were based on the measurement of the change in electrical properties of irradiated germanium after annealing. Such experiments cannot provide any information on the microscopic nature of the various dopants and dopant-defect interactions. A major objective of this thesis work is to reveal the behavior of each transmutation produced dopant species and their interaction with radiation defects in NTD germanium.

2. Experimental Technique

2.1 Hall Effect Measurement

Carriers which have a velocity component perpendicular to the direction of a magnetic field will be deflected from the direction of motion by the Lorentz force. This deflection causes a Hall voltage to appear across the sample perpendicular to the current flow direction. This voltage is measured experimentally to calculate the free carrier concentration. With the experimental set up shown in Fig. 2.1 the Hall voltage V_y is given by:

$$V_y = R_H I_x B_z d^{-1} \tag{2.1}$$

where I_x is the current flowing through the sample, B_z is the magnetic field applied perpendicular to the sample, and d is the sample thickness in the direction of the magnetic field. R_H is called the Hall coefficient and is given by:

$$R_H = \frac{r_H}{ne} \tag{2.2}$$

where r_H is called the Hall factor given by:

$$r_H = \frac{\langle \tau_m^2 \rangle}{\langle \tau_m \rangle^2} \tag{2.3}$$

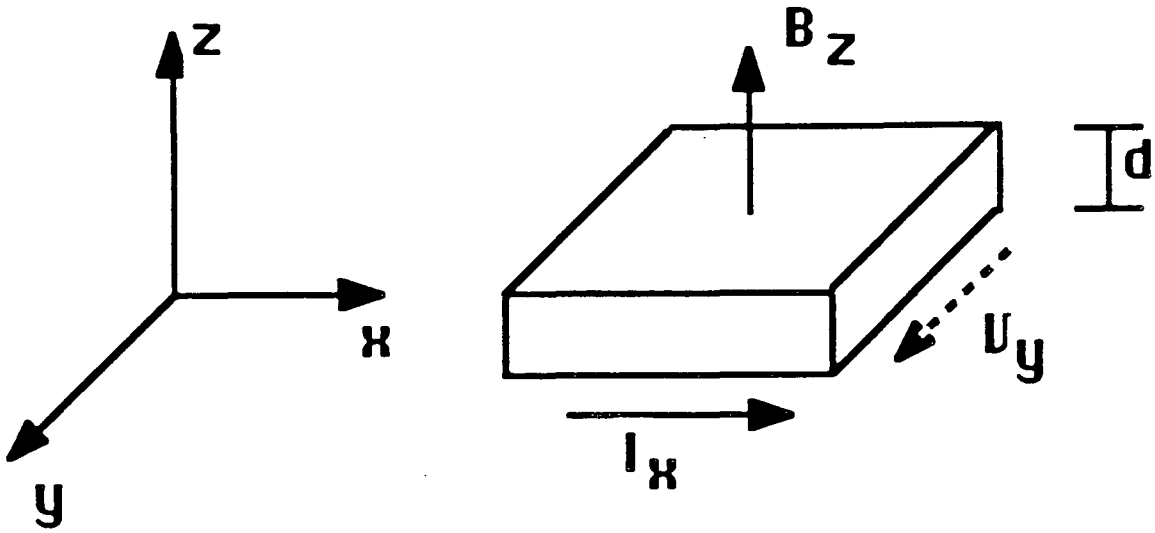

XBL 885-1654

Fig. 2.1 Schematic geometry for Hall effect measurement.

where τ_m is the momentum relaxation time. Assuming τ_m depends on the ratio of the carrier energy and the thermal energy of an atom, $\tau_m = \tau_0(E/kT)^r$. Here r is a constant having values between -1/2 and 3/2 depending on the scattering process [53]. The Hall factor r_H becomes:

$$r_H = \frac{3\pi(2r + \frac{3}{2})!}{4[(r + \frac{3}{2})!]^2} \tag{2.4}$$

For acoustic deformation potential scattering with r = -1/2, the Hall factor becomes 1.18 and for ionized impurity scattering where r = 3/2,

the Hall factor becomes 1.93. The order of magnitude of r_H is 1 and the exact value of this factor can be obtained from experiment for various conditions of measurement (type of conduction, sample temperature, magnitude of magnetic field used, crystal orientation, etc.) [54,55].

The Hall coefficient is negative for n-type conductivity and positive for p-type. Therefore, the Hall effect is an important method for the determination of the type of conductivity. From R_H the carrier concentration can be determined:

$$n \text{ or } p = \frac{r_H}{R_H e} \tag{2.5}$$

The Hall mobility is defined by the product of the conductivity σ and the Hall coefficient R_H:

$$\mu_H = R_H \sigma = \frac{r_H}{ne} ne\mu = r_H \mu \tag{2.6}$$

The Hall mobility is different from the drift mobility by the Hall factor. Usually it is the Hall mobility which is measured rather than the drift mobility.

In most practical situations, a Hall effect configuration suggested by L. J. van der Pauw is used [56]. Van der Pauw applied conformal transformation of an arbitrarily shaped lamellea of constant thickness δ onto a semi-infinite half plane to calculate the resistivity. The current flow pattern and equipotential lines are

easily calculated in the half plane. The resistivity ρ is:

$$\rho = \frac{\pi\delta}{\ln 2} \frac{(R_{12,34} + R_{23,41})}{2} \times f \tag{2.7}$$

where δ = thickness of the sample, $R_{12,34} = \Delta V_{34}/I_{12}$, $R_{23,41} = \Delta V_{41}/I_{23}$, and the factor f depends on the ratio of the resistances. The direction of the magnetic field B has to be perpendicular to the sample. The Hall coefficient R_H is:

$$R_H = \frac{\delta \Delta R_{24,13}}{B} \tag{2.8}$$

where $\Delta R_{24,13} = \Delta V_{13}/I_{24}$ and V_{13} corresponds to the usual Hall voltage. The free carrier concentration is found to be:

$$n \text{ or } p = \frac{B}{\delta \Delta R_{24,13} e} \tag{2.9}$$

By combining the equations for ρ and n (or p), one can determine the mobility:

$$\mu = \frac{1}{en\rho} = \frac{2\ln 2}{\pi B} \frac{\Delta R_{24,13}}{(R_{12,34} + R_{23,41})} \frac{1}{f} \tag{2.10}$$

Ohmic contacts for p-type samples were prepared either by implanting boron or by alloying a small amount of indium on four corners of the sample. For n-type samples, either a phosphorus-

implanted or lithium-diffused, indium-soldered contact was used as the ohmic contact.

2.1.1 Hall Effect Measurement at 77 K

When one wants to measure extrinsic carrier concentration in pure germanium, one cools the sample to 77 K (liquid nitrogen temperature). The intrinsic carrier concentration is suppressed and the extrinsic carrier concentration which is much larger than the intrinsic carrier concentration can be measured.

The measurement setup consists of a liquid nitrogen container with two coils wound in a Helmholtz configuration [57], a DC power supply for the magnetic field, a variable current supply for the sample (schematic shown in Fig. 2.2), and a voltmeter. With 4 A of current flowing, the two coils produce a magnetic field of 106 G which is perpendicular to the bottom of the container as well as to the sample. The measurement is performed for at least three different sample currents (The Hall voltage and the resistivity are proportional to the current over two orders of magnitude.) passing through the sample and the average value of three sets of data are used in the calculation of carrier concentration and carrier molibity. The Hall scattering factors r_H for n- and p-type germanium have been taken from the published literature [54,55]. The crystal orientation dependence can be typically neglected because it leads to a very small error.

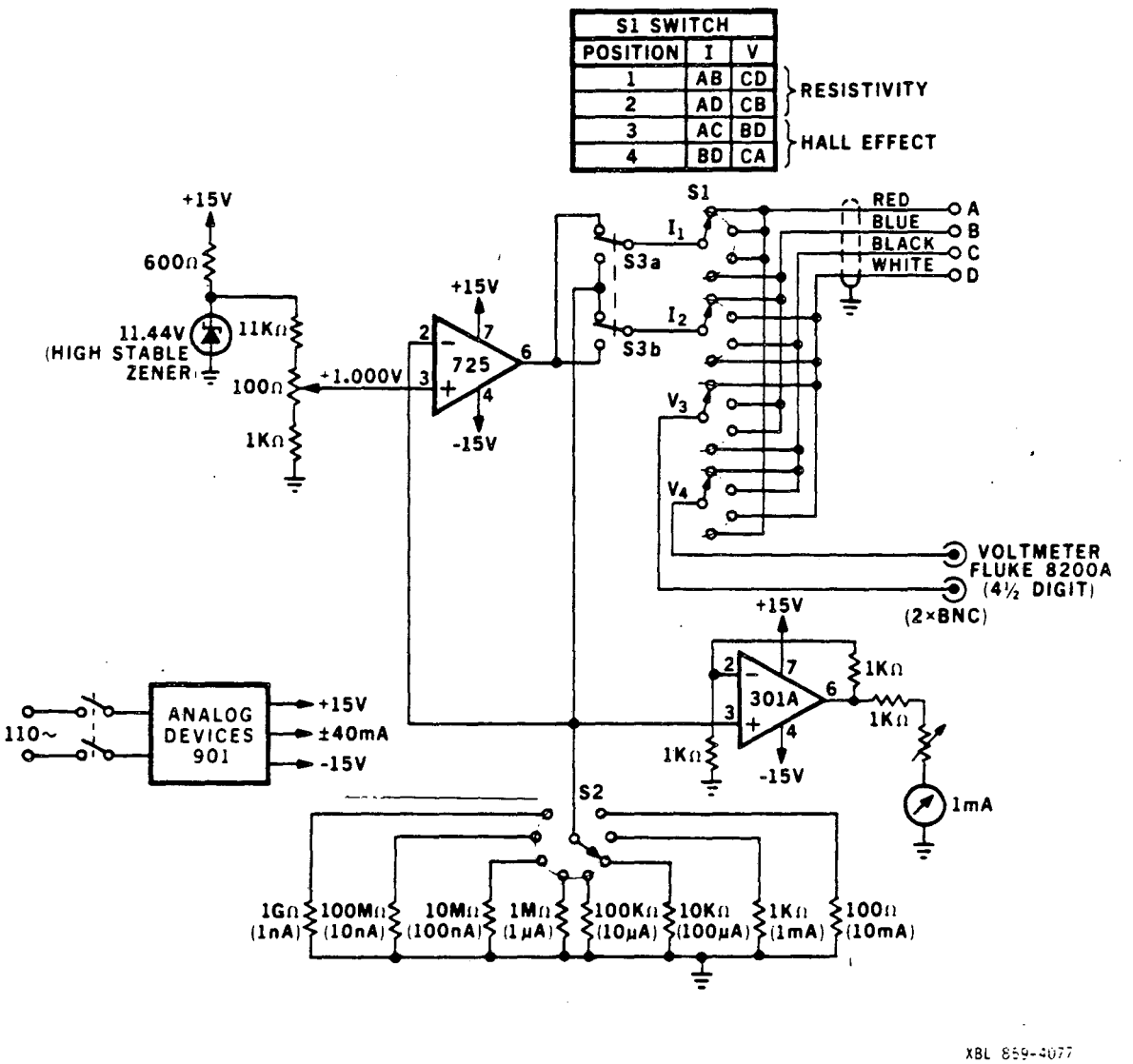

Fig. 2.2 Schematic of variable current supply used in Hall effect measurement.

2.1.2 Variable Temperature Hall Effect Measurement

By measuring the Hall coefficient over a broad range of temperatures, one obtains more information than just the net-carrier concentration, resistivity and carrier mobility of the semiconductors at one temperature. One can obtain information about the energy gap, the concentration of majority impurities, the ionization energy of the majority impurities, and the concentration of minority (compensating) impurities.

In the intrinsic range where $n_i = p_i$, the intrinsic carrier concentration is given by:

$$n_i^2 = N_c N_v \exp(-\frac{E_g}{kT}) \qquad (2.11)$$

N_c is the effective density of states in the conduction band, N_v is the effective density of states in the valence band, E_g is the minimum in energy gap, k is the Boltzmann constant (= 8.62×10^{-5} eV K^{-1}), and T is the absolute temperature. By plotting ln (n_i) vs. 1/T, one obtains a straight line with slope $- E_g/k$ in the intrinsic range. From this slope, the energy gap is obtained. In our case where the semiconductor is known, one can use the intrinsic range for an accuracy and equipment test.

In the extrinsic or saturation range, the calculation becomes more complicated. First we consider a semiconductor with N_D donors with no acceptors. The ionization energy of the donor, E_D, is assumed to be much smaller than the energy gap of the semiconductor. In order to

determine the carrier concentration a relation between the position of the Fermi level and that of the impurity center must be discussed. The probability that an energy level E_D is occupied is:

$$f(E_D) = \frac{1}{1 + \frac{1}{2} \exp \frac{E_D - E_F}{kT}} \tag{2.12}$$

where E_F is the Fermi energy and g is the donor level degeneracy and is assumed to be 2. Considering the total number of electrons available, we find:

$$N = \frac{N_D}{1 + \frac{1}{2} \exp \frac{E_D - E_F}{kT}} + n \tag{2.13}$$

N is the total number of electrons available, N_D is the concentration of donors, and n is the concentration of electrons in the conduction band. From the above two equations we obtain an expression for n:

$$n = \frac{1}{2}(\phi + N_D - N)([1 + \frac{4N\phi}{(\phi + N_D - N)^2}]^{\frac{1}{2}} - 1) \tag{2.14}$$

where ϕ is given by:

$$\phi = \frac{n(N_D - N + n)}{N - n} = \frac{1}{2} N_C \exp \frac{E_D}{kT} \tag{2.15}$$

When the semiconductor contains only donor impurities, N equals N_D. But in all "real" cases there are some residual acceptors, and in the above equations, N must be replaced by $N_D - N_A$. The material with both types of impurities is called "compensated" and is the common case for semiconductors.

At temperatures where $n_i > N_D$ equation 2.11 is satisfied. At temperatures, such that $kT >> E_D$ but which are still sufficiently low for $kT << E_g$, the equation becomes:

$$n = N_D - N_A \tag{2.16}$$

which is called "saturation range" (or "extrinsic range") in the Arrhenius plot.

At very low temperatures, where $n << N_A$ (which automatically fulfills $n << N_D$)), the expression for n becomes:

$$n = \frac{N_D - N_A}{N_A} \frac{N_C}{2} \exp \frac{E_D}{kT} \tag{2.17}$$

For the special case $n > N_A$ but $n < N_D$, the corresponding equation is:

$$n = \left(\frac{N_D N_C}{2}\right)^{\frac{1}{2}} \exp \frac{E_D}{2kT} \tag{2.18}$$

From the above discussion, it is clear that:

i) at sufficiently high temperatures, n will tend to be a constant value since all the available electrons ($N_D - N_A$) will be excited into the conduction band;

ii) at an intermediate temperature range, the Arrhenius plot [ln (n or p) vs. 1/T] will yield a straight line with slope $- E_D/2k$; and

iii) at very low temperatures, the same plot will yield a straight line with slope $- E_D/k$, and the concentration value where the slope of the plot changes corresponds to the concentration of the compensating impurities, N_A.

The experimental apparatus for variable temperature Hall effect used in this study consists of a cryogenic system (Lakeshore CT-310*) that holds two samples between the poles of a magnet and automated electronics controlled by an HP-85* computer for data collection. A magnetic field of 3 kG and a variable sample current between 10^{-9} and 10^{-2} A was used in the Hall voltage measurement. Details of the Hall effect system used are explained elsewhere [58].

2.2 Infrared Absorption Spectroscopy

Electronic transitions of a bound electron or hole from a 1s ground state to one of the p-like excited states of a donor or acceptor impurity in semiconductors can be used to identify the impurity species and to calculate the concentration of the impurity. As explained in Chapter 1, the excited states of impurities in a semiconductor are not affected by the impurity core and depend only on the conduction and valence bands of the host. The ground state,

however, has an s-like wavefunction which greatly depends on the particular impurity core and differs from one impurity to another. Therefore, the series of electronic dipole transitions from the ground to one of the bound excited states of an impurity in a semiconductor is particular to that impurity and can be used to identify the impurity species. The absorption peak intensity in the spectrum depends on the concentration of the impurity and this can be used to determine the impurity concentration.

2.2.1 Photothermal Ionization Spectroscopy (PTIS) and Linear Absorption Spectroscopy

There are two ways of performing the infrared spectroscopy: photothermal ionization spectroscopy (PTIS) and linear absorption spectroscopy. These two techniques are compared schematically in Fig. 2.3. In PTIS, the change in the conductivity of the sample due to absorption of photons is recorded as a signal (the sample works as a photoconductor) while in linear absorption spectroscopy, the intensity of the beam transmitted through the sample is recorded by a separate detector.

In a PTIS measurement, the incident photons with energies corresponding to precisely the energy difference between the ground state and one of the bound excited states are absorbed by bound carriers. The electrons (or holes) which are excited to one of the higher lying bound states may be excited into the conduction (or valence) band via absorption of a phonon. This two step ionization

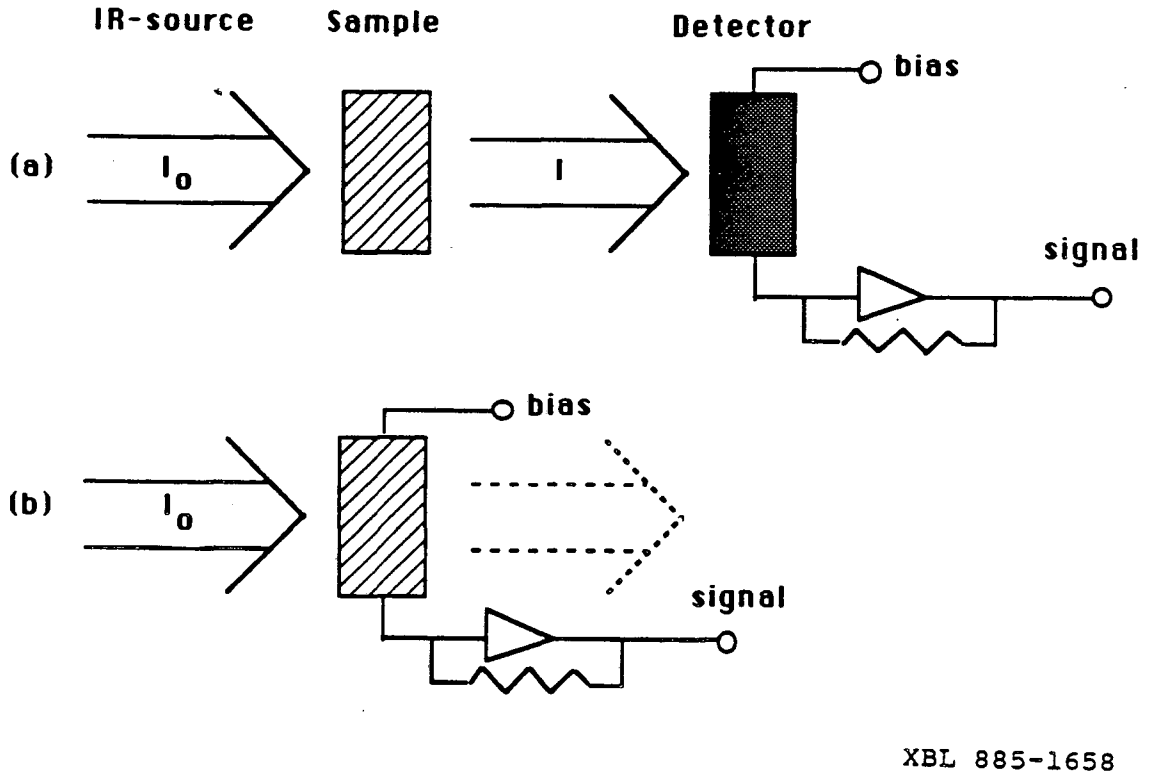

Fig. 2.3 Comparison of PTIS and absorption spectroscopy.

has a high probability because the second step is very small and the phonon population can be optimized for it to occur. Any extra free carriers in a band change the conductivity of the sample. This change in conductivity is essentially the signal. The best spectra are obtained in germanium at temperatures around ~ 6.5 K. In PTIS measurements, the absorption is detected as long as the carriers which are excited into the conduction band produce a measurable change in conductivity. The detection limit for shallow donors (acceptors) is very low and has been estimated to be 10^5 cm^{-3} [59].

In standard absorption spectroscopy, the incident photons with energies corresponding to one of the ground state to bound excited state energy differences are absorbed by the bound carriers reducing the intensity of the transmitted beam. This reduction corresponds to the signal. The measurement is performed at low temperatures where $N_A - N_D$ impurities are neutral (usually 4.2 K for germanium). For the absorption to be detected, an amount of photons should be removed from the incident flux which produces a signal in the detector which is larger than the detector noise. The detection limit of absorption spectroscopy for shallow impurities lies around 10^{12} cm^{-3}.

In PTIS or absorption spectroscopy, the impurity is identified by observing a series of absorption peaks at well defined energies. Exact values for electronic transitions for all known impurities have been reported [13,14,60,61]. A simple comparison of the position of the absorption peaks with published data reveals the identity of an impurity.

The absorption coefficient α is obtained from the relation between the intensity of incident beam and that of the beam transmitted through a sample:

$$\frac{I}{I_o} = \frac{(1 - R)^2 e^{-\alpha d}}{1 - R^2 e^{-2\alpha d}} \tag{2.19}$$

considering multiple internal reflections. Here I and I_o are the intensities of transmitted and incident beams, respectively, R is the

index of refraction (= 4 for germanium), and d is the sample thickness. The linear absorption coefficient α is linearly proportional to the concentration of the impurity that produces the absorption:

$$\alpha \sim \sigma N_I \tag{2.20}$$

σ is the absorption cross section and N_I is the impurity concentration. From this simple relation, the impurity concentration can be obtained by comparing the absorption coefficient of the absorption peaks with known values.

2.2.2 Fourier Transform Spectroscopy

The IR spectroscopy method used in this study was Fourier transform spectroscopy. This technique has many advantages over conventional spectroscopy. We first consider the basic aspects of Fourier transform spectroscopy.

Figure 2.4 shows the schematic of a Michelson interferometer. It consists of a light source, beam splitters, a fixed mirror and a movable mirror.

The changes in the beam intensity that occur as movable mirror M_1 is translated are measured with the mirror and detector arrangement shown in the figure. In the hypothetical case of a monochromatic light, the detector would record a intensity of illumination which varies sinusoidally. If the wavenumber is ν_1 and

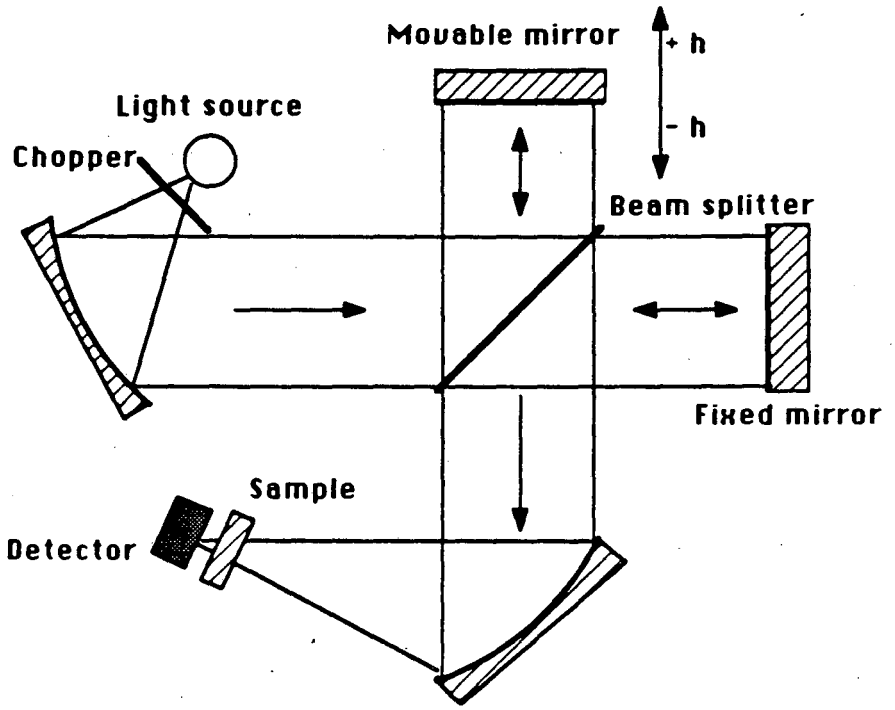

XBL 885-1663

Fig. 2.4 Schematic of an interforemeter.

the combining beams are of equal amplitude, A_1, then the intensity as a function of optical path difference l (= 2h, h is the distance M_1 travels) is given by:

$$I_{\nu l}(l) = 4A_1^2\cos^2(\pi\nu_1 l) \tag{2.21}$$

This can be written as:

$$I_{\nu l}(l) = 2A_1^2[1 + \cos(2\pi\nu_1 l)] \tag{2.22}$$

The intensity measured by the detector for light of spectral intensity distribution $B(\nu)$ is therefore given by:

$$I(l) = \int_{-\infty}^{\infty} B(\nu)[1 + \cos(2\pi\nu l)]d\nu \tag{2.23}$$

omitting numerical factors. The integral can be written as:

$$I(l) = \int_{-\infty}^{\infty} B(\nu)d\nu + \int_{-\infty}^{\infty} B(\nu)\cos(2\pi\nu l)d\nu \tag{2.24}$$

When the two mirrors are exactly equidistant optically from the beamsplitter, $l = 0$ and $I(l) = I(0) = 2\int_{-\infty}^{\infty} B(\nu)d\nu$. Therefore we have:

$$I(l) - \frac{1}{2}I(0) = \int_{-\infty}^{\infty} B(\nu)\cos(2\pi\nu l)d\nu \tag{2.25}$$

This is a cosine Fourier transform relationship and we can write:

$$B(\nu) = \int_{-\infty}^{\infty} [I(l) - \frac{1}{2}I(0)]\cos(2\pi\nu l)dl \tag{2.26}$$

This equation is often described as the basic equation of Fourier transform spectroscopy. It enables the intensity spectrum, $B(\nu)$, to be calculated for each chosen value of ν by performing the integration on the right.

The measured change in the intensity of light, $I(l) - (1/2)I(0)$, is called the "interferogram". Figure 2.5 shows an example of an interferogram and the spectrum obtained by integration of that

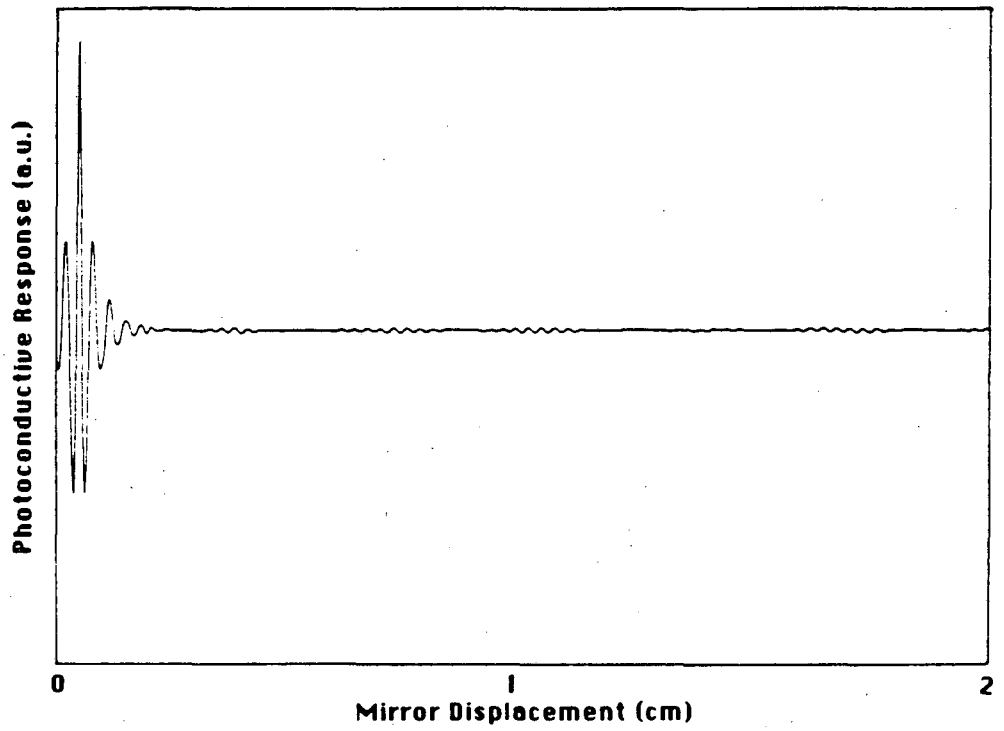

XBL 885-1664

Fig. 2.5(a) An example of a measured interfeorgram of arsenic doped germanium.

interferogram.

The advantages of Fourier transform spectrometers arise from two major concepts known as the Fellgett and Jacquinot advantages [62]. An interferometer receives information from the entire range of a given spectrum during each time element of a scan, whereas a conventional grating spectrometer receives information from only the very narrow region which lies within the exit slit of the instrument. Thus, the interferometer receives information about the entire spectral range during an entire scan, while the grating instrument

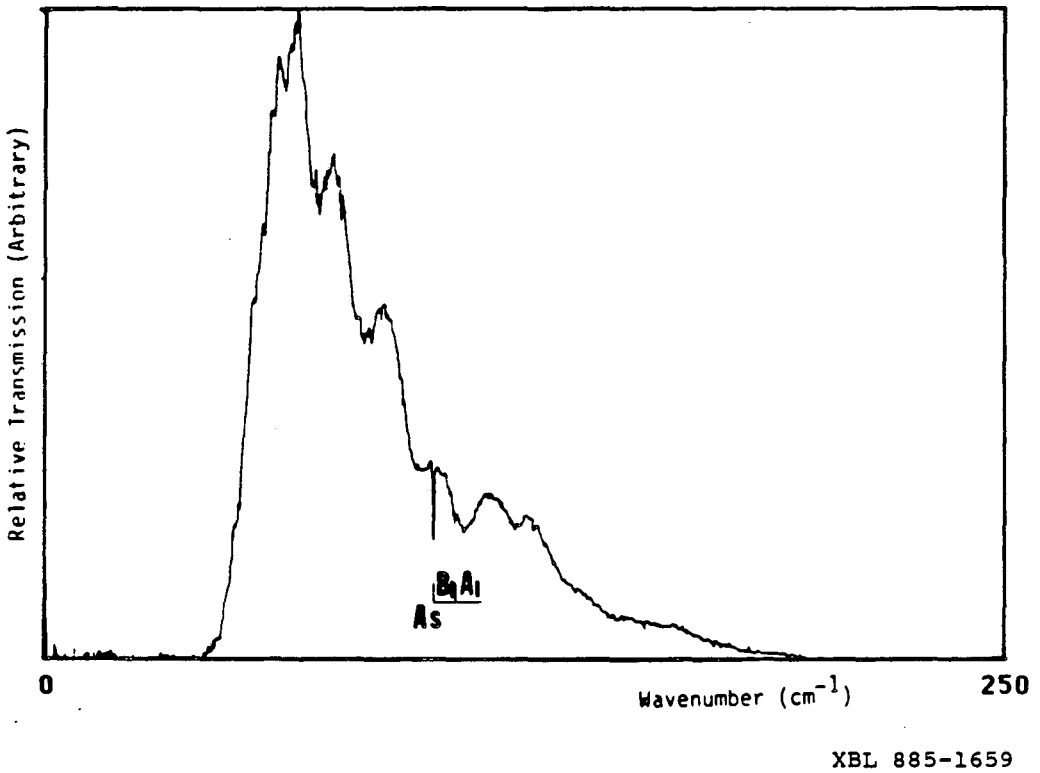

Fig. 2.5(b) Spectrum obtained by the integration of interferogram shown in Fig. 2.5(a)

receives information only in a narrow band at a given time. This is a statement of the Fellgett or multiplex advantage.

The interferometer can be operated with small f numbers or with large solid angles at the source and detector with no strong limitation on the resolution. This ability of interferometers to collect large amounts of energy at high resolution was expressed by Jacquinot as a throughput or <u>etendue</u> advantage of interferometers over spectrometers.

In the real measurement of the absorption spectrum, one cannot

scan the mirror from minus infinity to plus infinity. Instead, the movable mirror is scanned over a fixed distance. This limits the resolution of the absorption peaks in the spectrum. The absorption peak produced in the spectrum is the convolution between the natural linewidth and the instrumental lineshape. The instrument has a finite resolution because of the finite mirror movement and IR source size.

To calculate the resolution limit of the instrument, we first consider the monochromatic source. The interferogram cannot be scanned to infinity in a real measurement, but from $\delta = -L$ to $\delta = +L$. The basic equation now becomes:

$$B(\nu) = \int_{-L}^{L} [I(l) - \frac{1}{2}I(0)]\cos(2\pi\nu l)dl \qquad (2.27)$$

Upon integrating:

$$B(\nu) = 2L \frac{\sin[2\pi(\nu_1 + \nu)L]}{2\pi(\nu_1 + \nu)L} + \frac{\sin[2\pi(\nu_1 - \nu)L]}{2\pi(\nu_1 - \nu)L} \qquad (2.28)$$

By neglecting the first term which is much smaller than the second term, we get the spectrum of a monochromatic source produced by transforming an interferogram with a finite maximum optical path displacement:

$$B(\nu) \sim 2L(\sin z)/z = 2L\mathrm{sinc}\ z \qquad (2.29)$$

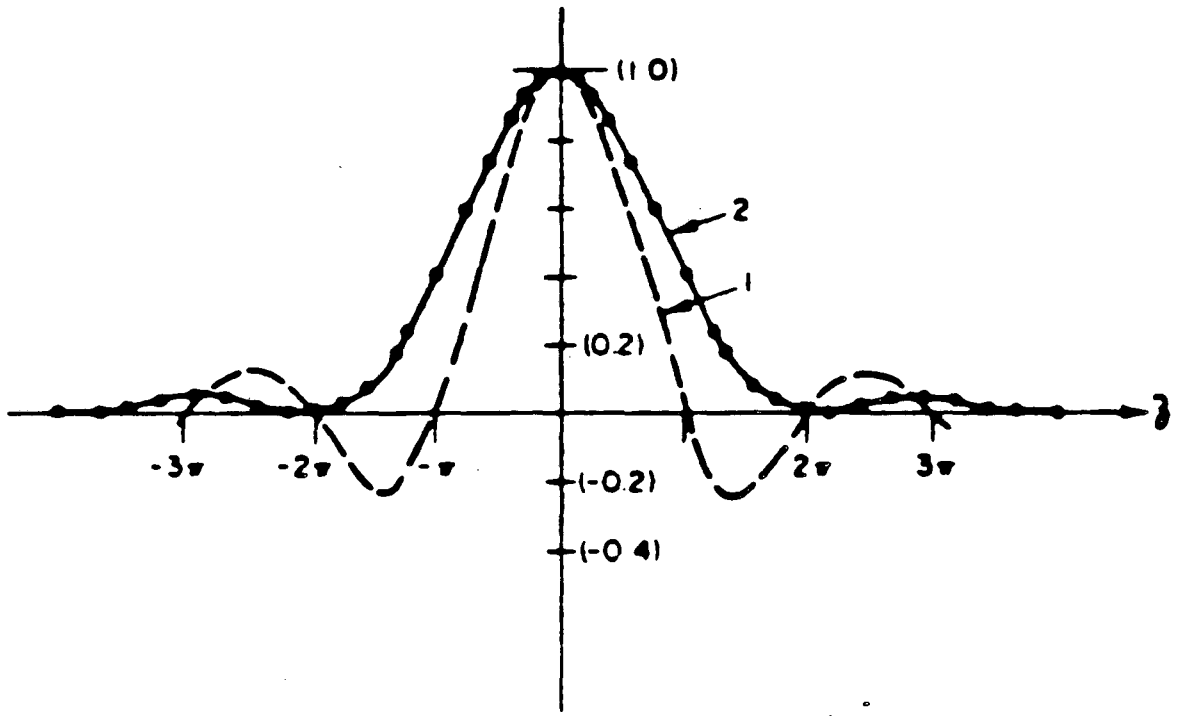

XBL 885-1660

Fig. 2.6 Instrumental line shape function 2Lsinc z (1) and the same function after apodization with a triangular function (2).

where

$$z = 2\pi(\nu_1 - \nu)L \tag{2.20}$$

The above equation is the instrument line shape function (ILS). For a monochromatic source, the line shape function produces a peak with a width of 2π at zero intensity as shown in Fig. 2.6. Furthermore, the peak has "sidelobes" or "feet" droping below zero by as much as 22 of the peak intensity. The "feet" would appear as a false source of

energy at the nearby wavelengths. We use "apodization" to reduce this error. In this thesis work, a triangular apodization was used. We multiply the interferogram with a triangular function $f = 1 - |\delta|/L$. We now obtain an instrument line shape function:

$$B(\nu) = L\,\mathrm{sinc}^2\left(\frac{z}{2}\right) \tag{2.31}$$

instead of equation 2.30. By this process, the width of the peak is increased somewhat, but not seriously, and negative intensities disappear as shown in Fig. 2.6.

In deriving the instrumental resolution limit, we assume the Rayleigh criterion which states that two resonances are resolved if they are separated such that the peak of one resonance falls at the first zero of the second resonance. The resolution limit for a triangularly apodized interferogram using the Rayleigh criterion with a phase difference of 2π is:

$$\nu' - \nu_0 = \delta\nu = \frac{1}{L} \tag{2.32}$$

i.e., the resolution of a Fourier transform spectrometer varies linearly as the maximum optical path difference used to obtain the interferogram.

2.2.3 Experimental Set Up

We used the far-infrared Michelson interferometer with a mercury arc lamp as the light source built by J. Kahn [63]. The maximum moving distance of the mirror of the instrument is 25 cm which gives a maximum resolution of 0.025 cm^{-1} (16 μeV). The instrument can cover a wavenumber range of 5 - 1000 cm^{-1}. The details of the spectrometer used in this thesis work are explained elsewhere [63].

For the characterization of radiation defects and transmutated impurities in NTD germanium, a special absorption rig was built. As shown schematically in Fig. 2.7, it consists of a beam pipe, cold spectral filters, rotating sample holder, a Winston cone [64], and a detector in an integrating cavity. To measure several different samples under the same conditions, the rig was designed to hold up to five samples which can be rotated into the measurement position. For the spectral range required, a black polyethylene (8 mil thick) and a homemade Yoshinaga-type low-pass filter (LiF powder + polyethylene) [65,66] were used.

As we are mainly interested in the shallow impurities in germanium, we used a stressed gallium doped germanium photoconductor as a detector in the system [67]. This detector has a photoconductive response range of 50 ~ 250 cm^{-1} which covers all the shallow impurities/defects in germanium. The peak responsivity of the detector is about 10 A/W at 60 cm^{-1} and to further improve the signal-to-noise ratio, the detector was mounted in an integrating cavity.

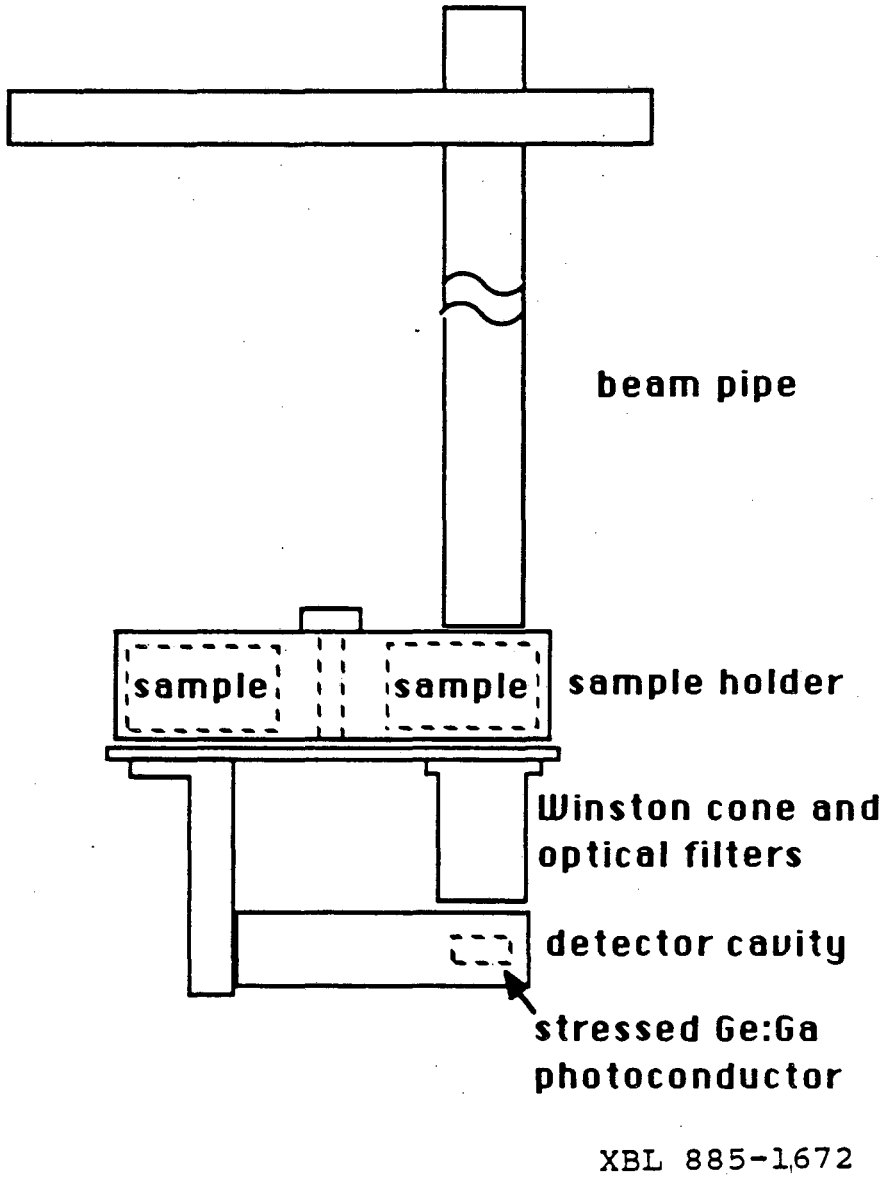

Fig. 2.7 Schematic of IR rig used in our absorption spectroscopy.

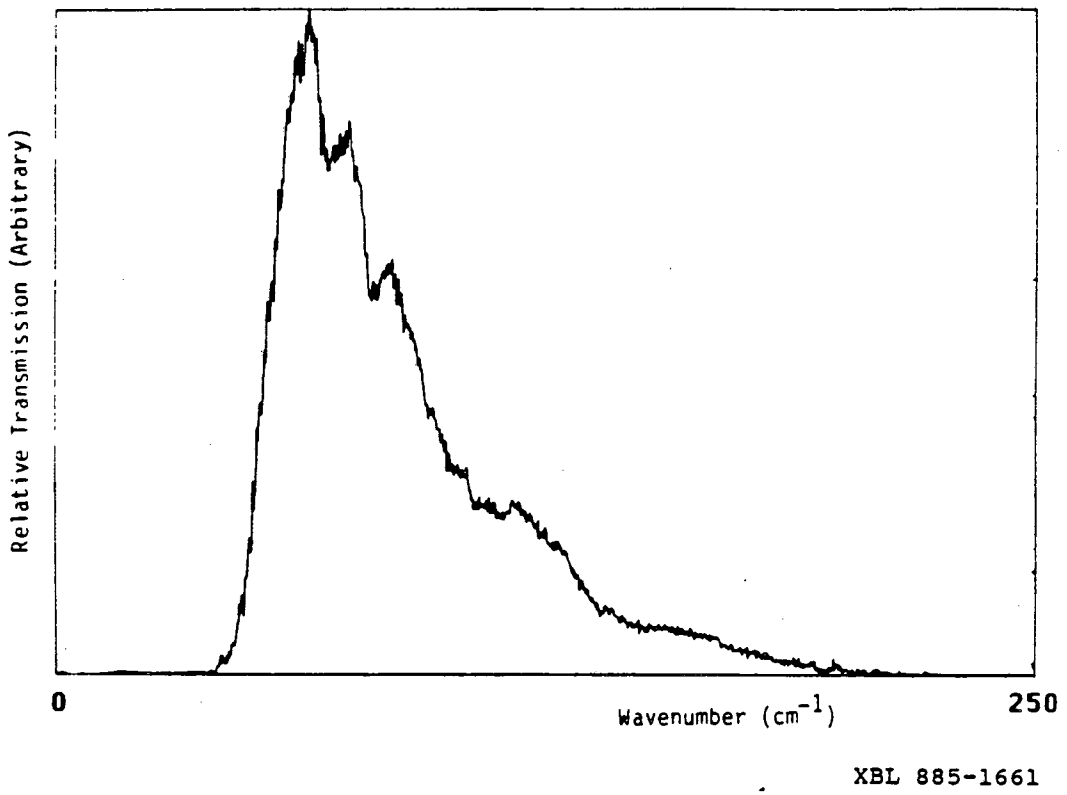

Fig. 2.8 Spectral response of stressed Ge:Ga photoconductor used in our absorption spectroscopy.

Figure 2.8 shows the spectral response of the detector from 0 to 250 cm^{-1} with no sample in front of it. The photoconductive response starts at around 50 cm^{-1} and sharply increases to a peak at around 60 cm^{-1}. It slowly decreases as the wavenumber increases, and at ~ 200 cm^{-1} it almost approaches zero. The 1/2 mil thick mylar beam splitter used has its peak at 125 cm^{-1} and approaches zero at 0 cm^{-1} and 250 cm^{-1}. The lowpass filter has a cutoff at about 200 cm^{-1}. The decrease of the detector response at high wavenumber region reflects the effect of all this optical system combined. Figure 2.9 shows an absorption spectrum taken with a

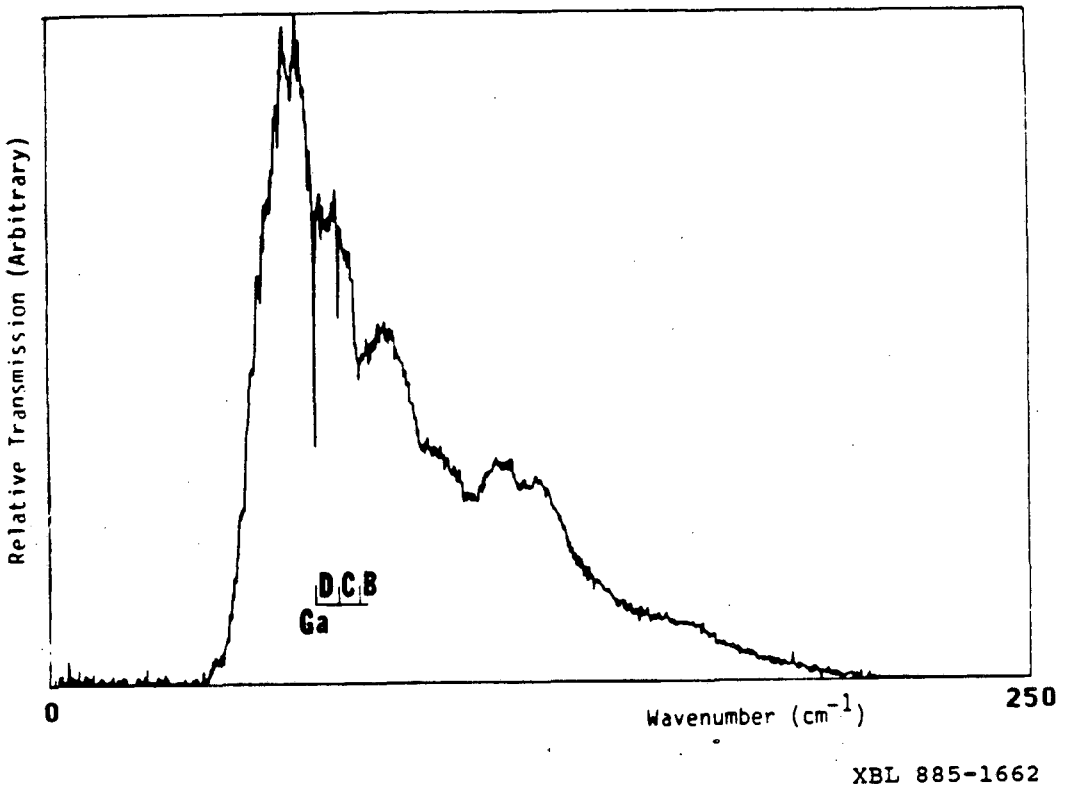

Fig. 2.9 A spectrum measured with a gallium doped germanium sample in front of the detector.

germanium sample in front of the detector. The general shape of the spectrum does not change, but we can see conspicuous absorption peaks corresponding to photons absorbed by the excitations from the ground state to one of the bound excited states of the impurity (in this case gallium), designated as D, C, B and A lines after Jones and Fisher [61]. By determining the energies of the absorption peaks, the impurity is easily identified as gallium. Because each shallow impurity species produces many well defined absorption peaks, there is a great amount of redundance in determining the impurity species. A faulty identification is almost impossible, though some series of

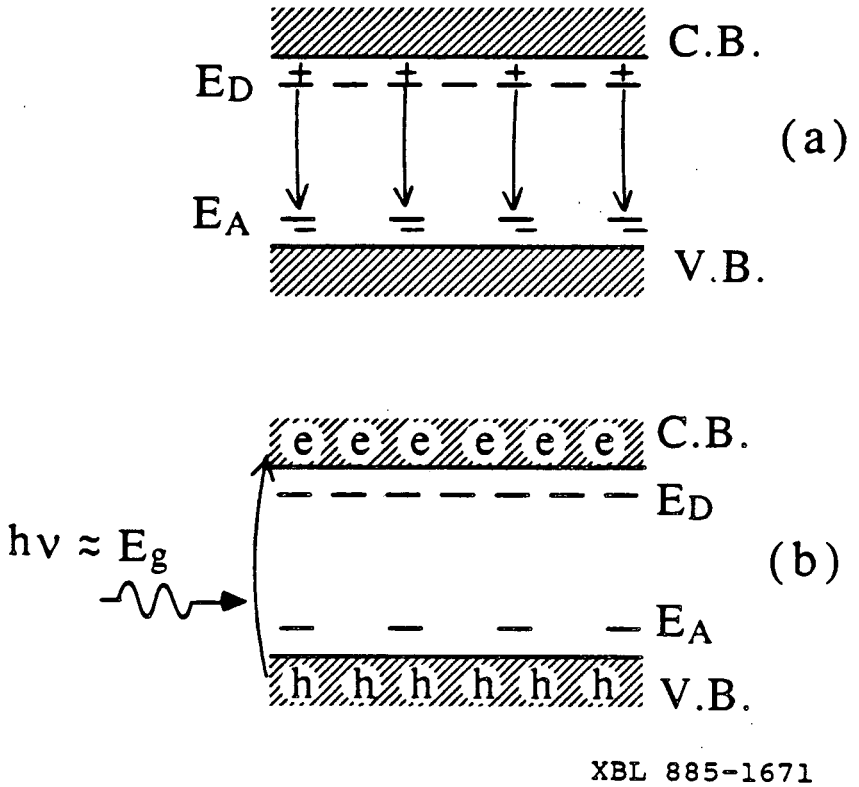

Fig. 2.10 Energy diagram showing a compensated semiconductor (a), and the effect of bandedge light illumination (b).

absorption lines may be almost identical [60].

The strength of the absorption peaks is used to find the concentration of the impurity. It will be discussed in section 3.2.1.

In compensated semiconductors, however, the absorption measurement, like other electrical measurements, reveals only the majority impurities. As shown in Fig. 2.10(a), all the minority impurity levels and the same number of majority impurity levels are ionized at all temperatures. Therefore, only $N_A - N_D$ impurities can contribute to the absorption. As we are interested in NTD

germanium which is a compensated semiconductor, we wish to observe both acceptors and donors at the same time. By using bandedge light illumination, i.e., light with energy just enough to excite electron-hole pairs across the bandgap of the semiconductor, it is possible to make minority dopants accessible for IR absorption spectroscopy [68]. The excess electrons and holes produced by bandedge light neutralize all the ionized impurity levels and all the impurities will contribute to the absorption peaks. Figure 2.10(b) shows this process. The effect of bandedge light on the absorption measurement is shown in Figs. 2.11 and 2.12. In Fig. 2.11(a), an absorption spectrum of a p-type germanium sample is shown. The sample is gallium-doped germanium and the net acceptor concentration is 3×10^{13} cm^{-3} measured by Hall effect measurement at 77 K. When we shine bandedge light on the sample, the spectrum shows additional series of absorption peaks besides the ones of gallium. This is shown in Fig. 2.11(b). The additional peaks are the absorption peaks of arsenic donors with a concentration of about 3×10^{13} cm^{-3} (as obtained from Fig. 3.6 in section 3.2.1). Also, in Fig. 2.11(b), the absorption peaks of gallium are stronger than those in Fig. 2.11(a) because all the gallium impurity became neutral by the bandedge light. The same effect in n-type germanium is shown in Fig. 2.12. Here the total concentration of arsenic is 6×10^{13} cm^{-1} and the concentration of the compensating impurity (gallium) is 3×10^{13} cm^{-3}.

We used the high energy part of the radiation source (the mercury arc lamp) as the bandedge light by putting the low-pass filter next to

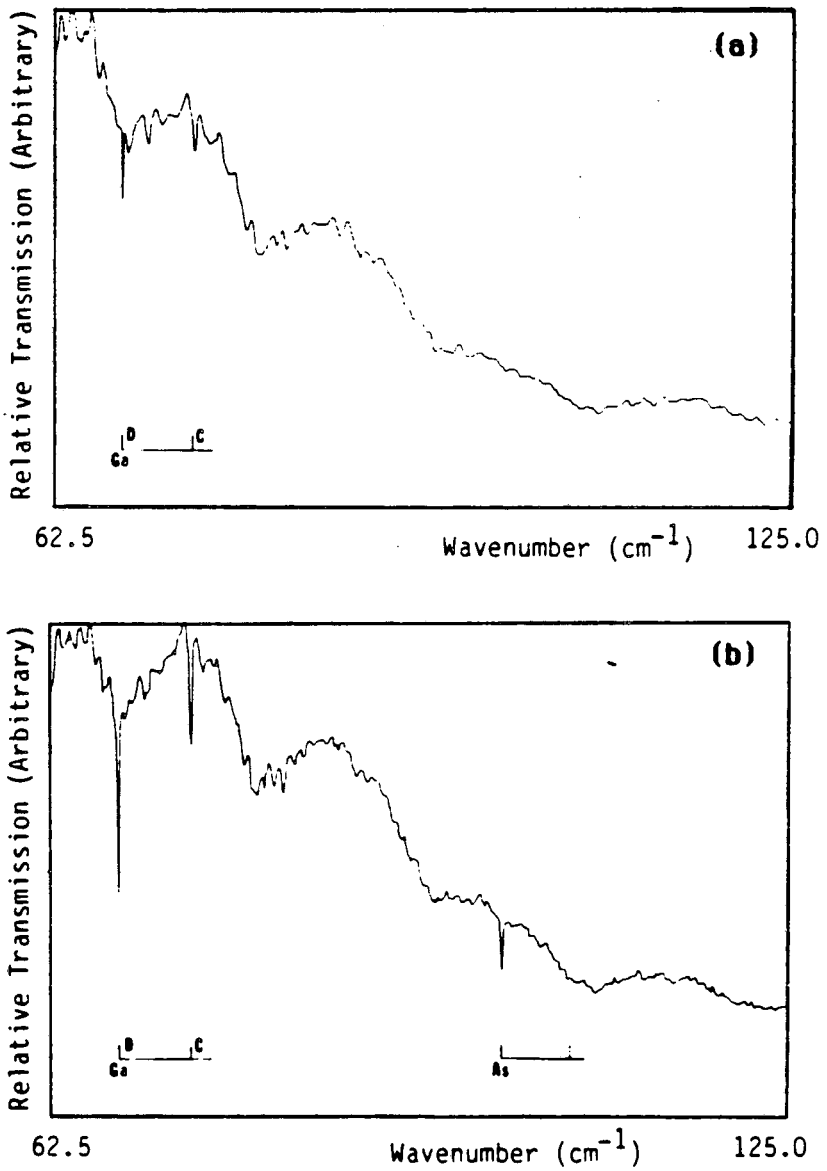

XBL 885-1676

Fig. 2.11 Illustration of the effect of bandedge light illumination in absorption spectroscopy of p-type germanium. (a) without bandedge light, (b) with bandedge light.

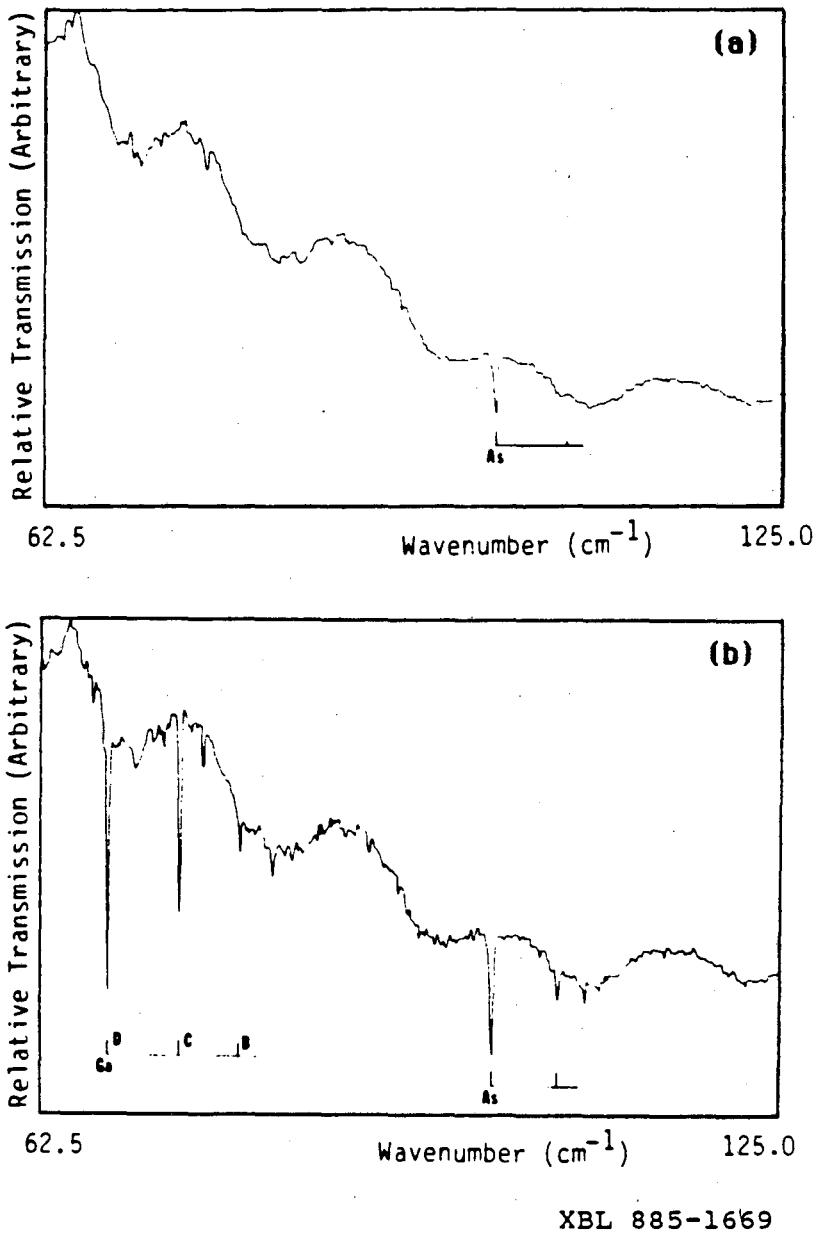

Fig. 2.12 Illustration of the effect of bandedge light illumination in absorption spectroscopy of n-type germanium. (a) without bandedge light, (b) with bandedge light.

the sample. When we want to remove the bandedge light, we insert a thin, pure germanium slice in front of the sample to cut off the higher energy photons.

2.3 Deep Level Transient Spectroscopy (DLTS)

Deep level transient spectroscopy, introduced by Lang in 1974 [69], is based on the dependence of the emission rate of carriers from deep traps on temperature and on the position of the energy level of the trap in the bandgap. This method was successfully applied to the study of deep levels in high purity germanium by Haller, et al. [70] and by Pearton [71], and is a very valuable technique in studying deep levels in semiconductors.

In DLTS measurement, one measures repetitively, thermally activated capacitance transients of a given time constant. The rate of decay or recovery of capacitance transients caused by the emission of trapped electrons or holes is compared with a standard recovery waveform, which forms a rate window. The output of the electronic processing instrumentation is a maximum when the experimental transient falls within the rate window selected. A number of signal processing schemes are possible, including use of a boxcar integrator, lock-in amplifier or correlator.

DLTS requires the sample to be a p-n or Schottky diode. Bias reduction pulses are applied periodically to the reverse biased sample. Accordingly, the ionized traps in the depletion region of the sample capture carriers during bias reduction and then emit carriers

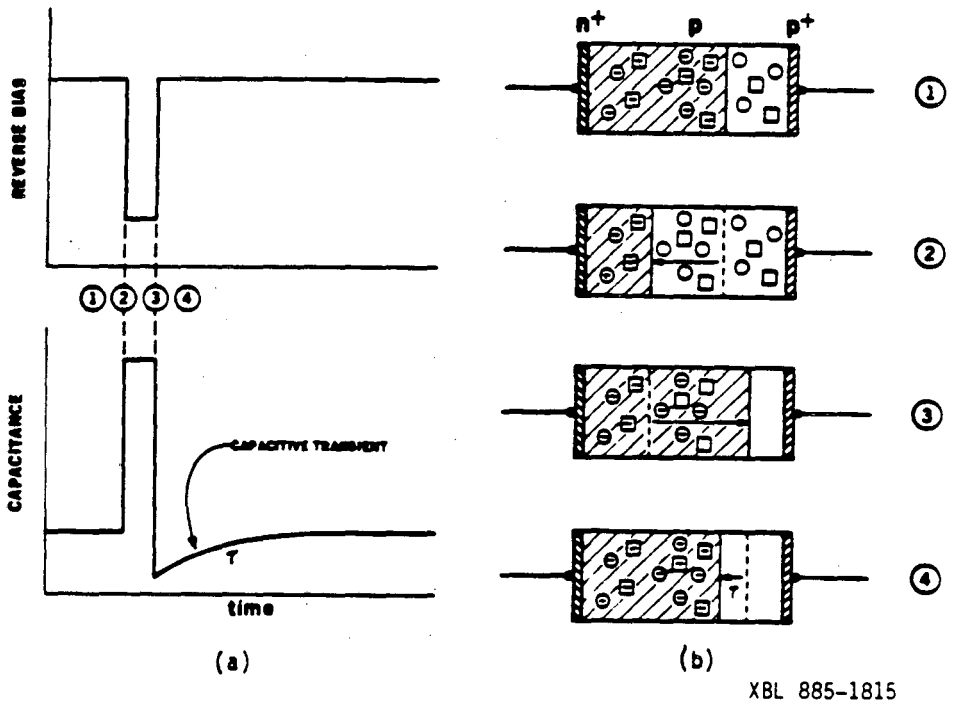

Fig. 2.13 Schematic of DLTS process. (a) the change of bias and capacitance with time, (b) corresponding changes in the depletion region of sample.

with the full bias reapplied. The shallow traps react instantaneously to the bias change but deep traps reemit carriers slowly with a time constant after the pulsed bias is removed. As a result of this process, a capacitance transient is produced in the sample and the time dependence of the capacitance is measured by a high sensitivity, fast transient response bridge. The process is shown schematically in Fig. 2.13. In Fig. 2.13(a), the change of the bias and capacitance with time is shown and in Fig. 2.13(b), corresponding changes inside the depletion are shown.

In our study, a Miller correlator is used. This instrument generates an exponential waveform whose decay rate is externally controlled between 1 ms ~ 100 ms. The system temperature was controlled by CTI model 21* closed cycle refrigerator and a heater resistor. With this system, we could scan the temperature between 20 K ~ 400 K.

2.3.1 Calculation of Trap Energy

The time constant τ of the recovery of the sample capacitance depends on the trap energy and temperature as:

$$\tau = \frac{g}{\sigma \langle v \rangle N} \exp\left(\frac{\Delta E}{kT}\right) \tag{2.33}$$

σ = capture cross section of the trap for carriers, $\langle v \rangle$ = average thermal velocity of the carrier at temperature T, g = degeneracy of the trap (this is unknown for most deep levels and is assumed to be

2), N = density of states in conduction or valence band at temperature T, ΔE = energy of the trap, and k = Boltzmann constant. The DLTS response is measured for several different time constants. The position (temperature) of the peak of deep levels changes as the time constant is changed because the emission rate e (= $1/\tau$) depends on the temperature. A plot of $\ln \tau$ vs. 1/T will yield a straight line with slope $\Delta E/k$ (for the simplest case and one trap present). We can calculate the trap energy from the slope. The alternative for getting the trap energy from a plot is to plot $\ln (e/T^2)$ vs. 1/T. In this way, the temperature dependence of the pre-exponential factor is accounted for (as $\langle v \rangle \sim T^{1/2}$ and $N \sim T^{3/2}$, the product of these two terms yields T^2-dependence). In this study we plot $\ln e/T^2$ vs. 1/T for trap energy calculations.

2.3.2 Trap Capture Cross Sections

The capture cross section can be obtained in two ways. One is to use the intercept in $\ln \tau$ v.s. 1/T plot. The intercept in the plot corresponds to $\ln (g/\sigma\langle v\rangle N)$. $\langle v \rangle$ and N can be calculated with known parameters at temperature T, and g is assumed to be 2. From the intercept value obtained in the plot, σ is easily calculated. Another way of obtaining the value of σ is to use the time dependence of trap filling. The number of traps filled depends exponentially on the pulse width (time) as:

$$n(t) = N_T[1 - \exp(\frac{-t}{\tau})] \qquad (2.34)$$

$n(t)$ = number of traps filled for pulse width t, N_T = trap concentration, and τ = time constant of trap emission. The above equation can be rewritten as:

$$\frac{N_T - n(t)}{N_T} = \exp\left(\frac{-t}{\tau}\right) \tag{2.35}$$

or

$$\ln \frac{N_T - n(t)}{N_T} = \frac{-t}{\tau} \tag{2.36}$$

A plot of $\ln [N_T - n(t)]/N_T$ vs. t yields slope $1/\tau = \sigma\langle v\rangle n$. The cross section is:

$$\sigma = (\tau\langle v\rangle n)^{-1} \tag{2.37}$$

where n is the doping density of the sample. The cross section values obtained usually range $10^{-14} \sim 10^{-18}$ cm^2.

2.3.3 Trap Concentration

Due to the presence of deep traps in the depletion region, the capacitance changes exponentially with time after the plused bias is removed. The relation between the capacitance and the carrier concentration is:

$$C = \left[\frac{\varepsilon e(N_D - N_A)}{2(V_{bi} + V)}\right]^{\frac{1}{2}} \tag{2.38}$$

ε is the dielectric constant, $N_D - N_A$ is the net carrier concentration, V_{bi} is the built in bias, and V is the applied bias. When the deep trap has not been filled fully:

$$\frac{C(t)}{C} = \frac{\left[\dfrac{\varepsilon e(N_D - N_A - N_T \exp(\frac{-t}{\tau})}{2(V_{bi} + V)}\right]^{\frac{1}{2}}}{\left[\dfrac{\varepsilon e(N_D - N_A)}{2(V_{bi} + V)}\right]^{\frac{1}{2}}} \tag{2.39}$$

or:

$$\frac{C(t)}{C} = \left[\frac{N_D - N_A - N_T \exp(\frac{-t}{\tau})}{N_D - N_A}\right]^{\frac{1}{2}} = \left[1 - \frac{N_T \exp(\frac{-t}{\tau})}{N_D - N_A}\right]^{\frac{1}{2}} \tag{2.40}$$

If $N_T << N_D - N_A$, the equation becomes:

$$\frac{C(t)}{C} = 1 - \frac{1}{2}\frac{N_T \exp(\frac{-t}{\tau})}{N_D - N_A} \tag{2.41}$$

or:

$$\frac{C - C(t)}{C} = \frac{\Delta C}{C} = \frac{1}{2}\frac{N_T \exp(\frac{-t}{\tau})}{N_D - N_A} \tag{2.42}$$

From this relation, the trap concentration is obtained as:

$$N_T = 2 \frac{\Delta C_{max}}{C} (N_D - N_A) \tag{2.43}$$

ΔC can be read from the oscilloscope, C is the reverse bias capacitance, and $N_D - N_A$ is the net doping concentration of the sample. This equation applies only when $N_T << N_D - N_A$ with one majority deep trap present.

3. Results and Discussion

3.1 Hall Effect Measurements: Free Carrier Concentration and Mobility

3.1.1 Determination of the Compensation Ratio of NTD Germanium

As a result of thermal neutron irradiation of germanium, three different dopant elements are produced by transmutation: gallium, arsenic, and selenium. As already explained in section 1.2.2, the compensation ratio of NTD germanium for a specific reactor used can be approximated by measuring the free carrier concentration of NTD germanium as a function of time after neutron irradiation.

A more systematic way of calculating the exact compensation ratio of NTD germanium was reported by Zabrodskii in 1981 [72]. He used the radioactive decay equation to get the exact compensation ratio and the half life of the gallium producing reaction.

As the arsenic producing reaction has a very short half-life (82.8 min), the reaction is very close to complete one day after neutron irradiation. The selenium producing reaction has a half-life of 32.2 hours (dominant process) and about 5 days after neutron irradiation, the reaction is over 90% completed. As the contribution of selenium to the total number of donor is very small (~ 6%), the rest of the reaction can be neglected. The net carrier concentration C as a function of time after ~ 5 days can be described in good approximation by:

$$C(t) = N_{Ga}[1 - \exp(-\frac{\ln 2}{\tau}t)] - N_D \tag{3.1}$$

When n- to p-type conversion of NTD germanium takes place at $t = t_o$, $C(t_o) = 0$ and the compensation ratio K is:

$$K = \frac{N_D}{N_{Ga}} = 1 - \exp(-\frac{\ln 2}{\tau}t)] \tag{3.2}$$

By measuring the time for n- to p-type conversion of the NTD germanium sample after neutron irradiation, the compensation ratio can be computed with equation 3.2.

We prepared two pure germanium slices with residual acceptor concentrations of less than 10^{10} cm^{-3}. By choosing a very pure germanium sample we can neglect the effect of the residual impurities in the unirradiated sample. These slices were then irradiated with neutrons with dose of 5×10^{14} cm^{-2} and 3×10^{15} cm^{-2},

respectively at Berkeley Research Reactor [73]. At the central thimble of the reactor the neutron flux is 4×10^{12} cm^{-2} sec^{-1} at a reactor power of 100 kW. The first sample was irradiated for 2.08 min and the second sample was irradiated 12.5 min at 100 kW of reactor power, respectively. The irradiation time required to get the desired neutron fluence is negligible compared to the time scale (several days) over which we measure the carrier concentration of the samples. The ratio of thermal neutron to fast neutron was 4.

Immediately after neutron irradiation, the slices were annealed at 400°C for 4 hr to remove the radiation damage. Precautions were taken so that there is no contamination by fast-diffusing copper during annealing process. This is done by soaking the samples in a 10% KCN in H_2O solution for about 10 min after they have been polish etched in HNO_3:HF (3:1) solution and then rinsed with deionized water. The free carrier concentration of each sample was measured with a Hall effect measurement at 77 K as a function of time after annealing. The measurements were done about twice a day.

For samples in the n-type state (before the NTD germanium sample changes into p-type, at about 6 days after neutron irradiation), lithium-diffused contacts worked as good ohmic contacts. For samples in the p-type state (after n- to p-type conversion), indium-alloy contacts worked satisfactorily.

Figure 3.1 shows the result of measurements from 3 to 15 days after neutron irradiation. Also shown is the theoretical curve calculated by using the cross section values from reference [26] which gives a compensation ratio of 0.32. Both samples have n-type carriers

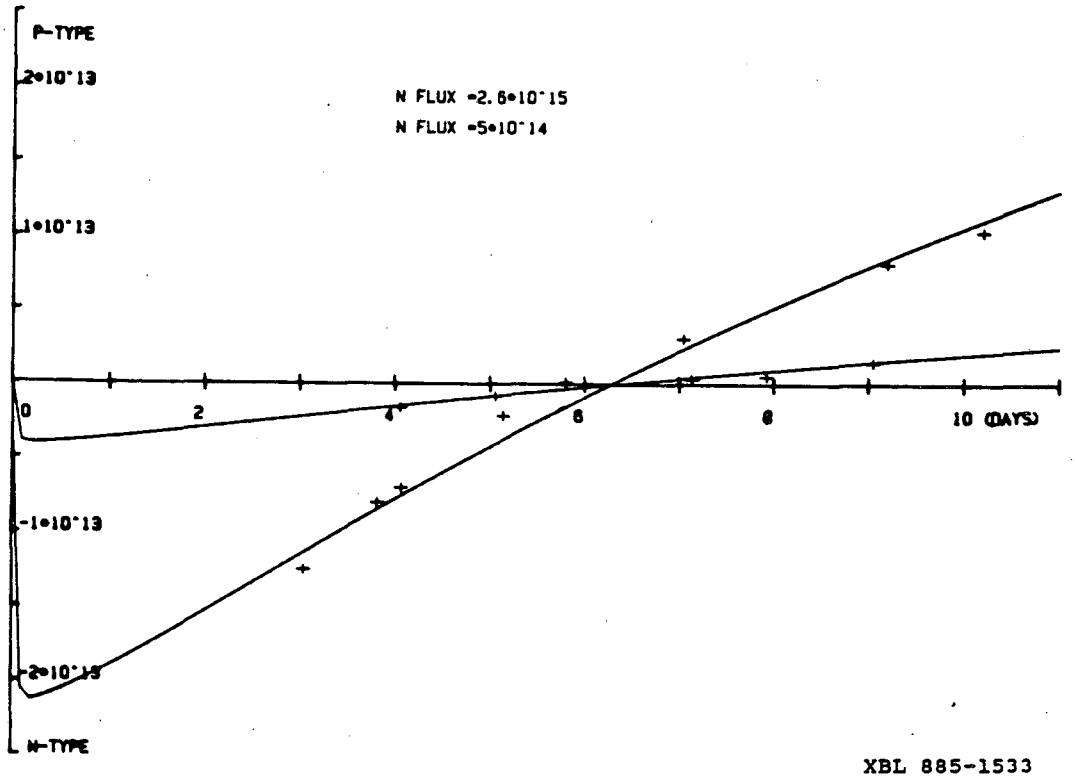

Fig. 3.1 Measurement fo net carrier concentration of NTD germanium as a function of time after neutron irradiation.

(mostly arsenic and some selenium) at first. But in the n-type region of the measurement, one measures only the arsenic concentration because selenium which is a deep double donor does not contribute electrons at 77 K. This does not affect the measurement significantly because of the very small contribution of selenium to the total donor concentration. The n-type carrier concentration slowly decreases because the donors are compensated by newly produced gallium acceptors. 5.9 days after neutron irradiation, both samples are exactly compensated, i.e., $N_A - N_D = 0$. After this time the gallium acceptors slowly overcompensate the donors. As is shown, both

curves meet at N = 0 on the x-axis meaning that there was no contamination of any other impurity during annealing stage (see discussions in section 1.2.2). By using equation 3.2 and the half-life for the gallium producing reaction of 11.2 days, the compensation ratio of NTD germanium irradiated at the Berkeley Research Reactor is found to be 0.306 [74].

3.1.2 Free Carrier Concentration of NTD Germanium

The presence of radiation defects in NTD germanium can be detected firstly by measuring the carrier concentration without removing the radiation damage. The carrier concentration of a neutron irradiated, unannealed sample is much larger than that expected from the thermal neutron produced shallow impurities. Annealing the sample after neutron irradiation decreases the carrier concentration. Figure 3.2 shows the net carrier concentrations of NTD germanium samples, neutron irradiated and annealed at different temperatures for 1 hr. The neutron irradiation was done at the Berkeley research reactor at room temperature and the total neutron dose was 2×10^{15} cm^{-2}. Again the cadmium ratio was 4. The carrier concentration was measured by Hall effect at 77 K. Measurements were made from 12 to 22 days after neutron irradiation when the samples already converted into p-type to show the presence of radiation defects more clearly. As shown in the figure, the p-type carrier concentration of the sample annealed at 500°C [NTD(5)] increases as time passes meaning that ^{70}Ge is still in the process of transmutation into gallium impurity. The measured

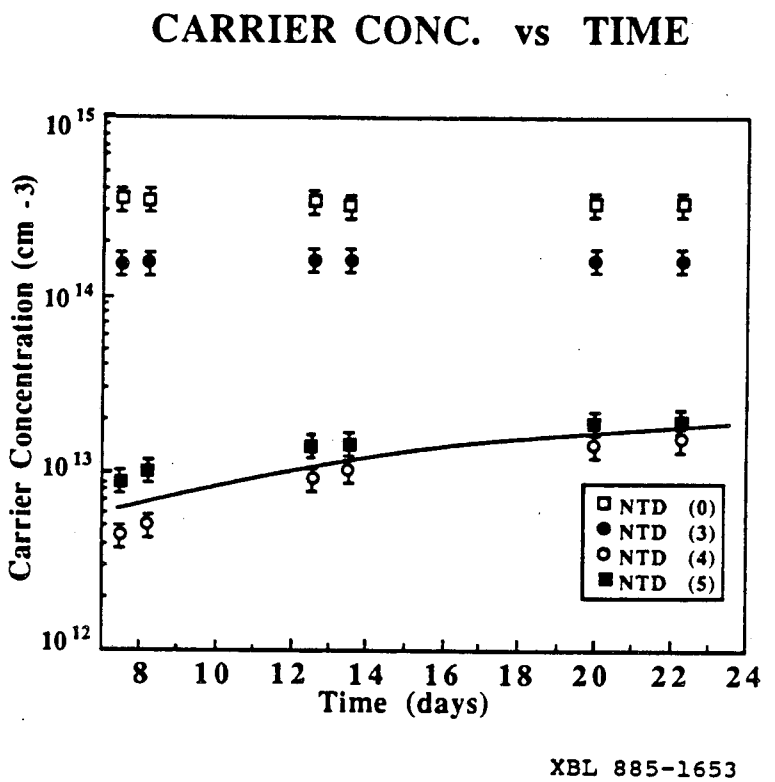

Fig. 3.2 Net carrier concentration of NTD germanium for different annealing temperatures measured for several days after neutron irradiation.

carrier concentration is close to the calculated one given by the solid curve and we conclude that most of the radiation damage has been removed by annealing at 500°C for 1 hr.

The sample annealed at 400°C for 1 hr [NTD(4)] also shows the same behavior with the concentration smaller than that of sample annealed at 500°C. It is believed that the sample annealed at 500°C may have been contaminated by fast-diffusing copper during the annealing stage. The maximum solid solubility of copper in germanium at 500°C is about 1 x 10^{13} cm^{-3} [75]. Each substitutional copper acceptor

has three energy levels. At 77 K only the first hole can be ionized from the E_v + 43 meV level. Therefore, the maximum contribution of holes from copper is expected to be about 1×10^{13} cm^{-3} at 77 K. The difference in the carrier concentration of the sample annealed at 400°C and 500°C is about 5×10^{12} cm^{-3} which can easily be explained by a small copper contamination.

The sample denoted NTD(0) which stands for "unannealed sample" experienced some limited annealing during the contact fabrication process. The sample was heated for 40 sec to 160°C which appears to be negligible compared to the other annealing conditions. Thus this "unannealed sample" serves as reference. The carrier concentration of the unannealed sample shows a behavior totally different from the annealed samples. First of all, the net carrier concentration is much higher (~ 3×10^{14} cm^{-3}) than that of fully annealed (400°C or 500°C) samples. It also exceeds the calculated values. Furthermore the carrier concentration does not change as time passes. We explain this behavior with the presence of radiation defects. The fast neutrons produce defect clusters and point defects by knocking germanium atoms from their substitutional positions. The defect clusters, vacancies, interstitials and defect-impurity complexes contribute to the increased p-type carrier concentration. As the number of displaced germanium atoms produced by fast neutrons is very large (on the average, we obtain 10^3 displacements for each fast neutron knock-on), the concentration of this defect-related acceptors is much higher than the concentration of gallium produced by transmutation. Therefore, the measured net-carrier concentration of

the unannealed sample dose not change measurably with time because the contribution of the growing gallium concentration to the total carrier concentration is negligible.

The sample annealed at 300°C for 1 hr [NTD(3)] shows similar behavior as the unannealed sample. The net carrier concentration has been reduced to some extent (~ 1.5 x 10^{14} cm^{-3}), but is still higher than those of samples annealed at 400°C or 500°C. Also, the carrier concentration does not change with time. At this temperature, most simple defects, single vacancies and interstitials, are believed to be annihilated [48]. Defects present in the sample annealed at 300°C can be higher order complexes of vacancies and interstitials. We estimate that annealing at 300°C for 1 hr removes about 50% of the fast neutron produced radiation defects.

With our results we have shown that the radiation damage in NTD germanium can be removed by annealing at or above 400°C and that the concentration of the radiation defects is about 20 times higher than the resultant net-acceptor concentration.

A quantitative study of the removal of radiation defects by annealing can be obtained by isochronal annealing. Fig. 3.3 shows the change in the free carrier concentration of NTD germanium for different annealing temperatures. The annealing time was 1 hr. From this figure we can conclude that annealing up to 150°C does not change the concentration of free carriers at all. This means that the p-type defects produced by irradiation at room temperature are stable up to 150°C. It has been reported that isolated single defects can move or diffuse below room temperature [37,48,52] and those single defects are

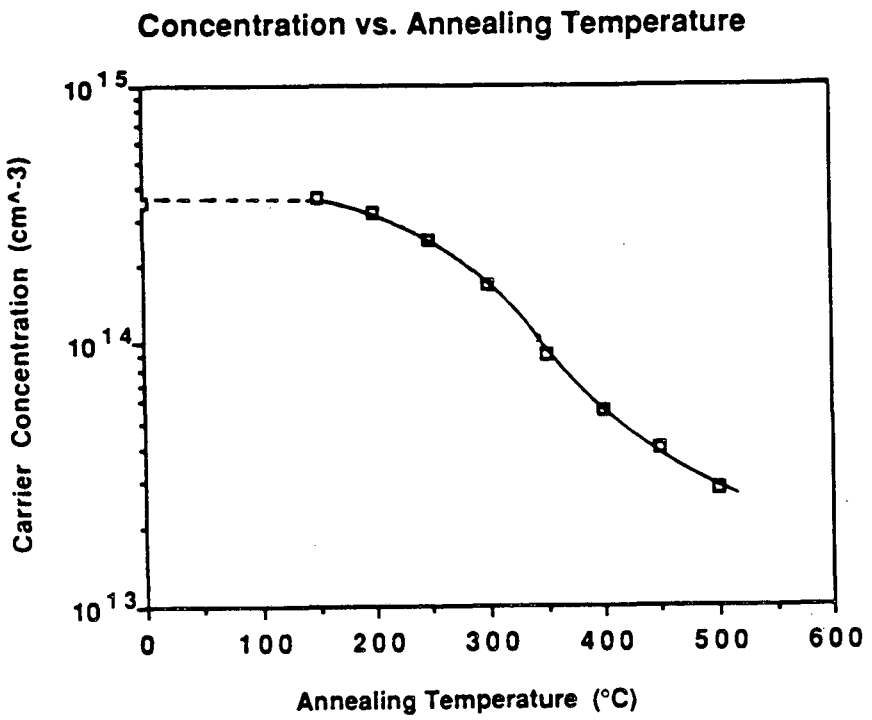

XBL 885-1652

Fig. 3.3 Effect of isochronal annealing on the net carrier concentration of NTD germanium (annealing time is 1 hr).

believed to be annealed out already at room temperature. Therefore the high acceptor concentration measured in the sample annealed up to 150°C must be due to more complicated defects. As the annealing temperature is increased, the acceptor concentration decreases almost linearly with annealing temperature. At an annealing temperature of 500°C, the acceptor concentration reaches a minimum which corresponds to the net-doping concentration by NTD. Unlike the radiation defects produced by light particles, such as energetic electrons or γ rays, the fast neutron damage anneals out only with high temperature annealing which again shows that neutron-induced defects must be

defect complexes.

3.1.3 Free Carrier Mobility of NTD Germanium

The presence of radiation defects and the extent of recovery in NTD germanium can also be observed by the change of carrier mobility after neutron irradiation and annealing.

There are many factors that can affect the carrier mobility in semiconductors. At high temperatures, the dominant factor in determining carrier mobility is the scattering by phonons with a dependence of $T^{-3/2}$ [76]. At low temperatures, scattering by ionized or neutral impurities becomes dominant with a dependence of $T^{3/2}$. In a semiconductor with a large number of defects or impurities, the carrier mobility is dominated by defects or impurities even at 77 K. Therefore, by performing measurements of the carrier mobility at 77 K after neutron irradiation, we can determine the effect of radiation defects on mobility and the extent of removal of the defects as evidenced by a mobility increase.

Figure 3.4 shows 77 K mobility values for NTD germanium after annealing at different temperatures. As expected from the considerations in section 3.1.2., the unannealed sample has the lowest carrier mobility because of the radiation defects present in the sample. As the samples are annealed at increasingly higher temperatures, the carrier mobility increases and above 500°C, the value saturates to a maximum. This confirms the annealing behavior shown in Fig. 3.3.

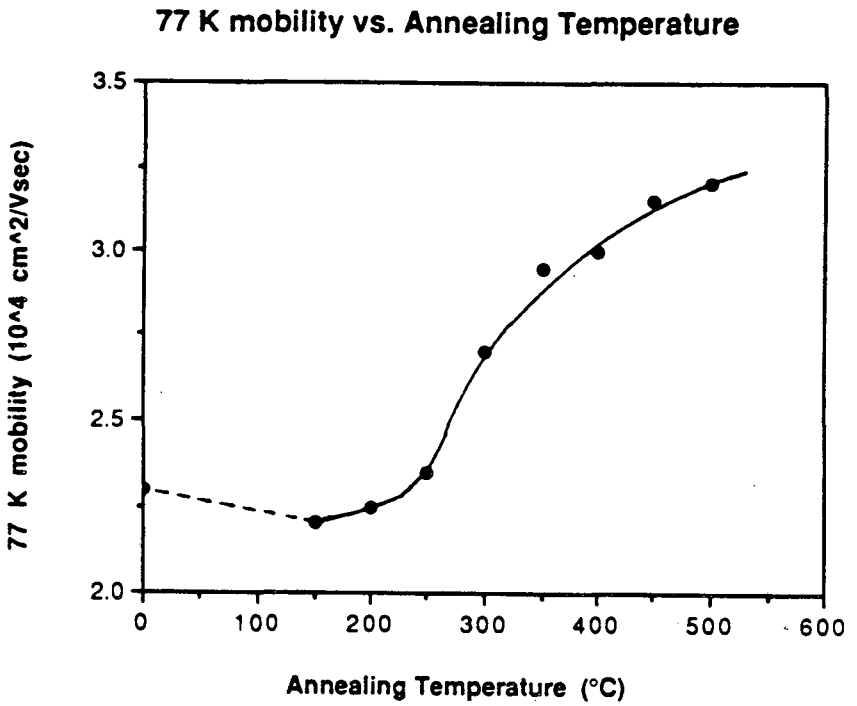

XBL 885-1651

Fig. 3.4 Effect of isochronal annealing on the carrier mobility of NTD germanium (annealing time is 1 hr).

3.1.4 Freeze-Out Curves of NTD Germanium with Radiation Defects

More detailed information about the radiation defects can be obtained from variable temperature Hall effect measurements. From the Arrhenius plot of the free carrier concentration vs. inverse temperature, one can obtain the net-carrier concentration, the ionization energy of the majority dopant and the concentration of compensating impurities. Figure 3.5 shows the results of an unannealed and a fully annealed (500°C) sample. The plot of the fully annealed sample (a) shows the saturation region with net dopant

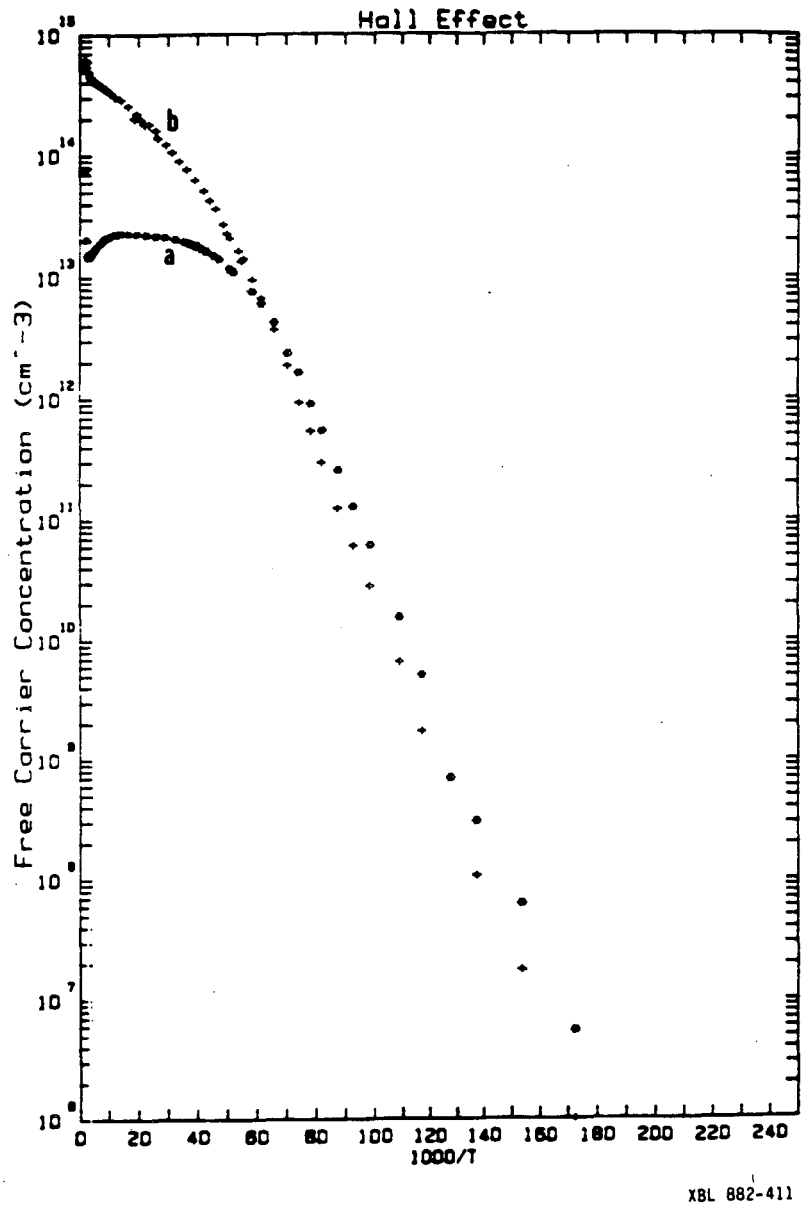

Fig. 3.5 Result of variable temperature Hall effect measurement of fully annealed (a) and unannealed (b) NTD germanium sample.

concentration of 2.5×10^{13} cm^{-3}. The curve starts to freeze out at about 20 K. It shows the half-slope freeze-out of the gallium acceptors followed by the full slope with the ionization energy of 11 meV in excellent agreement with reported value [60]. Here we cannot clearly distinguish the half-slope region because of the high compensation by arsenic donors. The same plot of the unannealed sample (b) looks very different. There is almost no saturation region at high temperatures and the acceptors with a maximum concentration of 4×10^{14} cm^{-3} start to freeze out at room temperature. Although the freeze out curve seems to be a straight line with the ionization energy of about 5 meV, it cannot be the freeze-out of one shallow impurity because the temperature is far too high for freeze-out to start. It can be explained as the freeze-out of a group of deep acceptor levels (due to the radiation damage) which have a continuous, broad range of energy levels. The freeze-out region, therefore, consists of a superposition of many step-like freeze-out curves. More details on these deep levels have been studied by DLTS as will be discussed in section 3.3.

3.2 Infrared Absorption Spectroscopy

3.2.1 Calibration of Infrared Absorption Peaks of Shallow Impurities in Germanium

The absorption coefficient α due to the electronic dipole transitions is linearly dependent upon the carrier concentration of

the sample. IR absorption spectroscopy can be used as a quantitative characterization tool in the study of semicondcutors. One can obtain the concentration of dopant impurities of the sample with a proper calibration.

The ratio between the intensity of the incident and the transmitted beam through the sample is expressed in equation 2.19. Equation 2.19 is a general expression for the absorption process including the reflection at the surface of the sample leading to the multiple internal reflections [77]. This equation is used to obtain the absolute value of the absorption coefficient of a sample. In our measurement, however, we are concerned with the absorption by impurities in germanium. And the strength of the absorption peak is actually compared with that of pure sample. Therefore, there is no need to consider the reflection at the surface in the absorption process. We use a simplified expression in the calculation of absorption coefficient of impurities in germanium by setting R = 0 in equation 3.3:

$$\frac{I}{I_0} = \exp(-\alpha d) \tag{3.3}$$

We obtain the value of I/I_0 from the absorption spectrum. The sample thickness d is measured. The absorption coefficient α is calculated using equation 3.4. As the absorption coefficient α is linearly proportional to the concentration of impurities (equation 2.20), a plot of α vs. the concentration of impurity measured

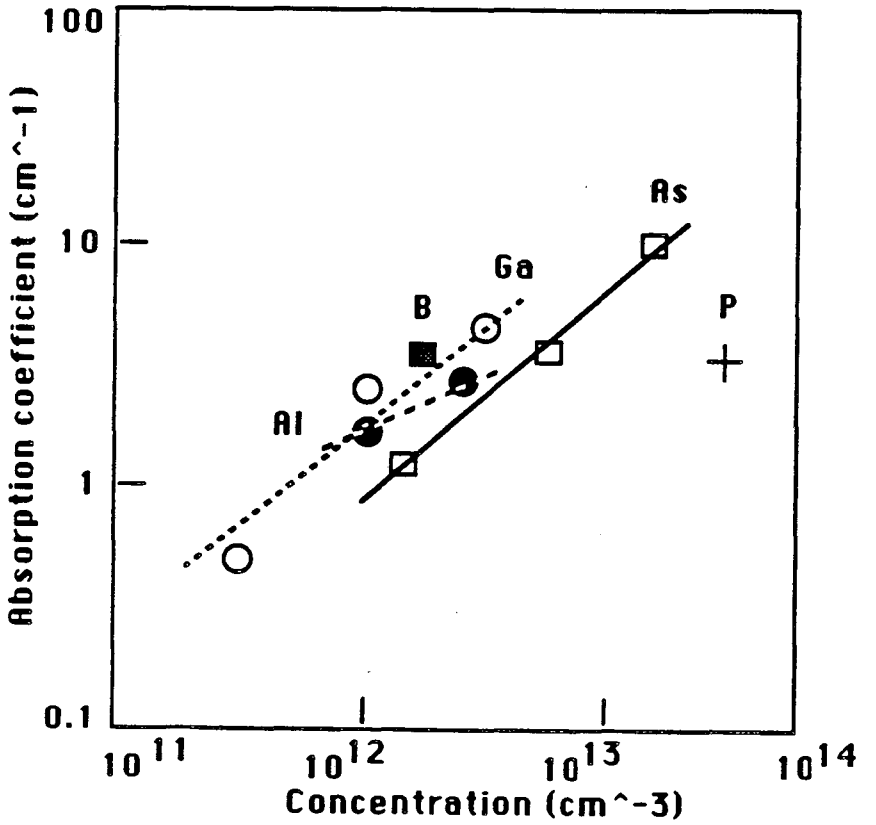

XBL 885-1816

Fig. 3.6 Plot of measured α vs. impurity concentration.

electrically should result in a straight line. The plot made from the measurements of the samples with known impurity concentration is used as a standard to get the concentration of the impurities in unknown samples. The slope of the line in the plot is the absorption cross section σ (equation 2.20) of the impurity.

We have measured the absorption spectrum of germanium standard samples doped with arsenic, phosphorus, gallium, aluminum, and boron with emphasis on arsenic and gallium doped germanium samples. The

doping concentrations of these standard samples were measured with Hall effect at 77 K. Figure 3.6 shows a plot of the absorption coefficient vs. carrier concentration of germanium standard samples. For group III aceptors, D-lines were used in the calculation of α, and for group V donors, $1s \rightarrow 2p_{\pm}$ lines were used. The plot yields a straight line for each impurity. The absorption cross section of arsenic $1s \rightarrow 2p_{\pm}$ line derived from the slope in the plot is 6×10^{-13} cm^2. The slope of gallium absorption coefficient is a smaller than that of arsenic, meaning the smaller absorption cross section. But from the lack of enough data, the value of absorption cross section of other impurities is subject to large error. This plot serves as standard for impurity concentration determination in this thesis.

3.2.2 Absorption Spectra of NTD Germanium

As discussed earlier, IR absorption spectra taken with a bandedge light enable us to observe simutaneously both types of impurities in a sample. This technique is applied to the investigation of NTD germanium to find out the details about the electrically active impurity species.

The absorption spectrum of a neutron-irradiated sample which was annealed at 500°C for 1 hr is shown in Fig. 3.7(a). The spectrum is shown in the wavenumber range 62.5 ~ 125 cm^{-1} (7.8 ~ 15.6 meV). As expected, after full annealing, the absorption peaks of both arsenic donors and gallium acceptors are visible. We cannot observe any other

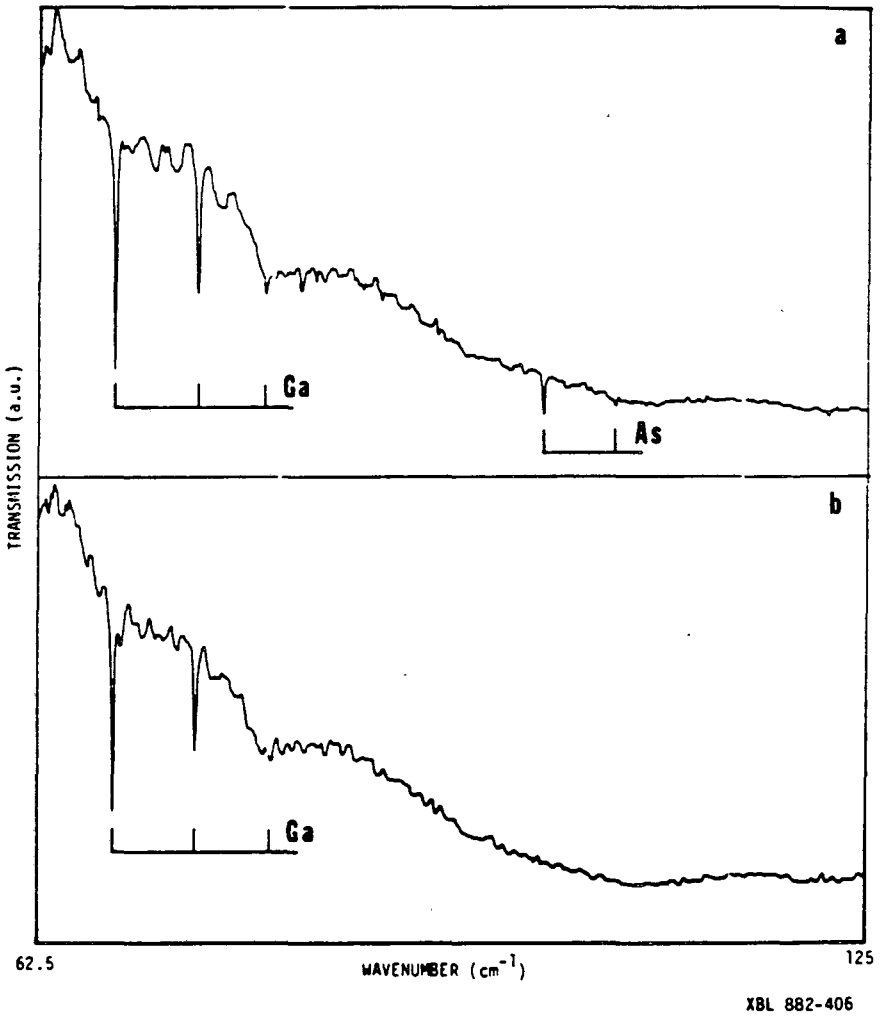

Fig. 3.7 IR absorption spectrum of annealed at 500°C (a) and unannealed (b) NTD germanium sample.

series of absorption peaks than those of gallium and arsenic. This means that there is no electrically active radiation defect present in the shallow energy range with sufficiently large concentration to be seen in the spectrum (~ 10^{11} cm^{-3}).

The absorption spectrum of a neutron irradiated, unannealed germanium sample is shown in Fig. 3.7(b). One obvious difference from Fig. 3.7(a) is that absorption lines of transmutated gallium acceptors are visible without annealing while no arsenic donor lines appear. This means that gallium impurities are active acceptors without annealing while the arsenic impurities are not shallow donors after NTD. From the intensity of the absorption peak (here we used D-line of gallium and $1s \rightarrow 2p_{\pm}$ line of arsenic for the calculation of impurity concentration), it is found that the concentration of electrically active gallium acceptor in both samples is the same to within about 10%. Figure 3.8 shows the absorption spectra of an unannealed sample measured several days after neutron irradiation. The increase of the intensity of gallium acceptor peaks as time passes is clearly visible. The value of α (D- and C-line) is plotted as a function of time in Fig. 3.9. This again comfirms the observed fact that gallium acceptors are electrically active without annealing.

Arsenic impurities in unannealed germanium samples are electrically inactive meaning that either they do not reside in substitutional positions or they form complexes with radiation defects even if they are in the substitutional positions. There exists a large amount of literature on donor-vacancy complexes in irradiated germanium [40 ~ 44]. From the reported work, we conclude that all

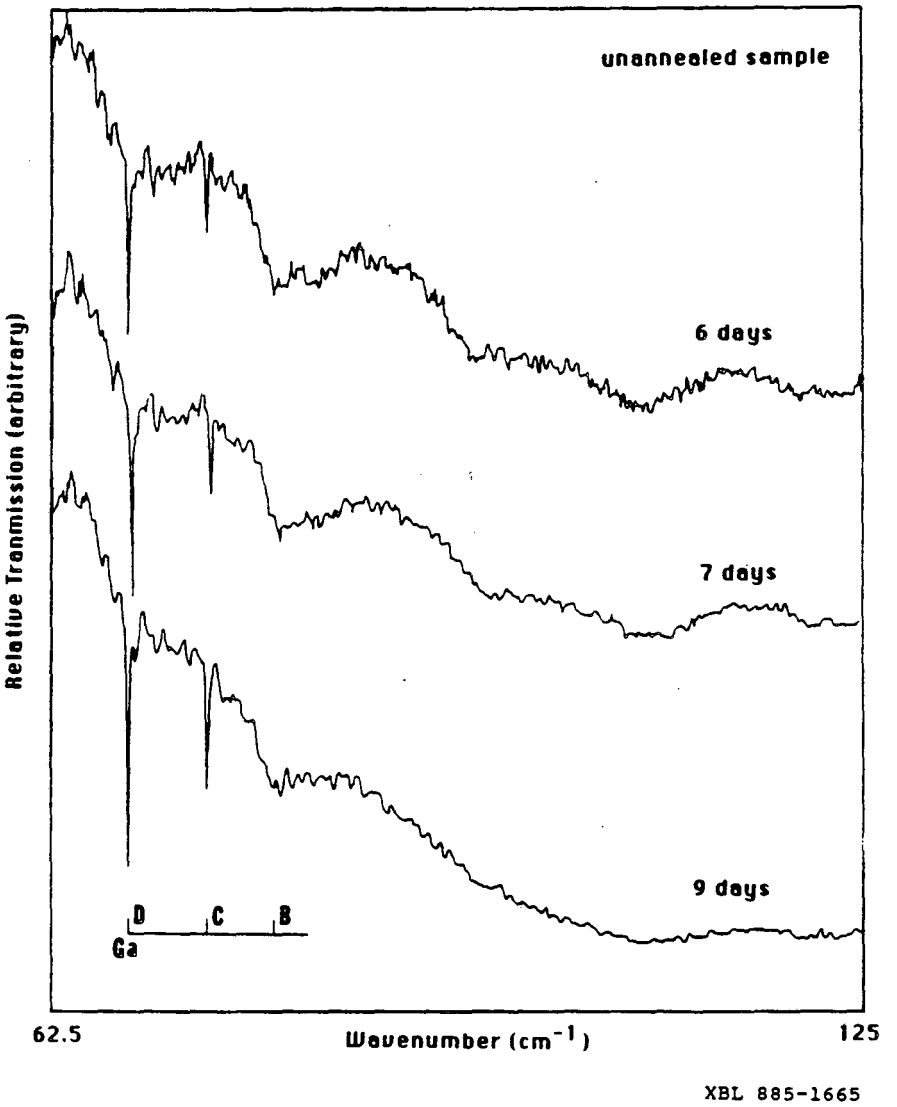

Fig. 3.8 IR absorption spectra of an unannealed NTD germanium sample measured as a function of time after neutron irradiation.

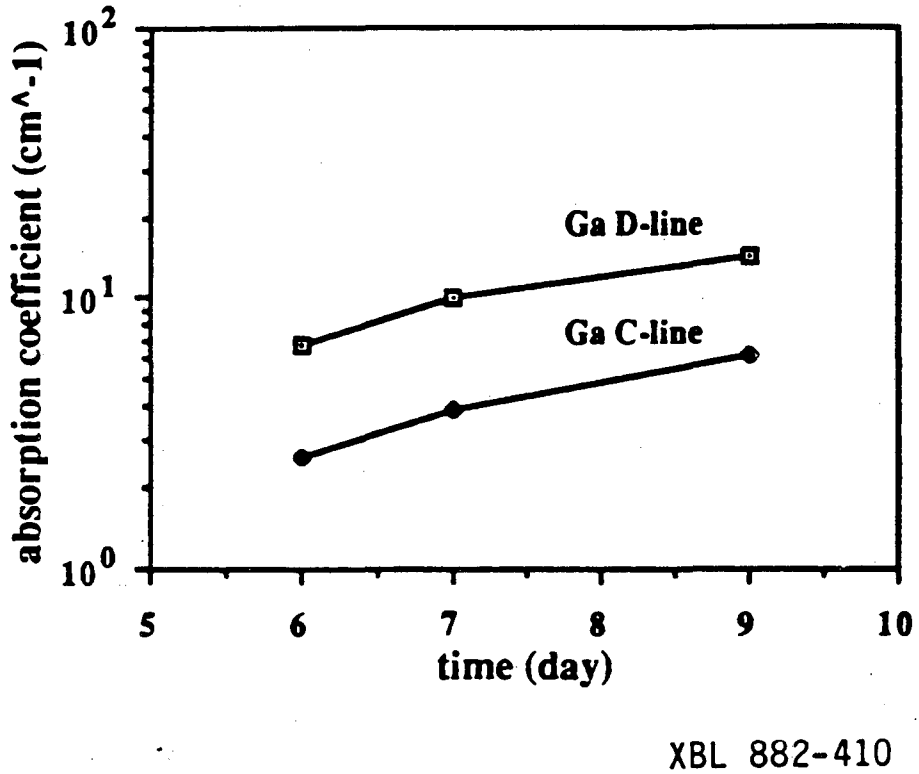

Fig. 3.9 Calculated α (from Fig. 3.8) vs. time after neutron irradiation of unannealed NTD germanium sample.

group V impurities, including arsenic, form complexes with vacancies and lose their donor property. These complexes can have energy levels in the bandgap. As an example, divacancy-donor complexes, observed in γ irradiated n-type germanium by Mashovetz [44], are deep acceptors with ionization energies near E_V + 0.10 eV. If the complexes formed in NTD germanium are the same as the divacancy-donor complexes in γ irradiated germanium, they would not show up in the absorption spectrum because of their deep acceptor level properties.

From the above observations we can list several possible scenarios about the evolution of transmutation produced impurities:

i) transmutation produced gallium impurities do not recoil sufficiently during decay process to become displaced from the original host germanium lattice location, and therefore, are electrically active acceptors;

ii) transmutation produced gallium impurities recoil during the decay process but afterwards diffuse to substitutional positions where they become electrically active acceptors;

iii) transmutation produced gallium impurities recoil away from substitutional positions, but rapidly diffusing vacancies recombine with the interstitial gallium forming substitutional gallium acceptors;

iv) transmutation produced arsenic impurities recoil from substitutional positions thereby becoming electrically inactive;

v) transmutation produced arsenic impurities do (or do not) recoil during decay process but, unlike gallium impurities, form complexes with radiation defects thereby losing their donor properties.

Using an elastic collision model, we can calculate the maximum energy transferred between two particles colliding into each other (or in this case, one particle splitting into two). When a particle with mass m and energy E elastically collides with a particle with mass M at rest as shown in Fig. 3.10, the maximum energy transferred from the moving particle to the particle that was at rest is:

$$T_m = \frac{2E(E + 2mc^2)}{Mc^2} \tag{3.4}$$

where c is the speed of light (= 3×10^8 m/sec). With equation 3.5,

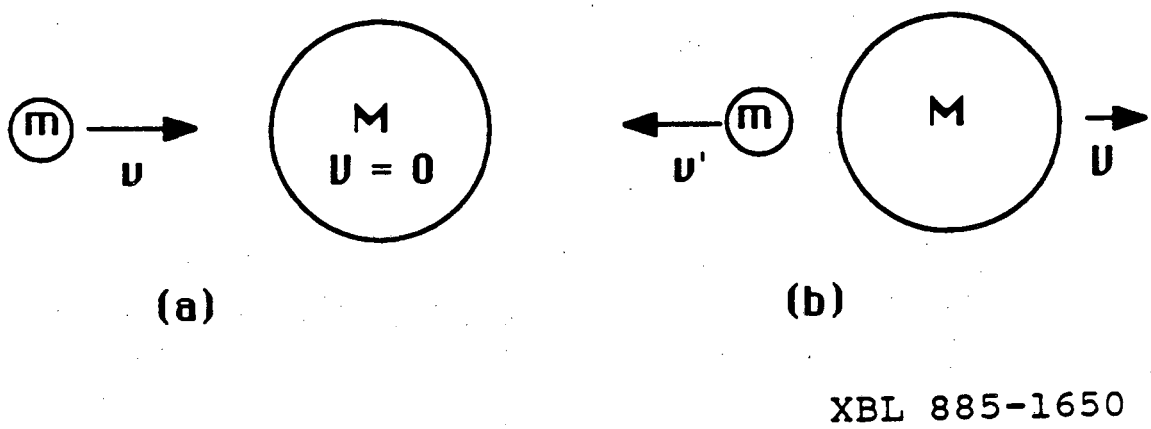

Fig. 3.10 Model for elastic collision of two moving particles.

we can calculate the recoil energies for the various decay reactions in NTD germanium. The displacement energy of germanium atom has been reported to be approximately 27.5 eV [78]. Any reaction with a recoil energy significantly greater than 27.5 eV can result in the dislocation of transmutated atom from its lattice position. Table 3.1 shows the result of calculations and the likelyhood for recoil of the transmutating isotopes.

From the results shown in Table 3.1, we conclude that gallium impurities do not recoil from their substitutional positions during the transmutation process (except for those atoms directly knocked out of substitutional position by fast neutrons) whereas arsenic and selenium impurities do recoil from their substitutional positions.

Table 3.1 Recoil of transmutating atoms in NTD germanium

reaction	emission	E_{max}(MeV)	T_{max}(eV)	probability of recoil
$Ge^{71} \rightarrow Ga^{71}$	γ	0.23	8.7	zero
$Ge^{75} \rightarrow As^{75}$	β^-	1.19	75	high
$Ge^{77} \rightarrow Se^{77}$	β^-	2.20	197	very high

This difference alone could explain the absence of absorption lines of arsenic in the unannealed sample.

However, the NTD germanium samples studied in this work were irradiated and kept at room temperature for some period of time before and during measurements. There is a possibility that the arsenic (and selenium) impurities in the interstitial positions diffuse to the substitutional positions at room temperature and become electrically active because they are highly mobile at room temperature as discussed in section 1.2.3.2. It has also been reported that interstitials in silicon can move and exchange positions with substitutional impurities at temperatures as low as 4.2 K [79]. The same analogy may also work for interstitials in gemanium, too. If this had happened to recoiled arsenic impurities in NTD germanium kept at room temperature, there would be absorption peaks of arsenic in the absorption spectrum of an unannealed NTD germanium sample. But the absorption spectrum of unannealed sample clearly shows that arsenic impurities are not

electrically active meaning that arsenic impurities formed complexes with radiation defects.

3.2.3 Absorption Spectra of Phosphorus-Doped, NTD Germanium

To verify if group V impurities in neutron irradiated germanium become electrically inactive, we did an infrared absorption study of neutron-irradiated, n-type germanium.

Slices were cut from a phosphorus-doped germanium single crystal which was grown under nitrogen atmosphere. Crystals grown under a hydrogen atmosphere were deliberately not chosen because it is well known that hydrogen forms a wide variety of complexes with impurities [80,81]. The phosphorus concentration was ~ 6 x 10^{13} cm^{-3} measured by Hall effect at 77 K. The sample was sliced into several 1 mm thickness wafers. An absorption spectrum was recorded for a sample before neutron irradiation to check the absorption lines from phosphorus. Figure 3.11(a) is the absorption spectrum of the phosphorus-doped germanium sample before neutron irradiation. The absorption peaks of phosphorus are clearly visible. The spectrum was taken under bandedge light illumination in order to be able to observe majority and minority dopants simultaneously. The absorption peaks from the compensating (minority) aluminum acceptors and other unknown residual acceptors are also visible.

Several wafers were irradiated with neutrons at Berkeley Research Reactor to introduce radiation defects along with transmutation gallium, arsenic, and selenium. The neutron fluence was again 2 x

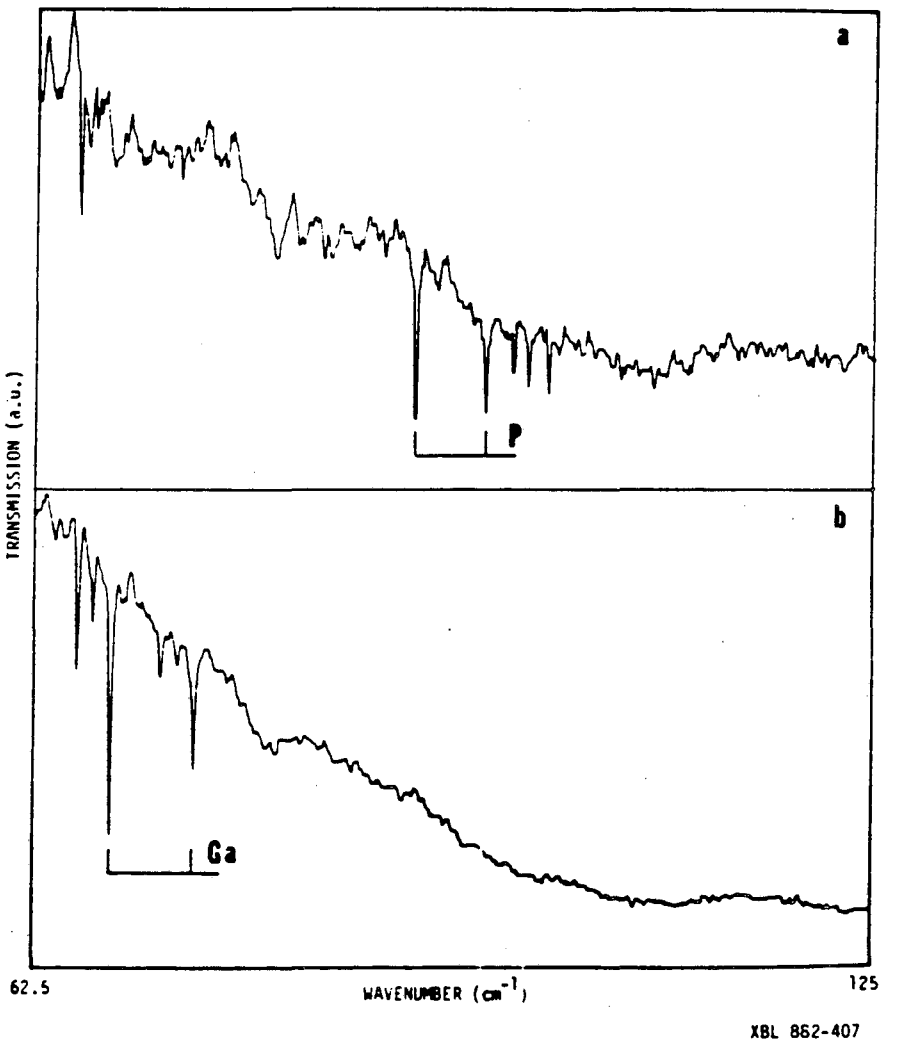

Fig. 3.11 IR absorption spectrum of phosphorus-doped (a) and phosphorus-doped, neutron-irradiated (b) germanium sample.

10^{15} cm^{-2} and the ratio of thermal to fast neutron was 4. After the neutron irradiation, the sample was checked by Hall effect and IR absorption measurements for different annealing conditions.

After neutron irradiation, the phosphorus absorption peaks are absent while those of gallium appear [Fig. 3.11(b)]. We can also see that the aluminum absorption peaks are not affected by neutron irradiation. This means that the residual phosphorus as well as the transmutation produced arsenic donors form complexes with radiation defects and lose their donor property while acceptors do not.

The phosphorus and arsenic absorption peaks do not appear even after annealing at 350°C for 1 hr within the sensivity limit of our IR absorption setup (~ 10^{12} cm^{-3} for 1 mm thick sample). After annealing at 400°C the absorption peaks of group V donors begin to appear and only after annealing at 450°C they reach maximum intensity (Fig. 3.12). In Mashovetz's paper, the donor-divacancy complex in γ irradiated germanium dissociated after annealing at 80°C for phosphorus-related complex and at 120°C for arsenic-related one. It has been reported that the annealing temperature required to remove radiation damage in irradiated semiconductors is higher for heavier particle irradiation [52]. The annealing temperature of the group V donor-defects complexes in our study is also higher than that reported for γ irradiated germanium. We conclude that the complexes formed in NTD germanium may not be the same defects as observed by Mashovetz but the complexes between donor and larger cluster of vacancies.

It is still not clear if the complexes were formed between

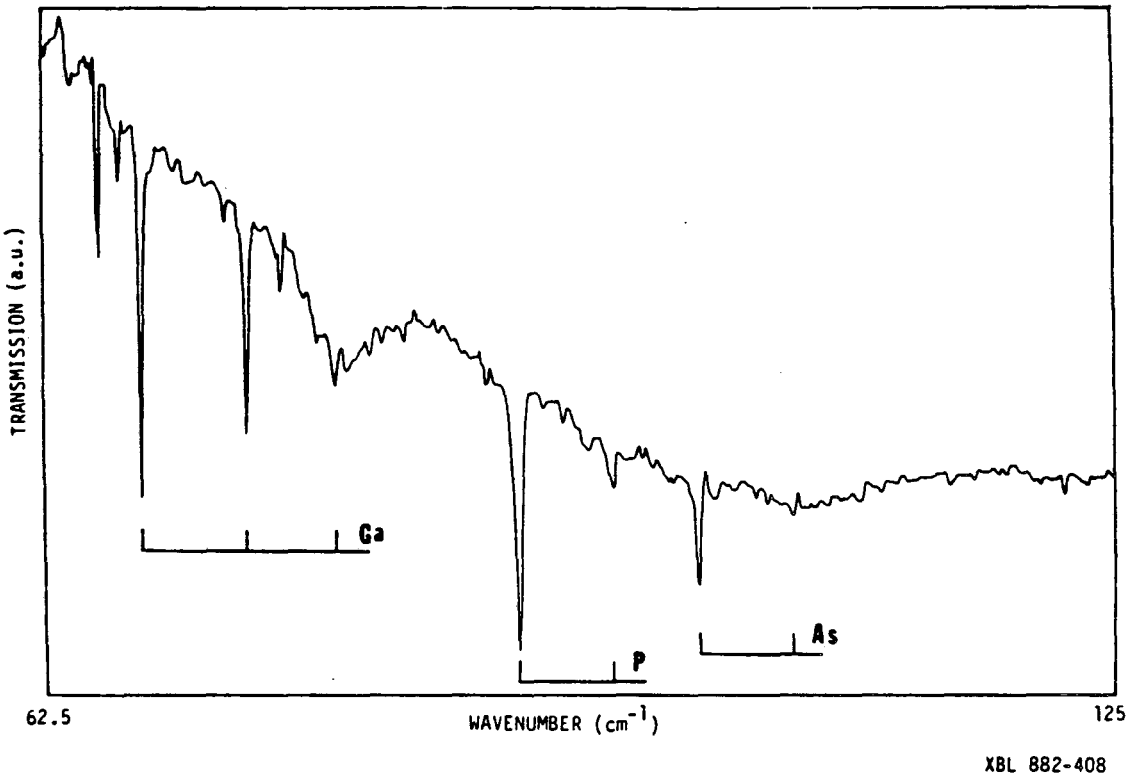

Fig. 3.12 The same sample as shown in Fig. 3.11(b) after annealing at 450°C for 1 hr.

vacancies and substitutional or interstitial donors. From the disappearance of the absorption peaks of phosphorus after neutron irradiation, we can draw several conclusions. It is not possible that all the phosphorus atoms in substitutional positions are knocked out into the interstitial positions by fast neutrons. A small fraction might have been knocked out, but this fraction must be very low considering the number of fast neutrons (~ 5 x 10^{14} cm^{-2}). However, the absorption spectrum of neutron irradiated and unannealed sample [Fig. 3.12(b)] shows no absorption peaks of phosphorus as well as those of arsenic (i.e., < ~ 5 x 10^{11} cm^{-3}). Therefore we

conclude that donor-vacancy complexes are formed by the diffusion of vacancy to the substitutional donor atom. However, we are not sure if the transmutation produced arsenic donors are in the interstitial position or if they diffuse into the substitutional position by the time they form the donor-vacancy complexes. The possibililty of complex formation between vacancies and interstitial donor atoms cannot be ruled out.

From our results, however, we could not verify whether the complex was really a donor-divacancy or not. The details of the radiation defects can be further investigated by DLTS (section 3.3) or other sophisticated methods.

3.3 Deep Level Transient Spectroscopy

The DLTS technique was applied in the investigation of radiation-induced deep level defects in NTD germanium. The advantages of the DLTS technique are that defect levels can be studied over a wide energy range in the gap and that the relative concentration of the defect levels can be determined. There are many publications reporting radiation-induced deep levels in germanium [21,46,82 ~ 85]. Most of the reported work concentrates on revealing the deep-level defects in as-irradiated germanium samples. This has improved the understanding of the nature of the radiation defects in germanium. In this thesis work, we concentrate on the deep level defects which exist after high temperature annealing (> 200°C).

DLTS samples are prepared by neutron irradiation followed by

annealing at different temperatures. The measurements were done on these samples to check the presence and the removal of deep level defects in NTD germanium. Our measurement setup is capable of reading temperatures between 20 ~ 400 K. We found that temperature ranges between 20 K and 200 K is sufficient to cover all the deep levels in NTD germanium.

3.3.1 Deep Level Defects in NTD Germanium (P-Type)

The same samples used in Hall effect measurement were also used for DLTS measurements. Ohmic contacts were prepared by alloying a small amount of indium on any of the corners (or the contacts used for Hall effect measurement were used again). A p-n diode was made by diffusing lithium (5 min, 250°C) on the other side of the sample.

Germanium samples annealed at 300°C and 500°C after neutron irradiation are investigated. The sample annealed at 500°C is supposed to have recovered from all the radiation defects while the sample annealed at 300°C has not.

A DLTS spectrum of a sample annealed at 300°C for 1 hr after neutron irradiation is shown in Fig. 3.13. Two DLTS peaks are observed in the temperature range 20 ~ 300 K. These peaks are due to hole traps with trap energies of 0.30 eV and 0.37 eV obtained from a plot of ln e/T^2 vs. 1000/T (Fig. 3.14). The hole trap at E_v + 0.30 eV is believed to be the same as the one reported at E_v + 0.31 eV peak by Fukuoka and Saito [82]. They observed this hole trap in 10 MeV electron irradiated germanium samples doped with indium and

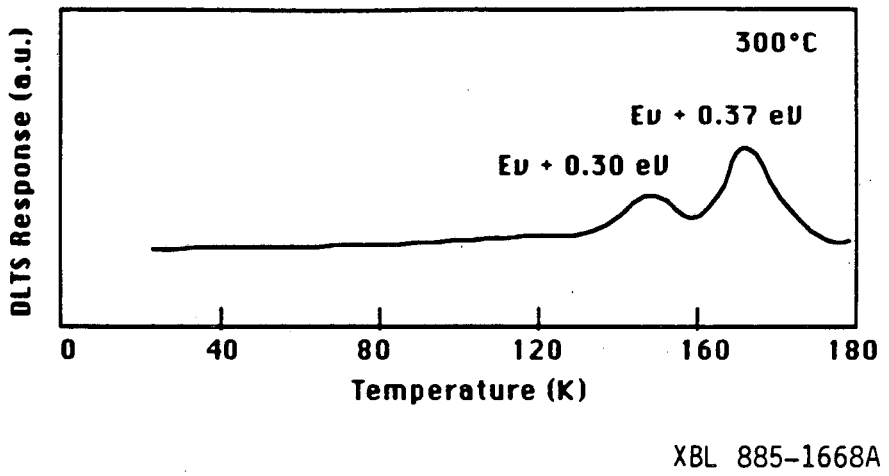

Fig. 3.13 DLTS spectrum of NTD germanium sample annealed at 300°C.

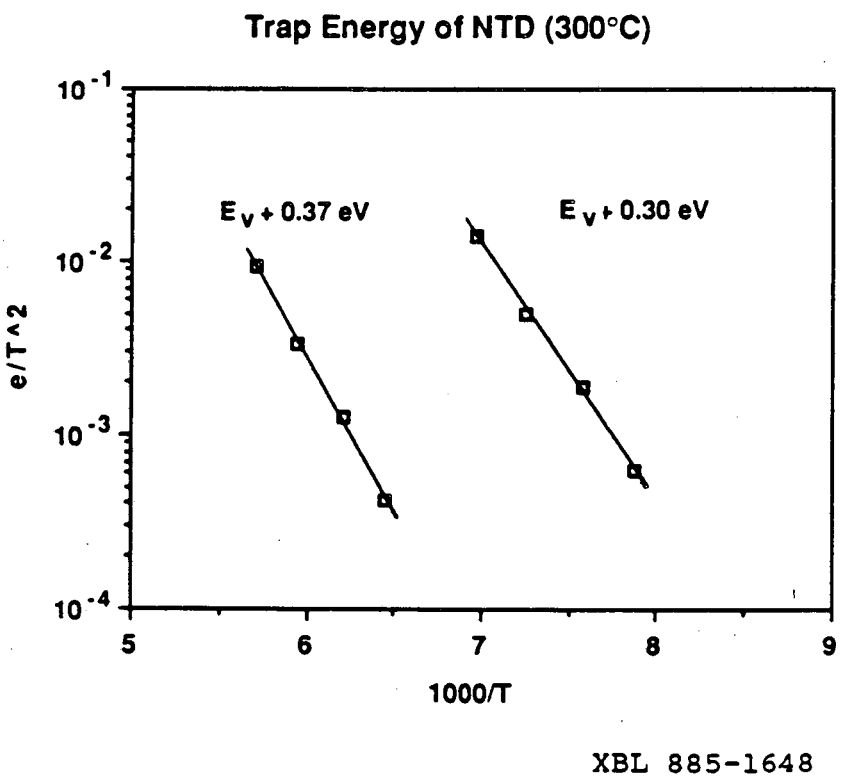

Fig. 3.14 Plot of ln e/T^2 vs. 1000/T of NTD germanium sample annealed at 300°C.

gallium. This trap was proposed as a native defect complex which does not contain an impurity atom as a component (i.e., a vacancy cluster). The hole trap at E_v + 0.37 eV was not observed by Fukuoka and Saito but was reported by Palaio, et al [21] in NTD germanium. The fact that the same trap was not observed in the work of Fukuoka and Saito may be due to the different kinds of irradiation (neutrons vs. electrons).

Figure 3.15 shows the DLTS spectrum of the sample annealed at 500°C. Two hole traps are observed. The trap energies are 0.22 eV and 0.30 eV as obtained from Fig. 3.16. The trap at E_v + 0.37 eV that was observed in the sample annealed at 300°C is absent in this spectrum. The trap at E_v + 0.22 eV is the same trap as reported in Palaio, et al's work and is also reported as the trap at E_v + 0.21 eV in Fukuoka and Saito's work [82]. Although there is a possibility of contamination by the rapidly diffusing and highly soluble copper impurities at high temperature (500°C) we rule out this possibility because we cannot find a peak corresponding to the first ionization of copper (E_v + 0.04 eV).

In both spectra in Figs. 3.13 and 3.15, the hole trap at E_v + 0.24 eV that was observed in indium doped germanium and also in some n-type germanium (antimony and arsenic doped germanium) [83,84] is not observed.

The concentration of all the hole traps measured using equation 2.43 were very small (~ 10^{11} cm^{-3}) and the absolute comparison of concentration between different measurements were difficult. The comparison was only made by comparing the relative intensities in the

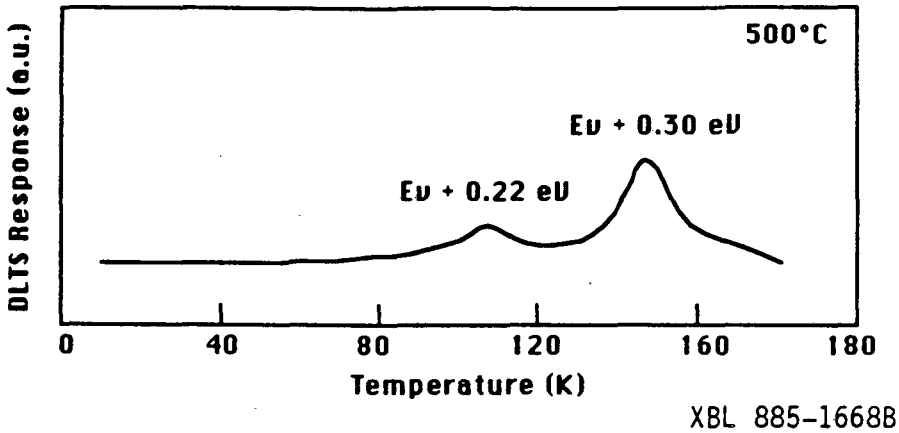

Fig. 3.15 DLTS spectrum of NTD germanium sample annealed at 500°C.

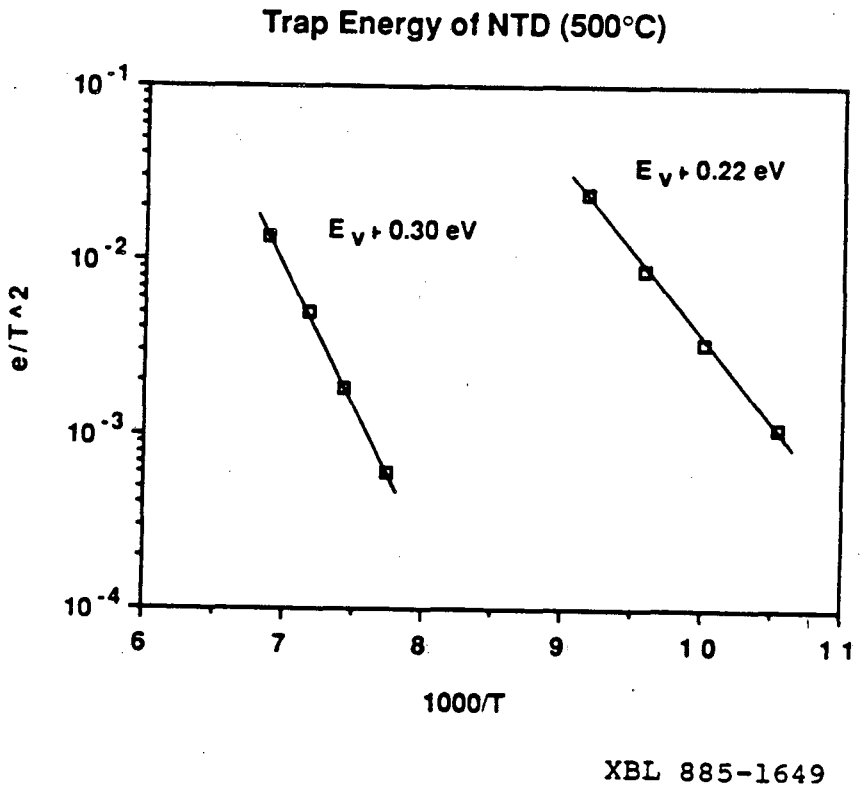

Fig. 3.16 Plot of ln e/T^2 vs. 1000/T of NTD germanium sample annealed at 500°C.

spectra.

The hole trap at E_v + 0.37 eV that is observed in the sample annealed at 300°C is believed to dissociate by annealing at 500°C, possibly increasing the concentration of the trap at E_v + 0.21 eV while the concentration of the trap at E_v + 0.31 eV remains practically unchanged. The defect associated with the level at E_v + 0.37 eV is thus believed to be a relatively simple complex which dissociates by annealing at 500°C. It is, however, not clear what the nature of E_v + 0.22 eV level is and why it was absent in the sample annealed at 300°C but appears after annealing at 500°C.

It should be noticed that, although the concentration is very low (~ 10^{11} cm^{-3}), two hole traps are present even after annealing at temperature as high as 500°C. From the fact that these two traps (E_v + 0.21 eV and E_v + 0.31 eV) are present in the sample annealed at 500°C, it is concluded that they are large and very stable complexes.

3.3.2 N-Type germanium

Electron traps in NTD germanium usually cannot be observed because the NTD process produces p-type germanium. To be able to observe the minority traps in DLTS measurement, one must inject electrons into the sample by forward bias pulsing. We have not attempted this technique, but we prepared n-type samples with concentrations high enough that the NTD process did not convert the type of the sample, so that we could study electron traps in NTD germanium.

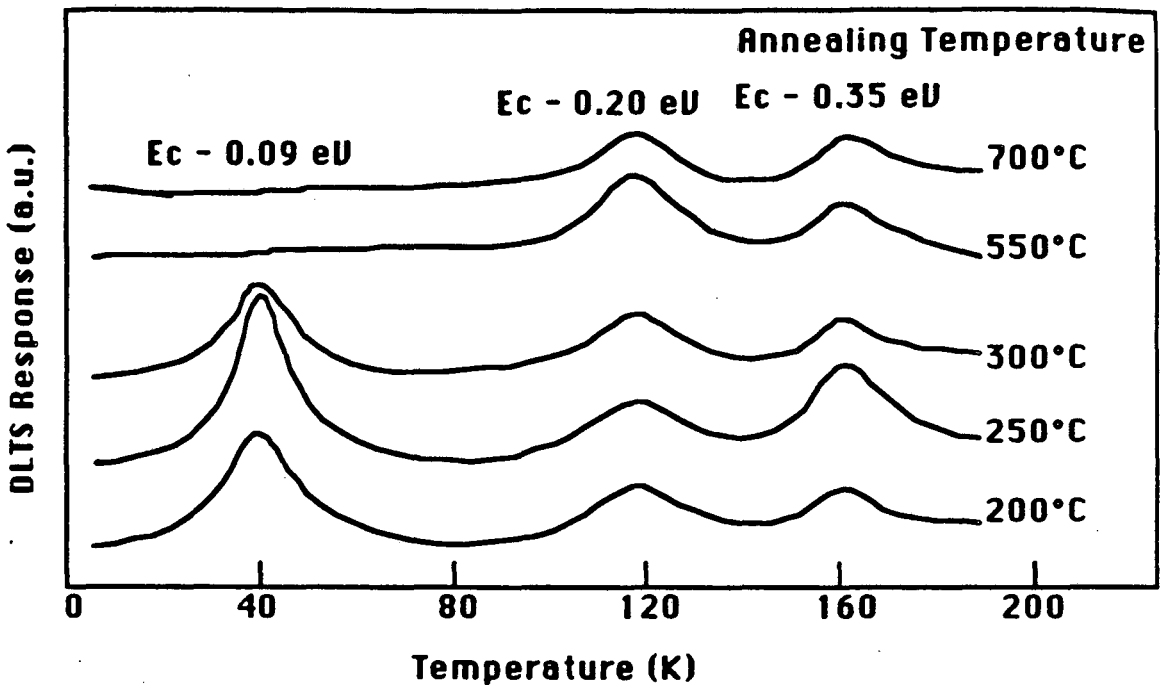

XBL 885-1667

Fig. 3.17 DLTS spectra of n-type, NTD germanium samples annealed at different temperatures.

Again, a phosphorus-doped, nitrogen atmosphere grown germanium sample was used. We chose a slice with a phosphorus concentration of 5×10^{13} cm^{-3}. We irradiated the sample with 2×10^{15} cm^{-2} neutrons at the University of Missouri Research Reactor facility. The neutron dose was chosen such that the resultant net-doping concentration remained slightly n-type. The net doping concentration measured with Hall effect at 77 K after NTD and annealing at different temperatures ranged from 6×10^{12} cm^{-3} to 2×10^{13} cm^{-3} n-type.

DLTS samples were prepared by implanting phosphorus to form an

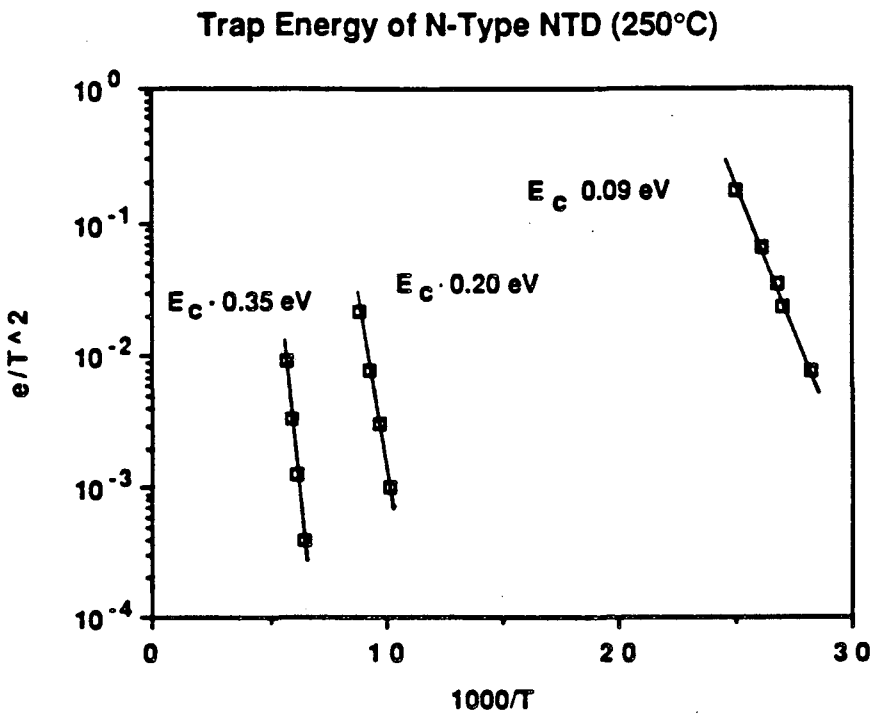

XBL 885-1647

Fig. 3.18(a) Plot of ln e/T^2 vs. 1000/T of n-type, NTD germanium sample annealed at 250°C

ohmic contact and by implanting boron on the other side to form a blocking contact. To assure good electrical and mechanical contact during the measurement, both sides of the samples were sputtered with 5000 Å of gold.

DLTS spectra for samples annealed at different temperatures are shown in Fig. 3.17. Three peaks are observed in n-type NTD germanium. These are electron trap energy levels at E_c - 0.09 eV, E_c - 0.20 eV, and E_c - 0.35 eV as obtained from Fig. 3.18. The traps at E_c - 0.09 eV and E_c - 0.35 eV were also observed by Nagesh and Farmer [48]. They proposed the E_c - 0.09 eV level to be

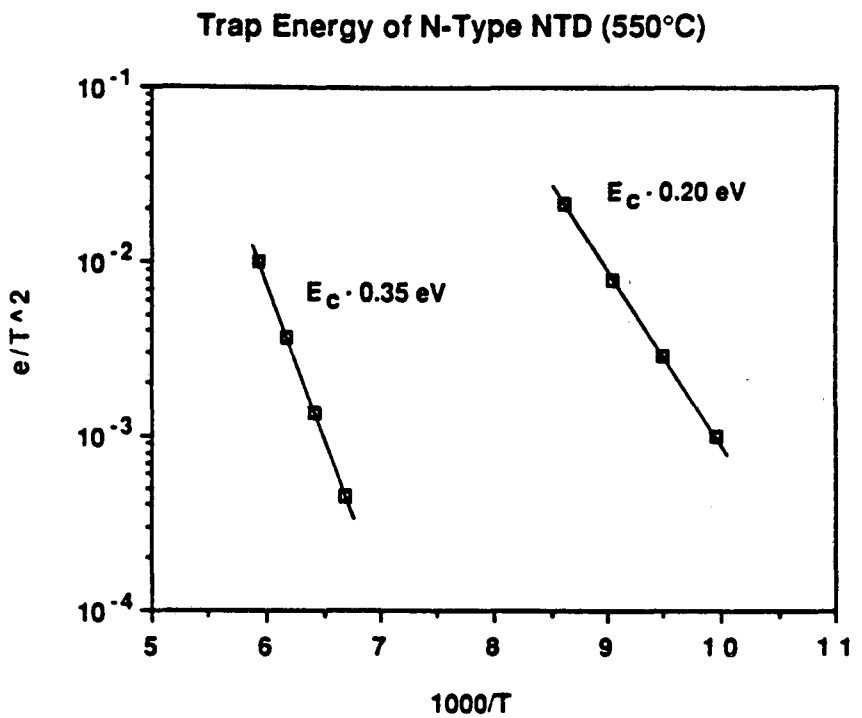

XBL 885-1646

Fig. 3.18(b) Plot of ln e/T^2 vs. 1000/T of n-type, NTD germanium sample annealed at 550°C.

a planar four-vacancy and E_c - 0.35 eV level to be a donor-vacancy pair. The traps at E_c - 0.17 eV (divacancy) and at E_c - 0.27 eV (vacancy-oxygen pair) are absent in our spectra. Either these traps were annealed out at high temperature (divacancy and/or vacancy-oxygen pair) or the sample did not contain enough oxygen (vacancy-oxygen pair). The E_c - 0.20 eV level which was not observed by Nagesh and Farmer was observed by Fukuoka and Saito [85] in both antimony- and arsenic-doped germanium after electron irradiation. The formation of the level was assumed not to be correlated with impurity atoms but with vacancies or interstitial atoms. It is not clear why the same

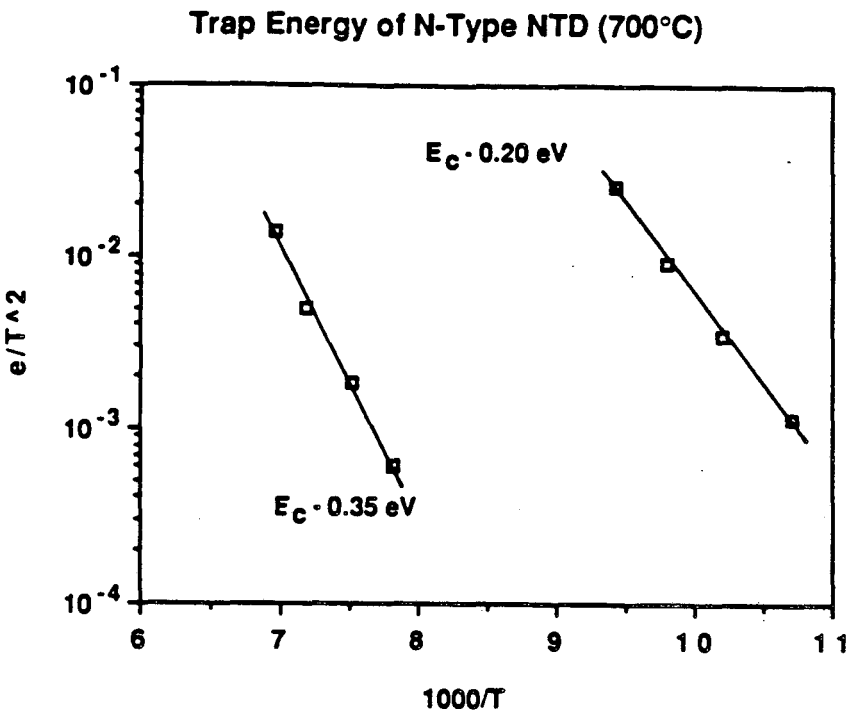

XBL 885-1645

Fig. 3.18(c) Plot of ln $e\mu T^2$ vs. 1000/T of n-type, NTD germanium sample annealed at 700°C.

trap was not observed in Nagesh and Farmer's work (phosphorus- and antimony-doped germanium irradiated either with γ or neutron, [46]).

As the annealing temperature is increased from 200°C to 700°C, the peak intensity of E_c - 0.09 eV and E_c - 0.35 eV level decreases relative to the peak intensity of E_c - 0.20 eV level. From this annealing behavior, it is preliminarily concluded that the E_c - 0.20 eV level is more stable than either the E_c - 0.09 eV or the E_c - 0.35 eV level. It is remarkable that although the concentration is very low (~ 10^{11} cm^{-3}) all these levels are still present in a sample annealed at 700°C for 1 hr.

3.4 Direct Observation of Neutron-Induced Defects in Germanium

Using high resolution transmission electron microscopy, neutron-induced defects in germanium were studied. As only a very small area of the sample can be studied by the electron microscopy, the density of radiation defects must be very high to be observed directly. Fig. 3.19 shows micrograph of two samples neutron irradiated (A, 2×10^{15} cm^{-2} and C, 3×10^{18} cm^{-2}) and annealed at 400°C for 4 hr (B and D, respectively). In the sample irradiated with low dose of neutrons (A and B), we could not observe any disordered region in the TEM sample. This is because of the low density of disordered region (radiation defects) of the sample. In the sample irradiated with 3×10^{18} neutrons/cm^2, however, small disordered regions are observed (dark circular areas). After annealing, no disordered region could be found any more. As discussed earlier, those vacancy clusters or interstitials dissociate by annealing at 400°C.

High resolution micrograph of NTD germanium sample irradiated with 3×10^{18} neutrons/cm^{-2} is shown in Fig. 3.20. A disordered region is clearly shown. The region consists of many interstitials and vacancies and the two-dimensional size of the disordered region is estimated to be about 10 x 10 atomic spacings. The extent of disordered region would be of the order of ~ 10^3 atomic spacings in three-dimension, in accordance with the expectations with an estimated value for fast neutron damage [36]. Also a dislocation produced by the radiation is clearly visible in the figure. We could not,

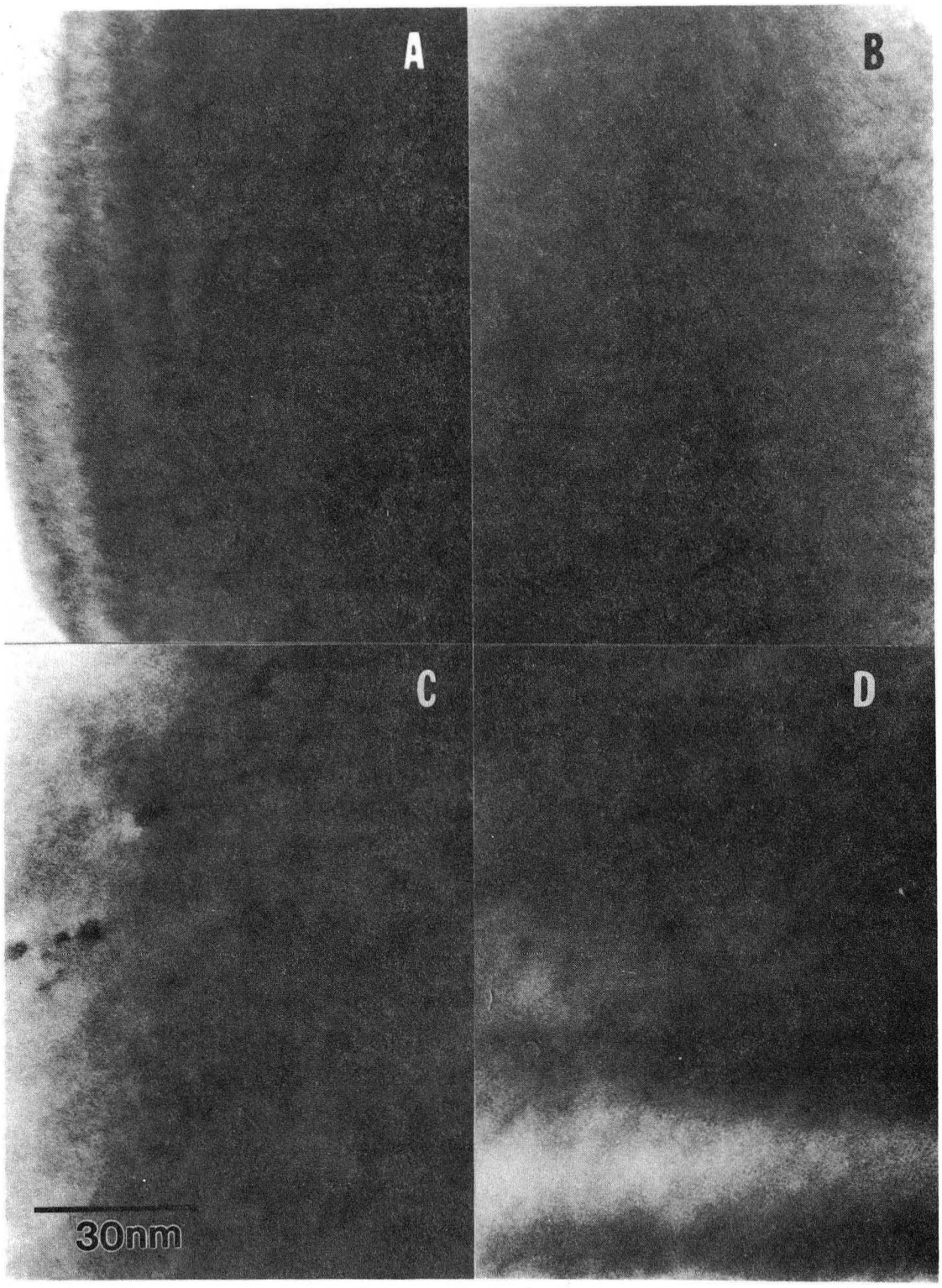

XBB 885-5128

Fig. 3.19 Transmission electron micrographs of neutron irradiated (A, 2×10^{15} cm^{-2} and C, 3×10^{18} cm^{-2}) and annealed (B and D, respectively) germanium samples. Annealing was done at 400°C for 4 hrs.

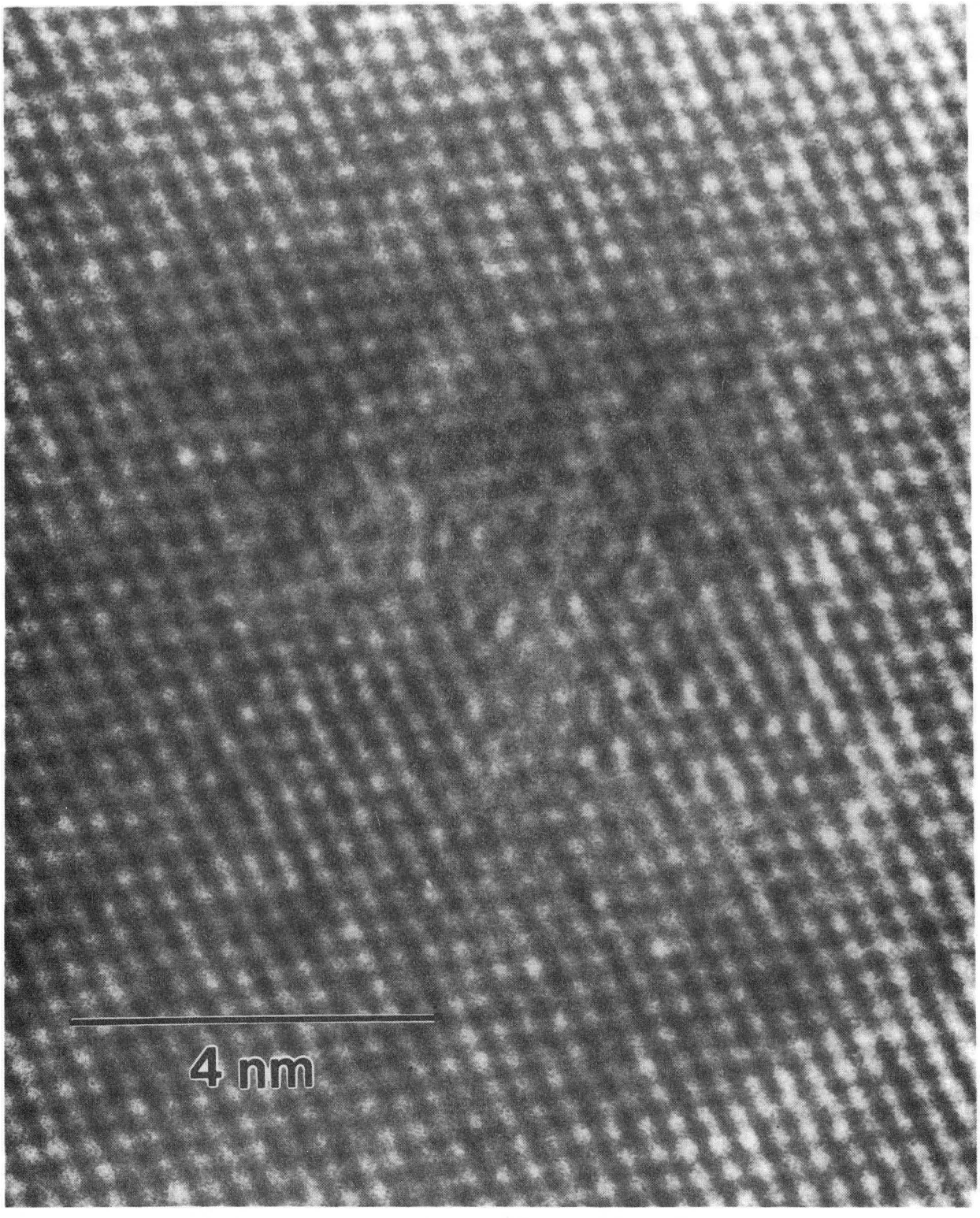

XBB 885-5127

Fig. 3.20 High resolution micrograph of germanium sample irradiated with 3×10^{18} neutrons/cm^2.

however, calculate the number density of the disordered regions in the sample.

4. Summary and Conclusions

The compensation ratio of NTD germanium irradiated at Berkeley Research Reactor has been experimentally determined to be 0.306. This value is very close to the one reported in reference 26. A direct determination of compensation ratio could be possible with well calibrated IR spectroscopy with bandedge light illumination is used.

By measuring the linear absorption coefficient α of shallow impurities in germanium of known standard samples, a standard calibration plot was obtained. The photoionization cross section of arsenic donor in germanium has been determined to be 6×10^{-13} cm^2 from the slope of the plot. Due to the lack of enough data, we could not obtain the photoionization cross section of other shallow impurities.

The presence of neutron-induced defects in NTD germanium were clearly shown by measuring the net-carrier concentration of unannealed sample as a function of time after neutron irradiation. Annealing at or above 400°C for 1 hr removed most of radiation defects in NTD germanium.

It was directly shown by IR absorption spectroscopy with bandedge light illumination that transmutation produced gallium acceptors are electrically active without annealing while arsenic impurities are not. From further evidence, we concluded that group V donors in

irradiated germanium readily form complexes with vacancies. The complexes were formed between substitutional donors and vacancies. But the possibility of complex formation between interstitial donors and vacancies was not ruled out. The detailed nature of these complexes has not been identified.

By DLTS measurements, it was found that two hole traps with energy levels at $E_v + 0.21$ eV and at $E_v + 0.31$ eV existed even after annealing at 500°C for 1 hr in p-type NTD germanium. In n-type NTD germanium, three electron traps with energy levels at $E_c - 0.09$ eV, at $E_c - 0.20$ eV, and at $E_c - 0.35$ eV were present after annealing at 700°C for 1 hr. The concentration of all these traps, however, was very low ($\sim 10^{11}$ cm^{-3}).

The defect region in NTD germanium has been shown by high resolution transmission electron microscopy. The size of disordered region is of the order of 10^3 atomic spacings. After annealing at 400°C for 4 hr, the disordered region has disappeared.

Part II: Development of Far-Infrared Detectors using NTD germanium

The Infrared Astronomical Satellite (IRAS) provided the first full survey of the infrared sky. The large number of new discoveries, including thousands of hitherto unknown galaxies, infrared-emitting dust clouds, starbirths, etc, has led to an intense research and development effort for future missions. The Space Infrared Telescope Facility (SIRTF), a cooled, pointed space telescope, is currently being planned by NASA.

In addition to satellite-based observations, astronomers also employ high altitude ground-based and airborne infrared instruments.

The key elements in all such infrared observing instruments are the infrared detectors. Therefore, there exists a continuous need for better infrared detectors from the astrophysics community. In this part we discuss the application of NTD germanium in the development of far-infrared detectors.

5. Introduction to Infrared Detectors

Infrared detectors can be grouped into two classes by the physical mechanism involved in the detection process. In one group, called thermal detectors or bolometers, the heating effect of the incident radiation causes a change in some electrical property of the detector. In the other group, called photon or quantum detectors, there is a direct interaction between the incident photons and the electrons of the detector material. The response of a thermal

detector is proportional to the energy absorbed whereas that of a photon detector is proportional to the number of photons absorbed.

The time constant of a thermal detector is usually a few milliseconds or larger, so they are rarely used in applications that require high data rates. One obvious advantage of thermal detectors is that they work for any wavelength as long as the photons are absorbed.

The response time of photon detectors can be made very short, usually in the microsecond range, because of the direct interaction between the incident photons and the electrons of the detector material. Most photon detectors have a detectivity that is one or two orders of magnitude greater than that of thermal detectors. This higher detectivity is obtained by cooling to cryogenic temperatures. The spectral response of photon detectors, unlike that of thermal detectors, is narrow and varies with wavelength.

6. NTD Germanium Bolometers

Thermal detectors that change their electrical resistance when heated by incident radiation are called bolometers, i.e., the change in conductivity due to a temperature change of detector is used to create a signal. When radiation is absorbed by the bolometer, the temperature is increased and the temperature change in turn changes the resistivity of the detector.

In 1800 Herschel developed a mercury thermometer which registered an increased temperature when illuminated by infrared radiation [86].

The term "bolometer" was firstly used by Langely [87] in 1880. He made a bolometer which consisted of a resistor made of fine platinum wire. In 1961, Low [88] developed the first liquid helium cooled semiconducting bolometer using highly doped, highly compensated germanium. Lowering the operating temperature lowers the heat capacity of the device, thus increasing the sensitivity. The spectral response of such a device extends beyond 1000 μm. Superconducting bolometers such as SNS tunnel junction bolometer [89] and superconducting transition edge bolometer [90] have also been developed. However, the most popular bolometers are those made of semiconductor because of; i) commercial availability, ii) the straightforward electronics for operation, iii) ability to operate in high magnetic fields, and iv) the exponential dependence of resistivity on temperature. Recently, Lange et al [4] reported an improved technique for fabricating NTD germanium composite bolometers which consist of a small thermometer mounted on a larger absorbing antenna (bismuth on sapphire). The antenna material has a lower heat capacity than the semiconductor, and warms to a higher temperature when irradiated. This induces a larger signal from the thermometer. In their paper, implanted, metallized contacts were used to reduce 1/f noise.

The requirements for cryogenic bolometer materials are uniform doping and high compensation. Also, the doping process should be reproducible so that detectors of known behavior can consistently be produced. NTD germanium satifies these requirements for bolometer material and nowadays, many NTD germanium bolometers are being used

for various applications.

6.1 Basic Operation Mechanism

In the characterization of detectors, we usually compare the responsivity and the noise equivalent power (NEP). The responsivity is usually expressed as the signal output (current or voltage) per unit incident radiation power. A more important figure of merit is the NEP. NEP is the ultimate sensivity of a detector and is defined as the incident power required to obtain a signal-to-noise ratio of one per unit detection bandwidth ($W/\sqrt{Hz}$). For the detection of weak infrared sources, it is required that detectors have very low NEP's.

The basic thermal circuit of a bolometer is shown in Fig. 6.1. The heat flow from the bolometer to the heat sink is given by:

$$\eta P = H(d\theta/dt) + G\theta \tag{6.1}$$

where η = fraction of power absorbed (quantum efficiency), P = incident radiation power, H = thermal mass of the detector, θ = temperature increase above the sink temperature T, and G = thermal conductance of the link. If the radiation flux consists of a continuous background component P_0 and a sinusoidally changing signal component P_ω, one can write:

$$P = P_0 + P_\omega \exp(j\omega t) \tag{6.2}$$

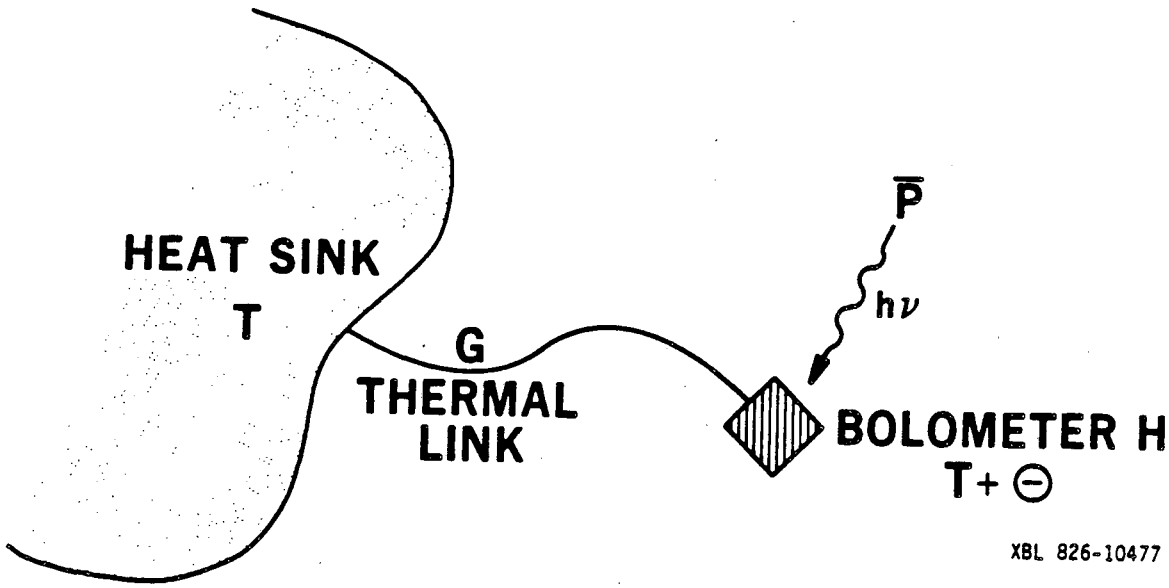

Fig. 6.1 Basic thermal circuit of a bolometer.

and we obtain:

$$\Theta_\omega = \eta P_\omega (G^2 + \omega^2 H^2)^{-\frac{1}{2}} \tag{6.3}$$

with the phase angle ρ between P_ω and Θ_ω:

$$\rho = \tan^{-1}(\omega H/G) \tag{6.4}$$

The characteristic response time constant τ can be defined by:

$$\tau = H/G \tag{6.5}$$

Typical values of τ fall between milliseconds and seconds, illustrating the slow response, which is one distinct disadvantage of thermal detectors.

The temperature coefficient α for the resistance R_b of a bolometer is commonly defined by:

$$\alpha = \frac{1}{R_b}\left(\frac{dR_b}{dT}\right) \tag{6.6}$$

with R_b = resistance and T = temperature. The voltage change V_s across the bolometer element can be written as:

$$V_s = I\Delta R_b = I\alpha R_b \theta_\omega \tag{6.7}$$

with I = current passing through the bolometer. Using the expression for θ_ω we find:

$$V_s = \eta P_\omega (G^2 + \omega^2 H^2)^{-\frac{1}{2}} I\alpha R_b \tag{6.8}$$

or in the form of a voltage responsivity S (V/W):

$$S = \frac{V_s}{P_\omega} = \eta I\alpha R_b (G^2 + \omega^2 H^2)^{-\frac{1}{2}} \tag{6.9}$$

This equation shows that to maximumize S, one wants to choose high

values of α, R_b, I and η. The bolometer resistance R_b can be made very large, but with the best amplifiers using cooled junction field effect transistors, one obtains the best results with bolometers and load resistors of the order of 10^6 to $10^8 \Omega$ [91].

The NEP is expressed as the rms sum of several independent terms:

$$(NEP)^2 = \frac{4kTR}{S} + 4kT^2G + 2kT_B\varepsilon P_B + (\text{other terms}) \qquad (6.10)$$

where T_B is the background temperature, ε is the emissivity, and P_B is the background power (blackbody radiation) from a Rayleigh-Jeans source at temperature T_B. The first term represents the square of the Johnson noise voltage across the bolometer of resistance R at temperature T with the voltage responsivity S. The second term is the thermal conductance noise due to random phonon fluctuation through the thermal link between the heat sink and bolometer. The third term arises from random fluctuations in the background radiation of the detector at temperature T_B. A bolometer is called "ideal" when the third term dominates the NEP. In practice, however, the first and the second term cannot be made smaller than the third or other terms.

To obtain a low NEP, bolometers are made very small to reduce the heat capacity and are operated at very low temperatures (< 4.2 K).

6.2 Detector Fabrication

In the cryogenic temperature range, the conduction mechanism of

highly doped, highly compensated semiconductors is impurity "hopping" conduction. The electrical conduction occurs via thermally activated net transfer of carriers from filled to neighboring empty sites. Therefore we can expect that small changes in the inter-impurity distances (i.e., doping concentrations) and the compensation will lead to large fluctuations in the resistance of detector material yielding a large difference in the detector performance. Changes within a slice of melt doped semiconductor crystal can be too large to yield more than a few suitable bolometer elements. This problem is easily solved by using NTD germanium as a bolometer material. As already discussed in Part I, NTD germanium has very uniformly distributed dopants, the doping concentration is reproducible, and is compensated with a fixed compensation ratio of 0.32.

We prepared several slices of ultra-pure germanium single crystal grown at Lawrence Berkeley Laboratory. The concentration of residual impurities was about 10^{10} cm^{-3}. Even if there are fluctuations in the starting material, the doping concentration from NTD is much higher than the residual impurity concentration and the resultant doping is very uniform throughout the sample. The slices were irradiated with neutrons at the Missouri Research Reactor Facility [92] with various doses of neutrons. As already explained, the resistance of the detector material should lie between 10^6 and $10^8 \Omega$ at the operating temperature to yield a best match with the electronic systems. By using different dose of neutrons we get materials with different resistivities, enabling us to prepare bolometer materials for different operating conditions. After neutron

irradiation, the slices were stored until all the radioactive reactions were complete and then annealed at 400°C for 6 hr in flowing argon gas. To prevent the diffusion of copper into the sample during the annealing stage, the samples were soaked in KCN solution for 10 min and cleaned with distilled water just before annealing. It has been reported that soaking germanium samples in KCN solution before annealing reduces surface contamination with copper [93].

To prepare bolometers, a slice with desired thickness is cut from the annealed sample. The slice is lapped, polish etched in HNO_3:HF (3:1) solution and soaked in 1% HF solution to remove the oxide. The slice is then implanted with boron (1×10^{14} at 25 keV and 2×10^{14} at 50 keV, step implant) on both sides to develope a degenerately (metallically) doped layer on the surface. This layer serves as a good ohmic contact. Then the surface was sputtered with 200 Å of palladium and 4000 Å of gold to facilitate mechanically strong electrical contacts to the final device.

Using either a wire saw or dicing saw, the processed slice is cut to the desired final size (usually a cube with 0.3 mm long edge is chosen for low heat capacity and easy handling). To remove the saw damage of the final sample, the cubes are lightly etched in HNO_3:HF (3:1) solution for 30 sec.

6.3 Resistivity Measurement

The first characterization of bolometer materials is the resistivity measurement at cryogenic temperatures. By knowing the

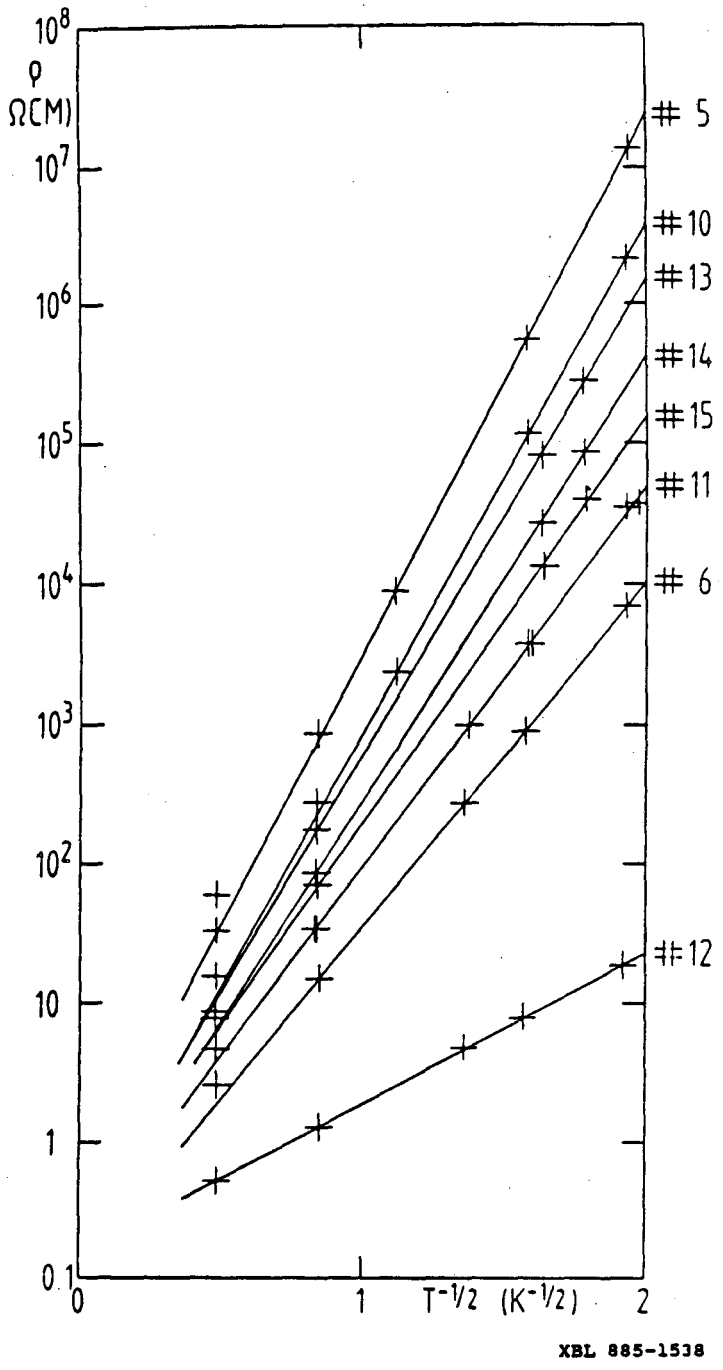

Fig. 6.2 Plot of ln ρ vs. $T^{-1/2}$ of NTD germanium samples.

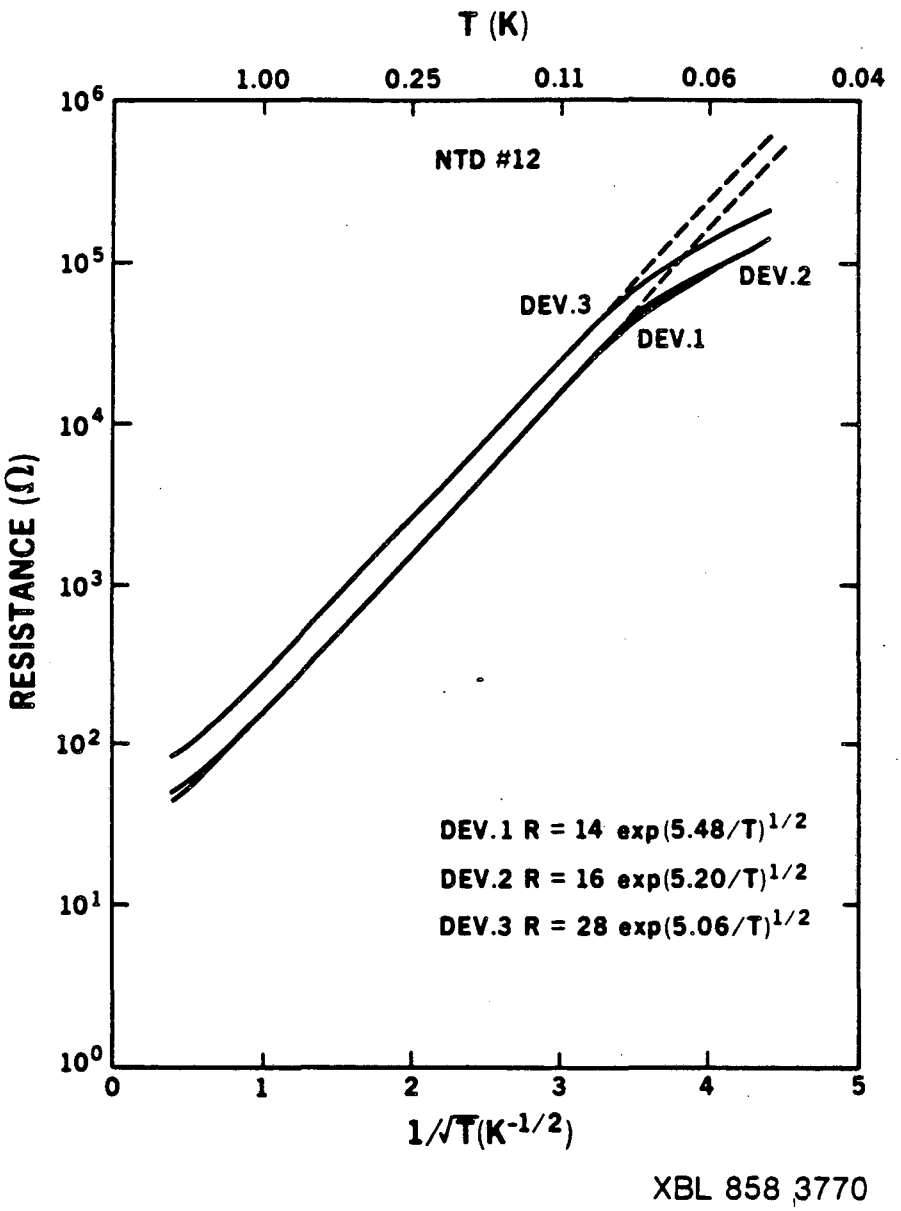

Fig. 6.3 Plot of ln ρ vs. $T^{-1/2}$ of NTD 12 sample.

resistivity of the various NTD materials at different temperatures, we can choose an optimum material for specific operating conditions. Resistivity measurements of bolometers are performed by our co-workers [94 - 96].

Figure 6.2 shows the temperature dependence of the resistivity of eight transmutation-doped germanium samples in the temperature range 4.2 K ~ 0.25 K. When plotting the logarithm of the resistivity as a function of inverse absolute temperature down to such low temperatures (Arrhenius plot, as done by Fritzsche and Cuevas [2]), one finds that the hopping regime deviates from a straight line [97]. A better fit to straight lines is obtained by plotting the logarithm of the resistivity as a function of the inverse square root of the absolute temperature. Such a dependance for hopping conduction has been also predicted by some theoretical models [98,99]. The result in Fig. 6.2 shows the relation:

$$\rho = \rho_0 \exp\left(\frac{\Delta}{T}\right)^{\frac{1}{2}} \tag{6.11}$$

where the constants ρ_0 and Δ are dependent on both the doping concentration and the degree of compensation. As we are using NTD germanium samples in this study, the compensation ratio is always 0.32. Resistance measurements of three samples made of NTD #12 at even lower temperatures (down to 50 mK) are shown in Fig. 6.3. Device 3 has a somewhat higher resistance than devices 1 and 2 because of a difference in the sample geometry. However, the slope of the straight

Table 6.1 Notations and Doping Concentrations of NTD Germanium

NTD	n dose (cm^{-2})	N_{Ga} (cm^{-3})	N_{As} (cm^{-3})	N_{Se} (cm^{-3})	$N_A - N_D$ (cm^{-3})
1	7.50×10^{16}	2.2×10^{15}	6.3×10^{14}	4.1×10^{13}	1.5×10^{15}
2	1.50×10^{17}	4.4×10^{15}	1.3×10^{15}	8.3×10^{13}	3.0×10^{15}
3	2.25×10^{17}	6.6×10^{15}	1.9×10^{15}	1.2×10^{14}	4.5×10^{15}
4	3.38×10^{17}	9.9×10^{15}	2.8×10^{15}	1.9×10^{14}	6.7×10^{15}
5	7.50×10^{17}	2.2×10^{16}	6.3×10^{15}	4.1×10^{14}	1.5×10^{16}
6	1.88×10^{18}	5.5×10^{16}	1.6×10^{16}	1.0×10^{15}	3.7×10^{16}
7	1.02×10^{17}	3.0×10^{15}	8.6×10^{14}	5.6×10^{13}	2.0×10^{15}
8	1.14×10^{17}	3.4×10^{15}	9.6×10^{15}	6.3×10^{13}	2.3×10^{15}
9	1.92×10^{17}	5.7×10^{15}	1.6×10^{15}	1.1×10^{14}	3.8×10^{15}
10	9.25×10^{17}	2.7×10^{16}	7.8×10^{15}	5.1×10^{14}	1.8×10^{16}
11	1.65×10^{18}	4.9×10^{16}	1.4×10^{16}	9.1×10^{14}	3.3×10^{16}
12	3.33×10^{18}	9.8×10^{16}	2.8×10^{16}	1.8×10^{15}	6.6×10^{16}
13	1.24×10^{18}	3.7×10^{16}	1.0×10^{16}	6.8×10^{14}	2.5×10^{16}
14	1.32×10^{18}	3.9×10^{16}	1.1×10^{16}	7.3×10^{14}	2.6×10^{16}
15	1.54×10^{18}	4.5×10^{16}	1.3×10^{16}	8.5×10^{14}	3.1×10^{16}
16	2.07×10^{18}	6.1×10^{16}	1.7×10^{16}	1.1×10^{15}	4.1×10^{16}
17	2.44×10^{18}	7.2×10^{16}	2.0×10^{16}	1.3×10^{15}	4.9×10^{16}
18	2.61×10^{18}	7.7×10^{16}	2.2×10^{16}	1.4×10^{15}	5.2×10^{16}
19	2.75×10^{18}	8.1×10^{16}	2.3×10^{16}	1.5×10^{15}	5.5×10^{16}
23	3.60×10^{18}	1.0×10^{17}	3.0×10^{16}	2.0×10^{15}	7.2×10^{16}
24	3.90×10^{18}	1.1×10^{17}	3.3×10^{16}	2.2×10^{15}	7.8×10^{16}
25	4.20×10^{18}	1.2×10^{17}	3.5×10^{16}	2.3×10^{15}	8.4×10^{16}

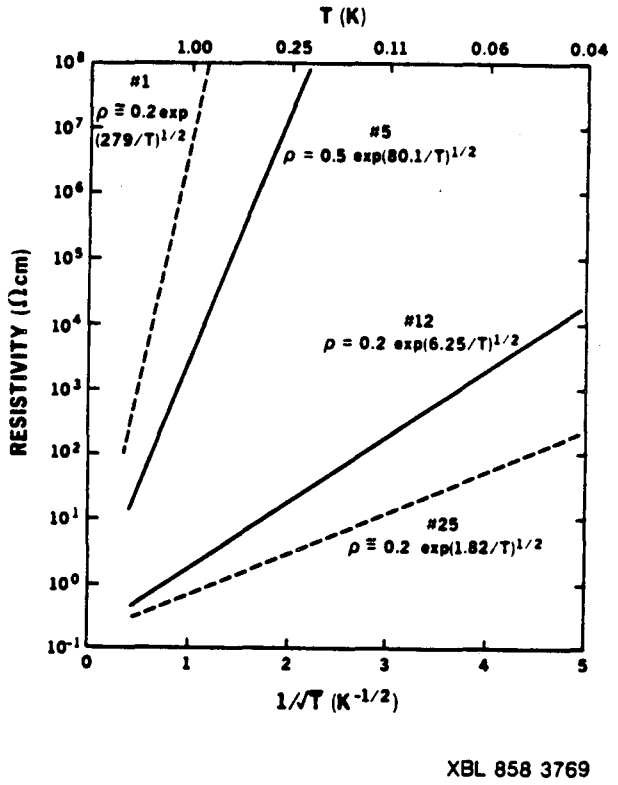

Fig. 6.4 Resistivity range of NTD germanium bolometer materials.

line of each device is within ~ 5%. This also shows the linear dependence of ln ρ vs. $T^{-1/2}$. The deviation at the lowest temperature region (below 100 mK) is assumed to be due to self heating of the resistor. From Fig. 6.3 we expect that NTD 12 may have too high a resistivity to be used below 40 mK. For application in the ~ 20 mK range, we prepared three more heavily doped NTD germanium samples (NTD 23, 24 and 25). Table 6.1 shows the notations and doping concentrations of the various NTD germanium samples produced in this study. In Fig. 6.4, the resistivity ranges are shown.

Bolometers made from these materials have given excellent performances in laboratory experiments [100] as well as in airborne astronomy [101].

6.4 Discussion on Hopping Conduction

In 1960, Fritzsche and Cuevas experimentally studied the impurity conduction in semiconductors using NTD germanium [2]. The reason they chose NTD germanium was that they could obtain uniform doping and a fixed compensation ratio for samples doped to different concentrations. They found that the resistivity of NTD germanium depends linearly on the inverse absolute temperature in the hopping regime. The activation energy of hopping (E_3, derived from the slope of the straight line in the hopping conduction range) was almost independent of the doping concentration of the sample, but the preexponential factor, ρ_0, was dependent upon the doping concentration. The study was limited by the fixed compensation ratio and the comparably high temperature region (300 K ~ 1.2 K). Miller and Abrahams [102] used the network resistance model in calculating the parameters of impurity conduction in p-type germanium ($N_D < 5 \times 10^{15}$ cm^{-3}, the overlap of neighboring wavefunction is small), and showed that the resistivity depends on temperature as:

$$\rho = C r_A^{-\frac{11}{4}} \exp\left[1.09\left(\frac{r_A}{a}\right)^{\frac{3}{2}}\right] \exp\left(\frac{E}{kT}\right) \qquad (6.12)$$

where C is a constant, $r_A = (3/4\pi N_A)^{1/3}$ is the average acceptor

separation, a is analogous to the Bohr radius of the hydrogen 1-s wave function. This relation is in accordance with Fritzsche and Cuevas' results. The activation energy of hopping conduction calculated by Miller and Abrahams is given by:

$$E = \left(\frac{e^2}{\varepsilon}\right)\left(\frac{4\pi N}{3}\right)^{\frac{1}{3}}\left(1 - 1.35K^{\frac{1}{3}}\right) \qquad (6.13)$$

where ε is the dielectric constant, N is the concentration of majority impurity, and K is the compensation ratio. This relation, again, showed moderate agreement with Fritzsche and Cuevas' result.

There are two points to be considered from the above discussion. One is that the activation energy of hopping conduction does not depend on the doping concentration or decrease with the doping concentration. The other is the 1/T dependence of resistivity in the hopping conduction regime. These two points are contradictory to our measurements shown in Figs. 6.2 and 6.3.

NTD germanium bolometer material can be considered as a disordered system in which the electronic states are localized at the Fermi level. Mott [103] derived the dependence $\ln \sigma \sim T^{-1/4}$ for the DC conductivity for such a system assuming that the density of states near the Fermi level is constant. This dependence of resistivity on temperature also does not agree with our measurements.

Pollak [104] and Ambegaokar et al [105] pointed out that electron-electron Coulomb interaction should reduce the density of states near the Fermi level. Efros and Shklovskii [98] have shown that the

long-range Coulomb interaction diminishes the density of states in the vicinity of the Fermi level in such a way that the density of states approaches zero as:

$$g(E) \sim E^{|d-1|} \tag{6.14}$$

or more rapidly if the energy approaches the Fermi level. Here, g(E) is the density of states, E is the difference between the energy and the Fermi level, and d is the space dimensionality. This Coulomb gap plays an important role in the low temperature DC conductivity. For the three dimensional case, the energy interval of width $\epsilon_M = T^{3/4}/a^{3/4}g_0^{1/4}$ is responsible for the hopping conductivity, which obeys the Mott law (here a is the localization length). The influence of the gap can be neglected if $\epsilon_M \gg \Delta$; i.e., $T \gg T_c = e^4 a g_0/\epsilon^2$, at such temperatures the Mott law is valid. If $T \ll T_c$ the states within the Coulomb gap are particularly important. Efros and Shklovskii obtained:

$$\sigma(T) \sim \exp[-(\frac{T_0}{T})^{\frac{1}{2}}] \tag{6.15}$$

where $T_0 = e^2/\epsilon a$.

Our resistivity measurements of NTD germanium down to low temperatures (< 4.2 K) in Figs. 6.2 and 6.3 show that the plot of ln ρ vs. $T^{-1/2}$ yields a best fit in agreement with Efros and Shklovskii's theory. Unlike from the data of Fritzsche, the slope of straight line is different for different doping concentrations (but same

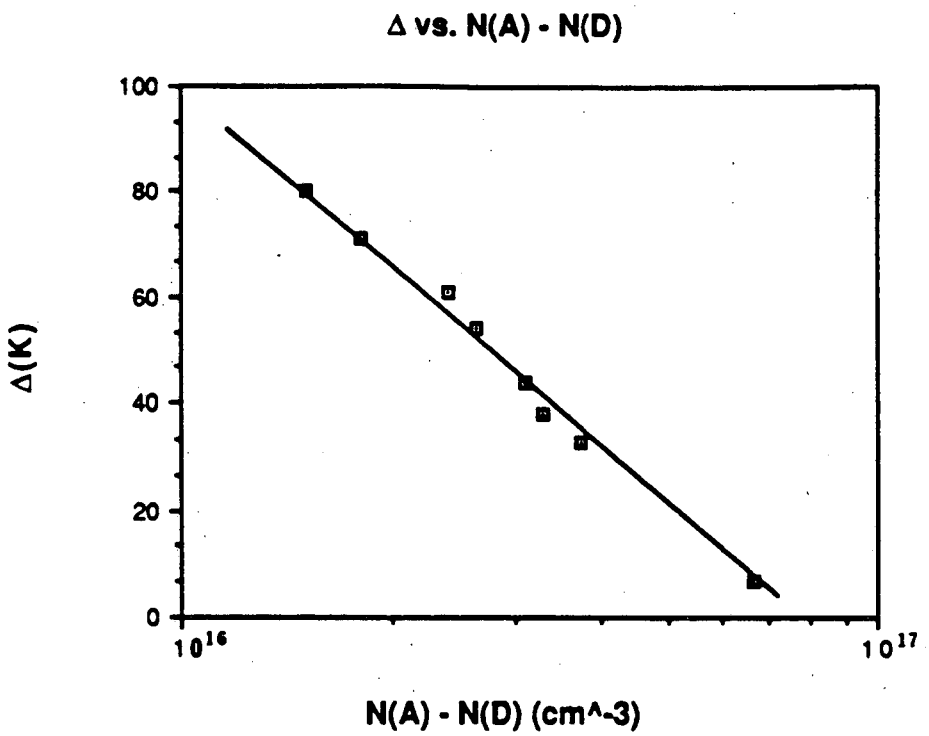

XBL 885-1531

Fig. 6.5 Plot of Δ vs. $N_A - N_D$ obtained from Fig. 6.2.

compensation ratio). This is the expected result because the higher the doping concentration, the smaller the jumping distance of carriers, and the more easily hopping conduction does occur. Obtaining an activation for hopping in such a plot is not straightforward because the plot is not Arrhenius like (thermally activated process). But the slope of the straight line in Fig. 6.2 (designated as Δ) should have a unit of temperature, or Δ/k should have a unit of energy (here assumed to be the energy required for carriers to jump into the neighboring empty site).

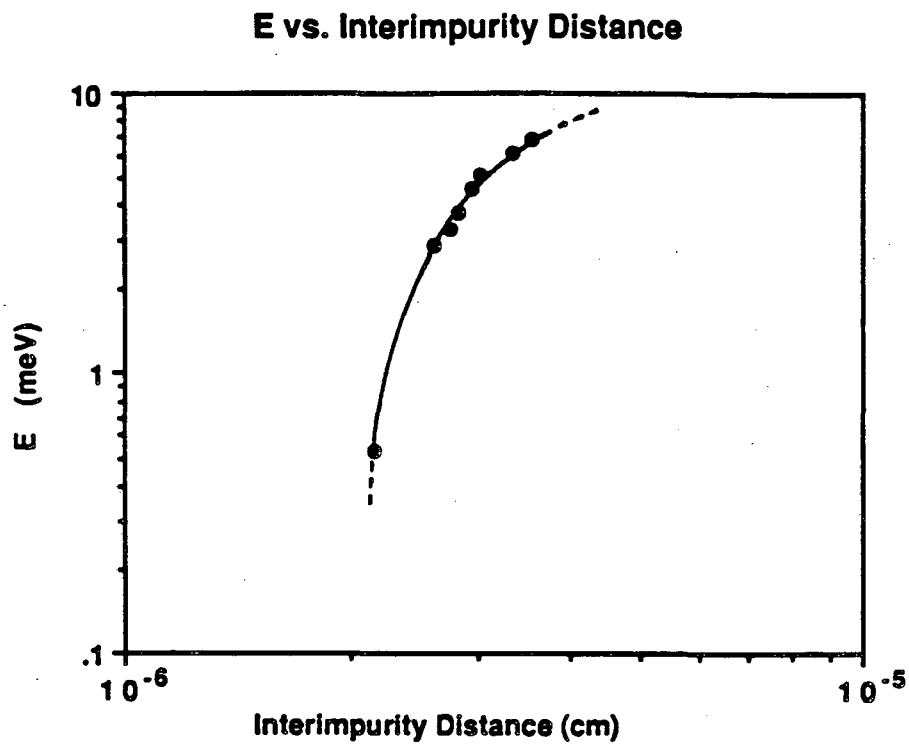

XBL 885-1813

Fig. 6.6 Plot of E (= Δ x k) vs. interimpurity distance of NTD germanium samples.

From the plot of ln ρ vs. $T^{-1/2}$, we obtain Δ for concentration range 10^{15} cm^{-3} ~ 10^{16} cm^{-3}. The values of Δ obtained from Fig. 6.2 are plotted as a function of net doping concentration in Fig. 6.5. The plot yields a straight line approaching zero as the doping concentration increases and linearly increasing on the other end. But in the region close to $N_A - N_D = 0$, the value cannot increase beyond 11.3 meV which is the ionization energy of gallium acceptor in germanium (if this value is somewhat related to the activation of hopping or conduction). Hopping conduction is based on the hopping of

carriers from occupied to empty sites. We can also calculate the distances between the occupied and empty sites assuming the impurities are extremely uniformly distributed. Figure 6.6 is a plot of E (= Δ x k) vs. interimpurity distance in NTD germanium.

Although the data obtained so far indicates that the resistivity vs. temperature behavior of our samples shows a very good fit to Efros' theory, it is ambiguous to interprete the hopping conduction mechanism from the results shown in Figs. 6.5 and 6.6 mainly because the best plot is not Arrhenius-type. There is also a possibility that there are several temperature ranges in the hopping conduction regime so that the dependence of the resistivity on temperature shows different behavior as in Pollak's paper [104]. If this is true, the hopping conduction mechanism may vary for different temperature range showing a different dependence of the resistivity on temperature.

To understand the hopping conduction mechanism more thoroughly, we need to have more resistivity measurements of samples with large range of doping concentrations and with different compensation ratios.

7. Far-Infrared Mixers

The bandgap energies and ionization energies of impurities in semiconductors usually fall within the infrared wavelength range. When a semiconductor absorbs photons with energies appropriate to excite carriers into the conduction or valence band, the conductivity of semiconductor changes and this change in conductivity is used to create a signal. The photoconductivity of semiconductors is very

useful in the detection of infrared radiation. When the photons absorbed by semiconductor excite electrons from the valence band to the conduction band, the photoconductivity is called "intrinsic". When the photons are absorbed in the process of exciting electrons (n-type) or holes (p-type) from impurity levels, the photoconductivity is called "extrinsic". Many extrinsic germanium photoconductors have been developed that provide high sensitivity for infrared astronomical observations [106]. State-of-the-art detectors have a sensitivity close to the theoretical limit (background limited impurity photoconductor, BLIP).

Extrinsic germanium phtoconductors exhibit good response for many spectral lines from molecules in planetary atmospheres. But the response speed of ordinary photoconductors (~ 10^{-6} sec which corresponds to a bandwidth of 0.16 MHz) is not fast enough to detect those narrow spectral lines which are very high frequency signals. For example, the CO_2 line near 10 μm and the OH line near 119 μm have linewidths of ~ 10^{-3} cm^{-1} (corresponds to 30 MHz of bandwidth). In the high resolution study of such narrow spectral lines, a heterodyne technique is used. In the heterodyne technique, a signal radiation is mixed with the coherent output of a laser serving as a local oscillator. This produces a difference frequency spectrum at radio frequencies. The much lower frequencies can be amplified with very little increases in noise. For efficient mixing, we need high speed, square-law devices.

Extrinsic germanium photoconductors, which are square-law devices, have shown excellent performance in the direct detection of

far-infrared radiation. Therefore, we conducted a study of the performance of gallium-doped germanium photoconductors as heterodyne detectors. The response speed of a photoconductor can be increased by an increase in compensation. The NTD process provides an excellent way of introducing impurities into pure and doped semiconductors. We chose NTD in combination with bulk doped germanium for the development of a far-infrared gallium-doped germanium photoconductive mixers.

Although the literature on copper-doped germanium (Ge:Cu) heterodyne detectors is very extensive for CO_2 laser wavelengths around 10.6 μm [107,108], not much work has been done in the far-infrared region ($\lambda > 30$ μm). Only one paper describing mixer performance of gallium-doped germanium (Ge:Ga) photoconductor at 118.6 μm (water-vapor emission line) [109] has come to our attention. In this work, the poor detector performance has been attributed to the high intrinsic noise equivalent power (NEP) of the detector. In our studies, we have established a direct, quantitative correspondence between semiconductor materials parameters (such as acceptor and donor dopant concentrations) and heterodyne detector parameters such as responsivity, NEP, and bandwidth.

7.1 Basic Operation Mechanisms

7.1.1 Photoconductors

Photoconductivity in extrinsically doped germanium is observed when infrared photons are absorbed by neutral impurities. The latter

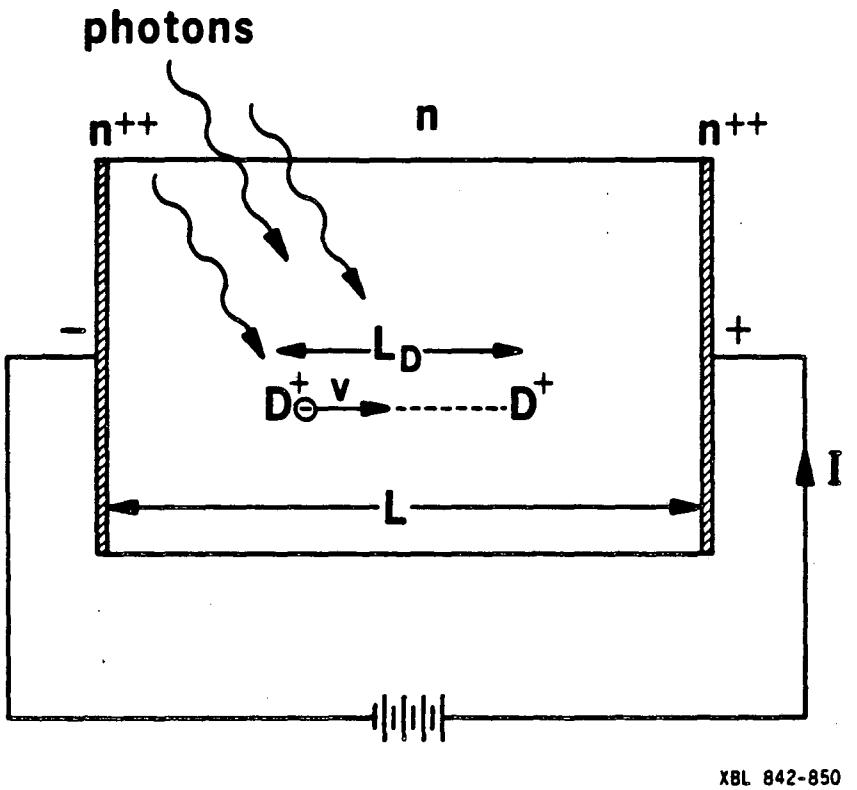

Fig. 7.1 Schematic diagram of a photoconductor.

are ionized to create free carriers. These free carriers will change the conductivity of germanium, and the corresponding change in current or voltage, the signal, is amplified. The relationship between ionization energy E_I and threshold wavelength λ is:

$$E_I = \frac{hc}{\lambda} \tag{7.1}$$

where h is Planck's constant and c is the speed of light.

Figure 7.1 shows the schematic of a photoconductor. A carrier is

set free by the absorption of incident photons and drifts towards the contact electrode. If it does not recombine until it arrives at the electrode, it is immediately replaced with a carrier injected at the opposite electrode. The overall distance a carrier travels is:

$$l = \tau \mu E \tag{7.2}$$

where τ is the carrier lifetime, μ is the carrier mobility, and E is the applied electric field. The photoconductive gain G is defined as the average distance a carrier travels divided by the interelectrode distance L:

$$G = l/L = \tau/T = \tau \mu E/L \tag{7.3}$$

where T is transit time for carriers to drift across the photoconductor.

When a photoconductor is exposed to a beam of incident radiation of power P, modulated at angular frequency ω, a photocurrent I is induced:

$$I = \frac{P}{h\nu} \frac{e\eta G}{(1 + \omega^2 \tau^2)} \tag{7.4}$$

where h = Planck's constant, ν = frequency ($= \omega/2\pi$), e = electron charge, and η = quantum efficiency (number of carriers produced divided by number of incident photons). In characterizing the

performance of photoconductors, we use responsivity and noise equivalent power (NEP).

The responsivity is the response (in current or voltage) of the detector per unit power of incident photons:

$$R = (e/h\nu)G\eta \ (A/W) \tag{7.5}$$

The NEP is the ultimate sensivity of a detector and is defined as the signal power required to get a signal-to-noise ratio of unity per unit detection bandwidth. This can be expressed as:

$$NEP = \frac{P_s}{(S/N)} \ (W/\sqrt{Hz}) \tag{7.6}$$

where P_s is the signal power, S/N is the signal-to-noise ratio.

In the detection of a signal there is unavoidable noise due to the fluctuation of photons from the background radiation called photon noise. Detector whose noise is dominated by this background noise is called BLIP (background limited impurity photoconductor) detector and the minimum detectable power is:

$$P_s = 2\left(\frac{P_b h\nu B}{\eta}\right)^{\frac{1}{2}} \tag{7.7}$$

where P_b is the background radiation power and B is the detection bandwidth.

7.1.2 Mixers

Extrinsic photoconductors used to detect infrared and submillimeter radiation are square law devices: their voltage output is proportional to the radiation power input [110]. If a detector of this type is exposed to two beams of radiation of similar wavelength, the detector voltage will oscillate at a frequency $(\nu_1 - \nu_2)$ with amplitude proportional to $(P_1P_2)^{1/2}$, where ν_1, ν_2 and P_1, P_2 are the frequencies and the powers of the two beams, respectively. The heterodyne detector's main function is this conversion of signals from high (IR) frequencies down to frequencies which can be amplified easily and filtered with good signal-to-noise ratio.

The classical heterodyne theory is as follows; when two electromagnetic waves with different frequencies arrive at the square-law device, the total electric field E_t is:

$$E_t = E_1\cos(\omega_1 t) + E_2\cos(\omega_2 t + \phi) \tag{7.8}$$

and the response R of the detector is proportional to E_t^2:

$$R_t \sim E_t^2 = E_1^2\cos^2(\omega_1 t) + E_2^2\cos^2(\omega_2 t)$$
$$+ E_1E_2\cos(\omega_1 - \omega_2)t + E_1E_2\cos(\omega_1 + \omega_2)t \tag{7.9}$$

Here we assume that the speed of the detector cannot follow the signal at double (first and second term) and sum (last term) frequencies.

Therefore, the response of the detector is proportional to the third term in the above equation which has a frequency $(\omega_1 - \omega_2)$. In this measurement system, we mix the signal radiation with a coherent output of a local oscillator. The local oscillator is a local IR-source (typically a FIR laser). The difference (or intermediate) frequency signal is proportional to the product of both signals, i.e., high local oscillator power leads to a large intermediate frequency signal. Also we convert the signal frequency to a frequency range in which we have good amplifiers. Now the mean-squared IF (intermediate frequency) current is [110]:

$$i_{IF}^2 = 2 i_{LO} i_s$$

$$= \frac{2\eta^2 G^2 e^2}{h^2 \nu^2} P_{LO} P_s \qquad (7.10)$$

where i_{LO} = signal current due to local oscillator power, i_s = signal current, η = quantum efficiency, G = photoconductive gain, e = electron charge, h = Planck's constant, ν = frequency, P_{LO} = local oscillator power, and P_s = incident signal power. The mean-squared noise current is:

$$i_n^2 = 4e^2 G^2 \eta \frac{P_{LO} B}{h\nu} + \frac{4kT_L B}{R_L} \qquad (7.11)$$

where B is the detection bandwidth, T_L = temperature of the resistor, R_L = resistance of the load resistor. The first term is

the G-R noise due to the laser local oscillator and the second term is the noise of the detector and load resistor assembly. The ideal heterodyne detector system is the one in which the noise is dominated by G-R noise from the LO power. For this system to be quantum G-R noise limited:

$$P_{LO} > \frac{kT_L h\nu}{G^2 e^2 \eta R_L} \tag{7.12}$$

and the minimum detectable power is:

$$P_s = \frac{2h\nu B}{\eta} \tag{7.13}$$

7.2 Detector Fabrication

For the heterodyne measurement technique we need a high speed (large bandwidth), square-law detector. Ordinary photoconductors have carrier lifetimes of about 10^{-6} seconds. Such a lifetime corresponds to a bandwidth of 0.16 MHz. The spectral lines from planetary atmospheres have linewidth ~ 10^{-3} cm^{-1} which corresponds to about 30 MHz of bandwidth, many times larger than the bandwidth of a regular photoconductor. Gallium-doped germanium (Ge:Ga) photoconductors show high responsivity around 100 μm which would facillitate mixing the spectral line from the OH molecule (118 μm) with a stable, strong laser line available at 118.8 μm from the optically pumped CH_3OH laser.

The main requirements of a good heterodyne detector are; i) large recombination bandwidth ($B \sim 1/\tau$, τ = carrier recombination time), ii) high quantum efficiency η for better sensitity, and iii) short interelectrode distance for large photoconductive gain G.

The principal way of obtaining large bandwidth detectors is to reduce the carrier lifetime by increasing the number of recombination centers. If we increase the number of the compensating impurities, the concentration of empty (i.e., ionized) centers increases and these ionized centers act as recombination centers for majority carriers. Unfortunately, the compensation reduces the responsivity of the detector by decreasing the carrier lifetime and mobility. In the heterodyne measurement, however, the signal radiation is mixed with strong laser local oscillator and resultant signal power is increased as $\sqrt{P_{LO}P_s}$.

High quantum efficiency of a detector can be obtained by the use of an integrating cavity and high doping concentration of detector material (high absorption of photons due to the presence of many neutral impurities). A cylindrical integrating cavity was used in the measurements of detector performances throughout this study. The high limit of doping concentration of a detector material is set by the signal-to-noise ratio consideration. The use of a high power local oscillator will enable us to increase the doping concentration.

The photoconductive gain G can be increased by using a short interelectrode distance as expected from equation (7.3). The detector thickness is limited by the convenience of handling and the consideration of absorbing area of incident photons (i.e., quantum

efficiency).

7.2.1 Single Crystal Growth

To achieve a certain compensation in a semiconductor, we can incorporate both n- and p-type impurities during the crystal growth stage of detector material. This method is somewhat unpredictable making it difficult to get the desired doping concentration and compensation ratio at the same time. We used the NTD technique to counter-dope germanium samples. A germanium single crystal was grown doped with n-type impurity (phosphorus). P-type impurity (gallium) were then incorporated by the NTD process. This technique is reproducible and the desired compensation ratio of a germanium sample is easily obtained.

The gallium concentration of our detector covered three ranges: 3 x 10^{14} cm^{-3} (series 20), 6 x 10^{14} cm^{-3} (series 21), and 1 x 10^{15} cm^{-3} (series 22) with compensation ratios ranging between 0.32 and 0.8. As NTD produces acceptors (gallium) and donors (arsenic and selenium) in the ratio of about 3:1 in germanium, we grew an n-type single crystal (phosphorus-doped) rather than p-type to get the maximum range of compensation ratio.

Doping of a germanium single crystal is usually achieved by adding a small amount of master-alloy (heavily doped germanium crystal) to the melt. Because of the segregation of solute atoms in the melt, a single crystal does not have a uniform concentration of impurities but has a concentration profile along the crystal axis. The segregation

coefficient depends on the properties of the impurities. In most cases, the resultant doping concentration of the crystal is not exactly the same as calculated, and is more often determined empirically. The equilibrium segregation coefficient k_o of phosphorus in germanium is known as ~ 0.08. When one grows a single crystal from a doped melt, however, the equilibrium condition is not met because the crystal is pulled at finite speed. This results in a deviation from the equilibrium condition, and the effective segregation coefficient is different from the equilibrium segregation coefficient. The effective segregation coefficient of phosphorus in germanium is 0.25 determined empirically for our regular growth conditions. Using this value we can predict the doping profile from the head to the tail of the single crystal.

We wanted to have a doping concentration of 10^{14} cm^{-3} of phosphorus at the center of the crystal. The overall doping concentration is obtained from the normal freezing equation [111]:

$$C_s(g) = kC_o(1 - g)^{k - 1} \tag{7.14}$$

where $C_s(g)$ is the concentration of the crystal at solidification g, k is the effective segregation coefficient of solute (assumed 0.25 for phosphorus), and C_o is the overall concentration of solute throughout the crystal. By putting $C_s(0.5) = 10^{14}$ cm^{-3}, we obtain $C_o = 2.38 \times 10^{14}$ cm^{-3}. The doping concentration of the phosphorus master-alloy is 2×10^{18} cm^{-3}. For a charge of 800 g of pure germanium, we need 0.095 g of master-alloy to obtain the mean

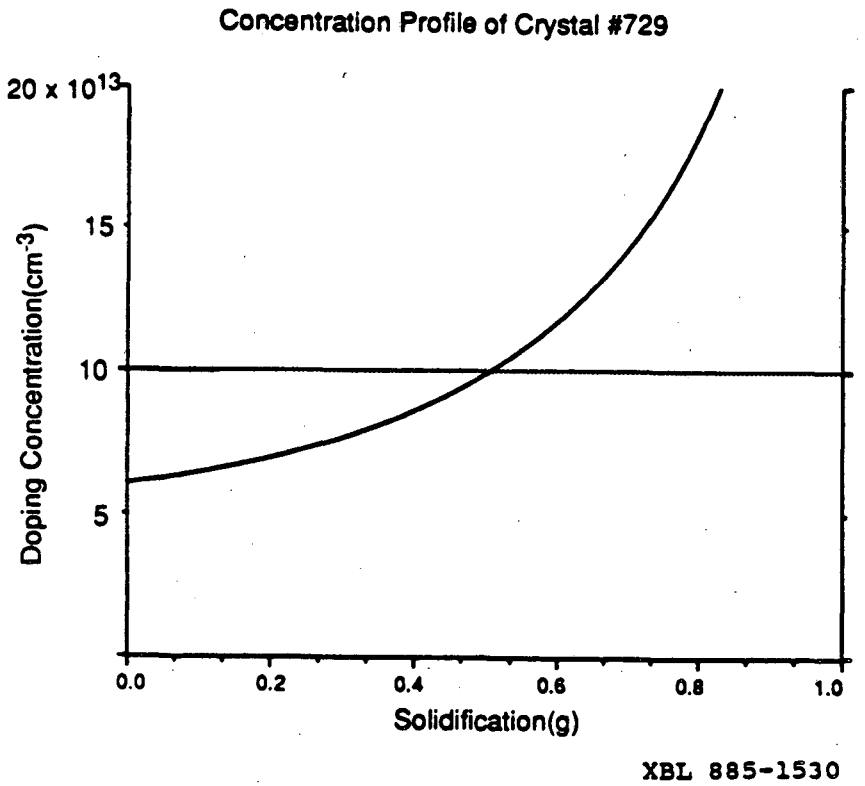

Fig. 7.2 Concentration profile of phosphorus-doped germanium single crystal 729.

melt concentration of 2.38 x 10^{14} cm^{-3}. The expected concentration profile is as shown in Fig. 7.2.

Precaution is needed when growing phosphorus-doped germanium because phosphorus has a high vapor pressure. In order to retain phosphorus in the crystal growth stage, the phosphorus-doped master alloy is placed at the top of the solid, polycrystalline charge so that it melts last. The concentration of compensating acceptor impurities in this crystal was estimated to be $1x10^{12}cm^{-3}$ as

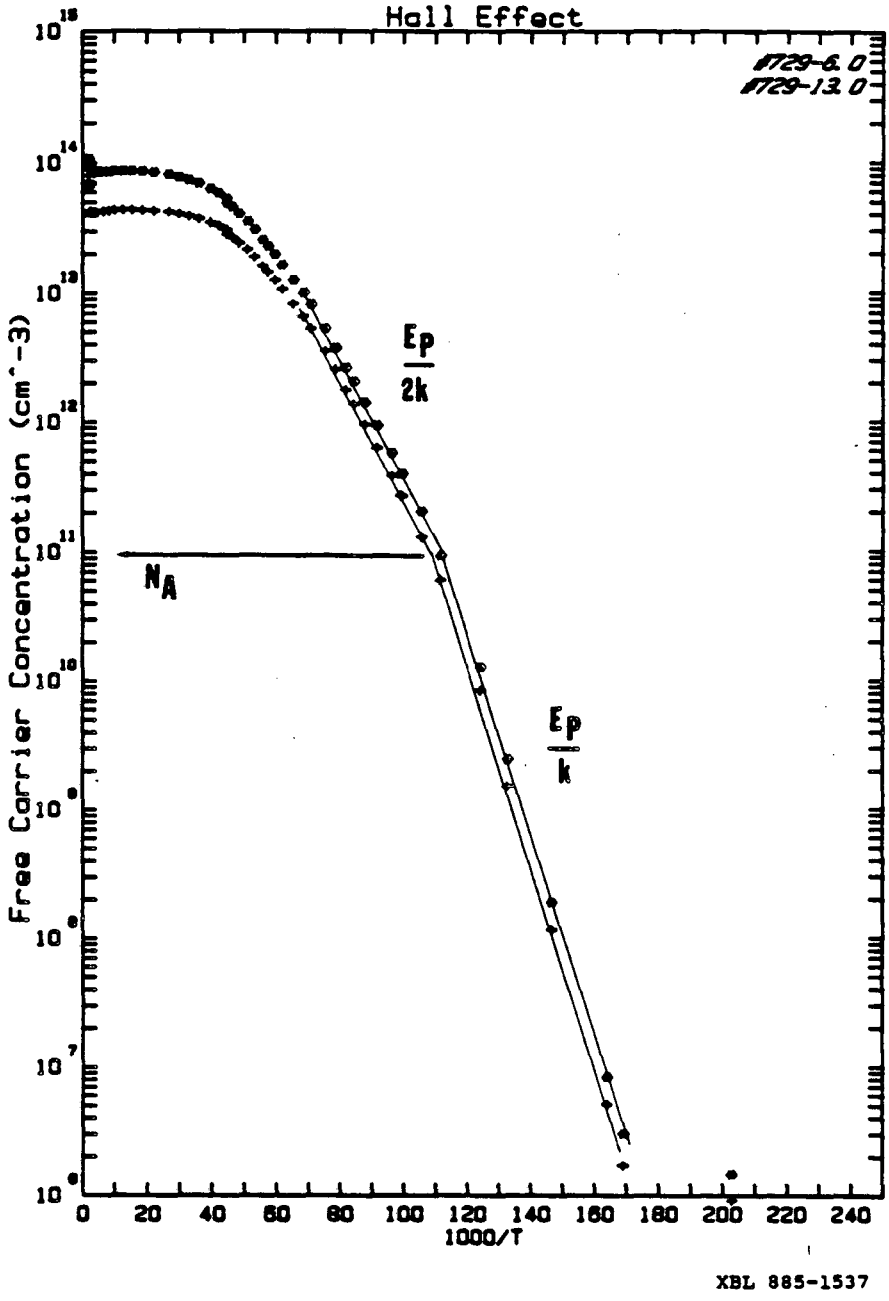

Fig. 7.3 Result of variable temperature Hall effect measurements of two wafers from crystal 729.

determined from variable temperature Hall effect measurements (Fig. 7.3).

7.2.2 Neutron Transmutation Doping (Counter Doping)

Neutron transmutation doping (NTD) was used to add further dopants (acceptors) to several 1 mm thick wafers of this crystal. NTD of germanium produces gallium acceptors and arsenic and selenium donors. By producing more gallium than the sum of the resultant donors, we have produced three series of samples with each series having a fixed acceptor concentration and varying amounts of compensating impurities (donors). To obtain gallium concentrations of ~ 3.2×10^{14} cm^{-3} (series 20), ~ 6.4×10^{14} cm^{-3} (series 21), and ~ 1×10^{15} cm^{-3} (series 22), we need thermal neutron doses of 1×10^{16} cm^{-2}, 2×10^{16} cm^{-2}, and 3.4×10^{16} cm^{-2}, respectively. With those doses of thermal neutrons, we also obtain 9.6×10^{13} cm^{-3}, 1.8×10^{14} cm^{-3}, and 3×10^{14} cm^{-3} donors for series 20, 21 and 22, respectively.

Slices with phosphorus concentration between 5×10^{13} cm^{-3} and 2×10^{14} cm^{-3} were taken to obtain the desired final donor concentration between 1.4×10^{14} cm^{-3} and 5×10^{14} cm^{-3} so that the compensation ratio changes between 0.32 and 0.8. Final concentrations of our samples are given in Table 7.1.

After NTD, germanium wafers were annealed at 400°C for 6 hrs in flowing Ar gas to remove the radiation damage caused mainly by fast neutrons and to activate impurities.

7.2.3 Contact Preparation and Size of Detectors

Ohmic contacts on these p-type detector material were produced by implantation with boron ($1x10^{14}cm^{-2}$ at 25kV and $2x10^{14}cm^{-2}$ at 50kV). These implant doses lead to degenerately (i.e., metallically) doped contact areas. 200 Å of Pd and 8000 Å of Au were sputtered on the implanted surface.

The photoconductive gain G of a detector is inversely proportional to the interelectrode distance L (i.e., thickness of detector). Figure 7.4 shows the effect of detector thickness on responsivity.

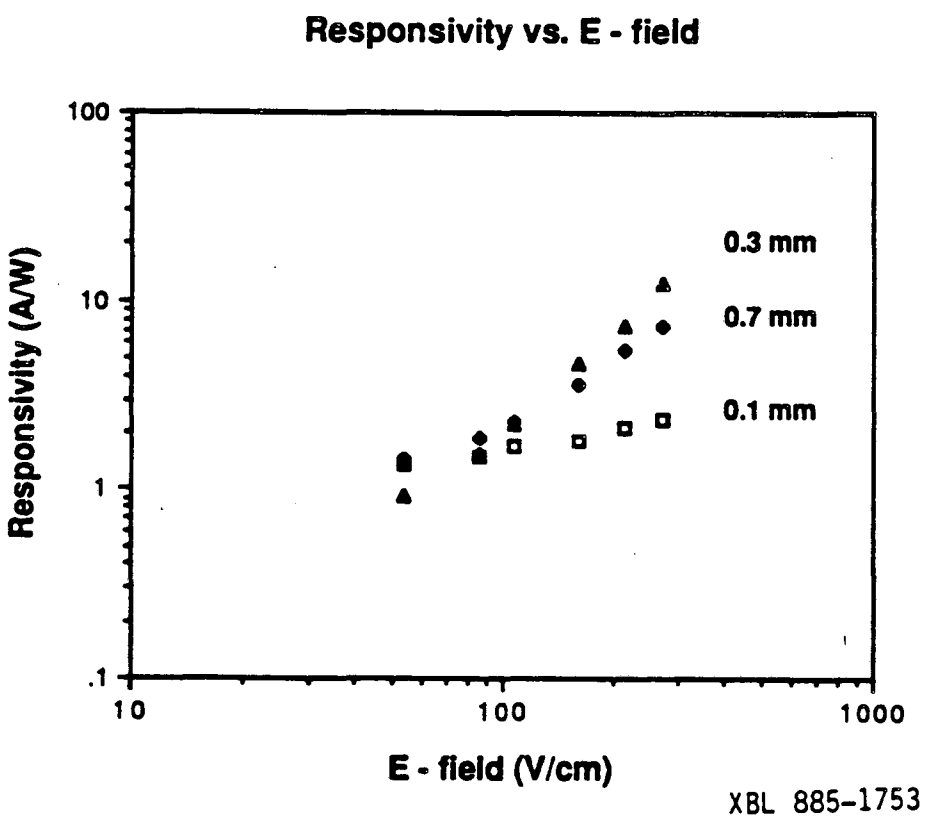

Fig. 7.4 Effect of thickness on responsivity (detector#108-18).

Table 7.1

Doping Concentrations of Samples(cm^{-3})

Series	Sample	As Grown	NTD		Final	
		$N_D(P)$	$N_A(Ga)$	$N_D(As+Se)$	N_A	N_D
20	496-5.5(20)	~ 10^{11}	$3x10^{14}$	$9.6x10^{13}$	$3x10^{14}$	$9.6x10^{13}$
	729-6.0(20)	$5.0x10^{13}$	$3x10^{14}$	$9.6x10^{13}$	$3x10^{14}$	$1.4x10^{14}$
	729-9.0(20)	$8.0x10^{13}$	$3x10^{14}$	$9.6x10^{13}$	$3x10^{14}$	$1.8x10^{14}$
	729-13.0(20)	$1.0x10^{14}$	$3x10^{14}$	$9.6x10^{13}$	$3x10^{14}$	$2.0x10^{14}$
21	729-6.4(21)	$5.0x10^{13}$	$6x10^{14}$	$1.9x10^{14}$	$6x10^{14}$	$2.4x10^{14}$
	729-9.4(21)	$8.0x10^{13}$	$6x10^{14}$	$1.9x10^{14}$	$6x10^{14}$	$2.7x10^{14}$
	729-14.6(21)	$1.5x10^{14}$	$6x10^{14}$	$1.9x10^{14}$	$6x10^{14}$	$3.4x10^{14}$
22	729-6.4(22)	$5.0x10^{13}$	$1x10^{15}$	$3.2x10^{14}$	$1x10^{15}$	$3.7x10^{14}$
	729-9.4(22)	$8.0x10^{13}$	$1x10^{15}$	$3.2x10^{14}$	$1x10^{15}$	$4.0x10^{14}$
	729-14.6(22)	$1.5x10^{14}$	$1x10^{15}$	$3.2x10^{14}$	$1x10^{15}$	$4.7x10^{14}$
	729-17.0(22)	$2.0x10^{14}$	$1x10^{15}$	$3.2x10^{14}$	$1x10^{15}$	$5.2x10^{14}$

The detector geometry was 3 x 1 x t mm^3 with electrodes on the 3 x 1 mm^2 surfaces. The responsivity of the 0.3 mm thick sample shows the higher responsivity than that of the 0.7 mm thick sample. However, the 0.1 mm thick sample shows responsivity values much lower than those of the thicker samples. This is believed to be due to the very small absorbing area of the sample. The 0.3 mm thick sample showed the highest responsivity, but it is quite difficult to handle. The

detector thickness was therefore chosen to be 0.5 mm compromising between the optimum responsivity and the ease of handling.

7.3 Measurement of Detector Performance

7.3.1 Direct Photoconductivity Measurements

Current responsivity, which is proportional to the product of quantum efficiency η and photoconductive gain G, was measured with direct (incoherent) detection at $\lambda = 93$ μm (near the peak of the Ge:Ga spectral response) by use of a liquid-helium temperature cooled narrow-band filter. Through this filter, the detector receives radiation from a 300 K blackbody chopped at 20 Hz against a 77 K blackbody. The total background incident on the detectors in this case was approximately 10^{-13} W.

The dewar used for photoconductivity measurement was obtained from Infrared Laboratories (Model HD3), Tucson, Arizona. It consists of a liquid helium space with a volume of approximately 1 liter shielded with a liquid nitrogen jacket. Vacuum space provides thermal insulation. The detector, cavity, and filter train are mounted in a light-tight box which is mounted to a thick copper plate which is in contact with the liquid helium bath. The filters were fabricated and characterized in Professor Charles Townes' group by Dan Watson of the Physics Department, U.C. Berkeley [112]. Table 7.2 contains the descriptions and measured transmission for filters which were used for testing at 93 μm. This filter was designed so that λ_{peak} coincides

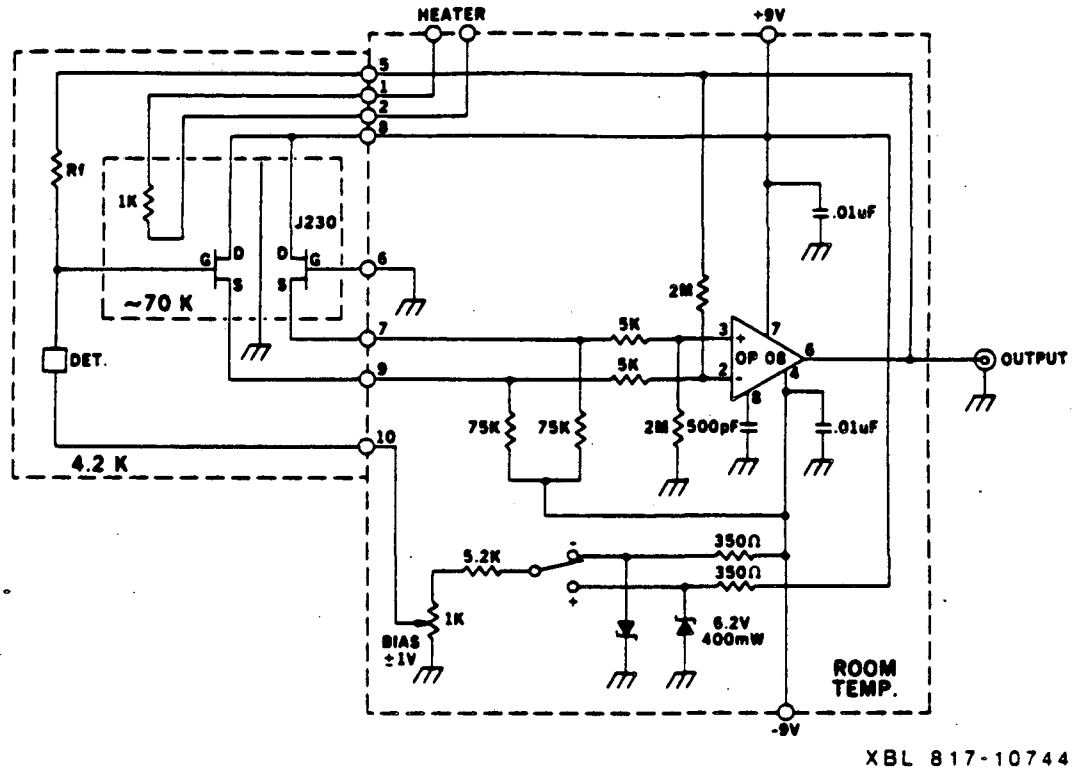

Fig. 7.5 Schematic diagram of transimpedence amplifier circuit used in the photoconductivity measurements.

approximately with the peak of the spectral response of a Ge:Ga photoconductor. The filters are independently mounted along the optical axis on sliding baffles and are heat sunk directly to the copper plate by two screws and pure indium foil. This system provides the condition for infrared astronomy of low background (10^6 ~ 10^{10} photons/sec).

The detector is located inside its integrating cavity at the far end of the box. The use of the integrating cavity increases the

quantum efficiency. The temperature of the detector and its surroundings is monitored by a 1 kΩ Allen-Bradley carbon composite resistor. The resistor is enclosed in a small copper block and heat sunk to the copper plate.

The photoconductor signal is amplified by a standard transimpedance amplifier shown in Fig. 7.5. The input stage consists of two matched junction FETs (J230). The JFETs are located inside a light-tight copper housing with glass feed-throughs which are opaque to FIR radiation. They are mounted off the He temperature plate on a thin wall fiberglass tube. A 1 kΩ Allen-Bradley resistor is glued with epoxy resin to the JFETs. A constant voltage applied across the resistor together with the power dissipated by the JFETs keeps the operating temperature at approximately 77 K. The feedback resistor connecting the output to the gate is an Eltec Model 102 resistor with a room temperature resistance of $10^{10}\Omega$. The resistance increases to $2.35 \times 10^{10}\Omega$ when cooled to 4.2 K. The voltage drop measured across the feedback resistor (i.e., output voltage) is divided by the feedback resistance to obtain the value of the current flow through the detector under a fixed bias. The output signal from the transimpedance amplifier is fed directly into a lock-in amplifier (EG & G, Model 116) to measurable rms value of the chopped signal. Noise measurements are obtained with the aid of a Hewlett-Packard Model 3582A Fast Fourier Transform spectrum analyzer.

It has been reported that the optimum concentration of shallow impurity in an extrinsic germanium photoconductor is $\sim 2 \times 10^{14}$ cm^{-3}. Our detectors are, however, doped more heavily (with high

Table 7.2

Filter Characteristics

λ(peak)	Filter Components	Transmission	Bandwidth ($\pi/2\Delta\lambda$FWHM)	Q
	93 μm Fabry-Perot			
	0.5 mm KCl			
93.2 μm	1.0 mm BaF_2	27%	1.05 μm	140
	2 mil black polyethylene			
	1 monolayer 6-12 μm diamond dust			
	7 mg ZnO			

compensation ratio) than the optimum concentration to increase the recombination bandwidth and therefore showed low responsivity and large dark current. In Fig. 7.6, the responsivity and NEP of 729-14.6(21) detector at 93 μm are shown. The maximum responsivity is about 1 A/W near breakdown. This value is more than an order of magnitude smaller than that of state-of-the-art gallium-doped germanium photoconductor [106]. This is the result of short carrier recombination time (due to high compensation) and low carrier drift mobility. NEP value of the detector is in the range ~ 10^{-14} W/ Hz which is about two orders of magnitude greater than the theoretical limit. This is mainly due to the presence of large dark current caused by hopping conduction [113]. For the most heavily doped detectors (22-series), the noise associated with the dark current due to hopping conduction overwhelmed the photocurrent and it was

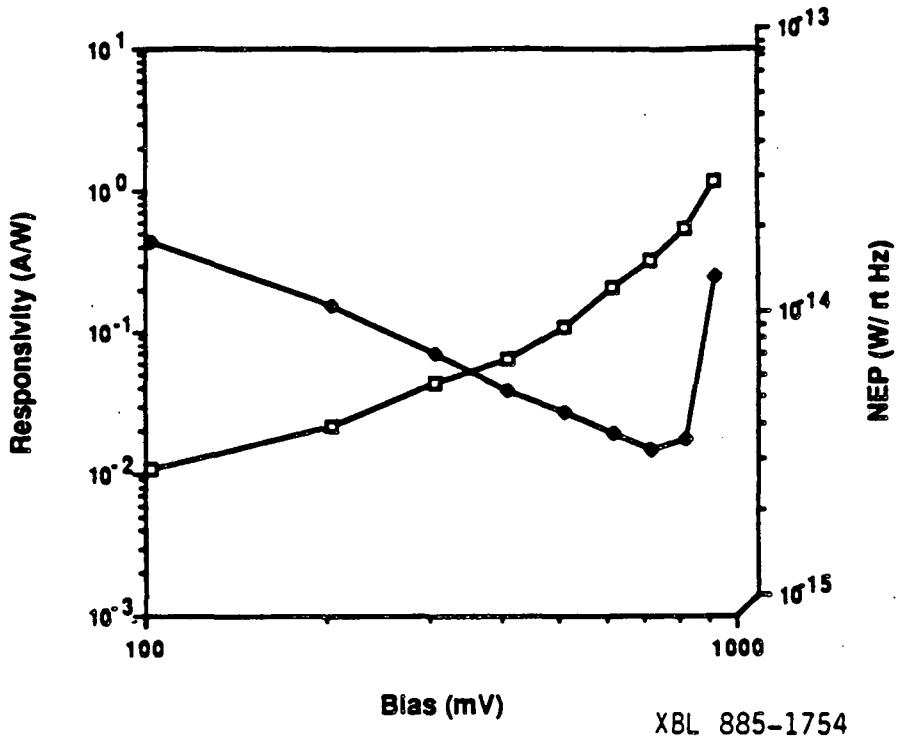

Fig. 7.6 Responsivity and NEP of detector #729-14.6(21) at 93 μm.

impossible to get any signal at the low-background condition (~ 10^{-13} W) because of the low signal-to-noise ratio. In the case of detector 729-9.4(22), for example, the shot-like noise due to hopping conduction was about five times larger than the signal. A simple estimate agrees well with our experimental result. From the measured value of dark current I_{DC} the rms noise current I_n for unit detection bandwidth can be calculated as:

$$I_n^2 = GeI_{DC}B \tag{7.19}$$

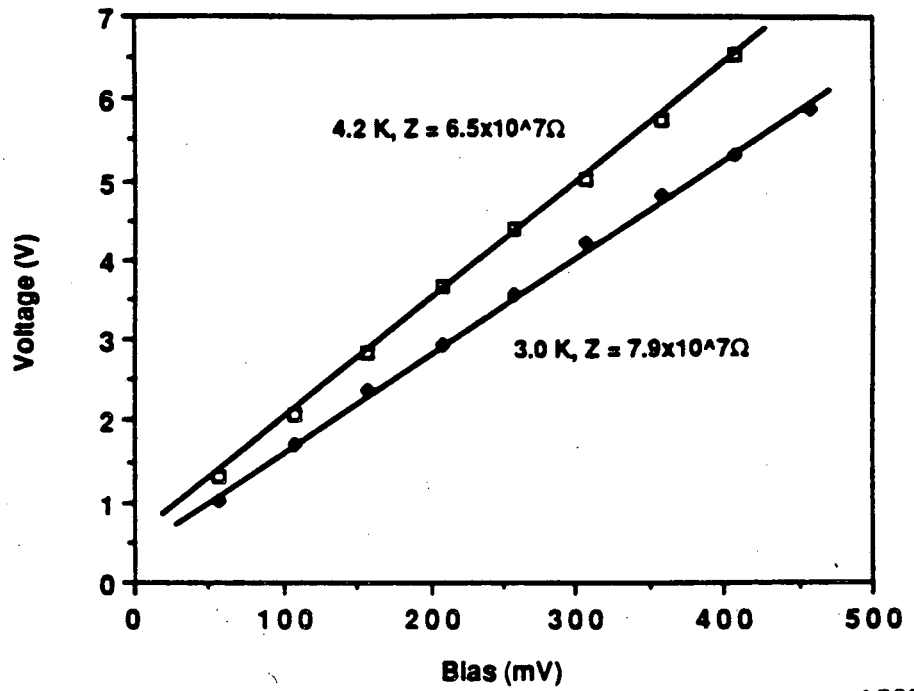

XBL 885-1755

Fig. 7.7 Dark voltage of #729-94.(22) measured with $10^9\Omega$ load resistor.

where e is the electron charge (= 1.6×10^{-19} C) and B is the detection bandwidth. Figure 7.7 is the dark voltage of #729-9.4(22) measured with $10^9\Omega$ load resistor. At 400 mV bias, I_{DC} = 6.6×10^{-9} A, and we obtain $I_n = 3.2\times10^{-14}$ A for unit bandwidth. The photon signal current is:

$$I_s = \frac{\Delta ne}{T} = \frac{\Delta ne\mu E}{L} \tag{7.20}$$

with $\Delta n = (P_{signal}/h\nu)$, i.e., the number of photogenerated

carriers. T is the transit time for carriers across the electrode, μ is the mobility and E is the applied electric field. At λ = 93 μm, $P_{signal}/h\nu = 4.8\times10^{7}$ sec^{-1}, and with the measured value of μ = 5×10^{3} $cm^2/Vsec$, estimated τ of about 10^{-9} sec, and E = 400 mV/0.05 cm = 8 V/cm, we obtain $I_s = 6.1\times10^{-15}$ A resulting in $I_s/I_n = 1.9\times10^{-1}$.

The direct photoconductivity measurements of 22-series detectors were, therefore, performed with increased incident flux by removing the Fabry-Perot narrowband filter from the filter train. The incident photons are limited by the absorption edge of the detector material (~ 120 μm) at the low energy end and by the cut-off of the lowpass filter at the high energy end (~ 80 μm) as shown schematically in Fig. 7.8. The calibration factor was obtained by measuring the increase in the signal of detector 729-6.0(20) after removing the Fabry-Perot filter. From the increase in the signal (Fig. 7.9), the calibration factor was determined to be 30. The 22-series detectors were then measured without the Fabry-Perot filter, and the measured signal output value was divided by 30 to obtain the responsivity. In the heterodyne measurement with a laser power of about 1 mW, however, the intermediate frequency (IF) signal power is increased by about five orders of magnitude [$P_{IF} \propto \sqrt{P_{LO}P_s} = \sqrt{10^{-13} \times 10^{-3}}$ W = 10^{-8} W >> 10^{-13} W (P_s)] and the signal to noise ratio reaches 10^4 considering only the noise from the hopping conduction.

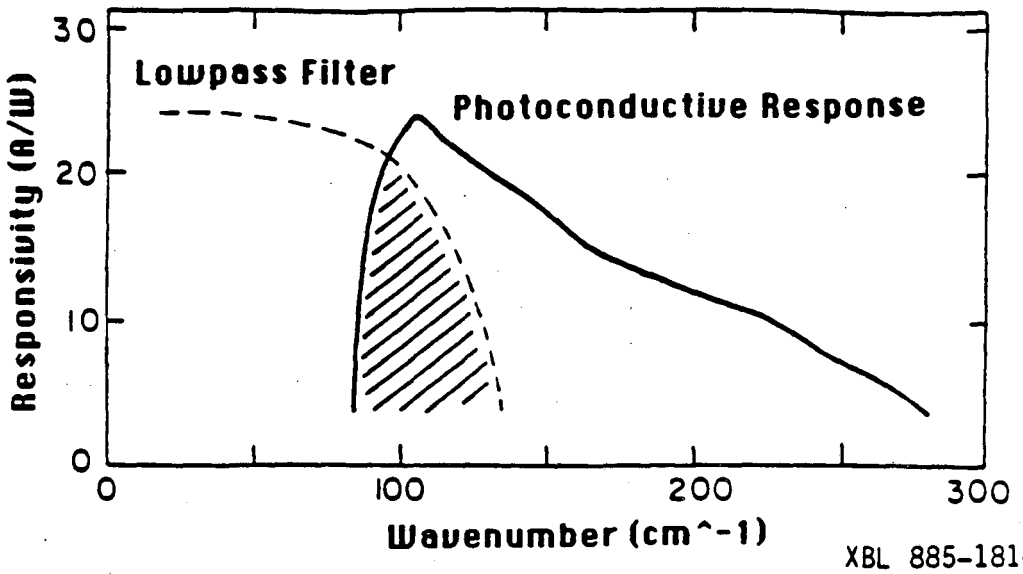

Fig. 7.8 Schematic showing the spectral range of incident radiation in the measurement of 22-series photoconductors.

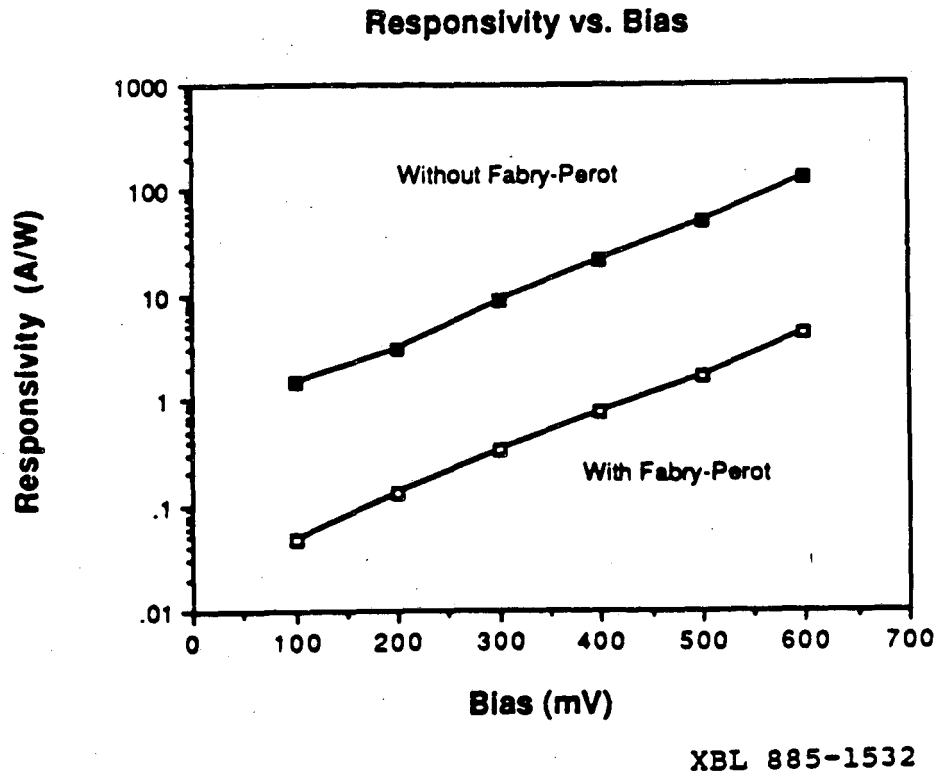

Fig. 7.9 Responsivity of detector 729-6.0(20) (with Fabry-Perot) and the increase of output signal of the same detector by removing the Fabry-Perot filter.

7.3.2 Heterodyne Measurements

The heterodyne measurement was performed in colaboration with Drs. D. M. Watson and E. N. Grossman at the California Institute of Technology [114]. Photoconductive gain and carrier lifetime for each detector was measured with the use of a far-infrared heterodyne receiver. This device, illustrated in Fig. 7.10, is described in detail elsewhere [115]. Briefly, the receiver consists of a photoconductor, a 80 μm lowpass filter and a low-noise 1 ~ 100 MHz GaAsFET amplifier mounted in a liquid helium dewar. Local oscillator power is provided by a far-infrared laser sideband generator, in which the output of an optically-pumped far-infrared molecular laser is coupled to an ultra-low-capacitance GaAs Schottky diode via a long-wire antenna and a corner-cube reflector. Tunable radio-frequency power is also injected into the Schottky diode, with the result that the diode and antenna reradiate all of the mixing products of the two frequencies, including two sidebands separated from the laser line frequency by the radio frequency. Normally, one of these tunable sidebands is selected by a polarizing Michelson interferometer - Fabry-Perot interferometer combination to serve as the local oscillator. For this experiment, however, tunable low-frequency (1 ~ 100 MHz) sidebands on the 118.8 μm line of methanol were generated with the Fabry-Perot removed and the polarizing Michelson tuned to zero path difference. The detector was thus illuminated with sidebands and laser carrier, the latter having sufficient power to drive the detector impedance low enough that the

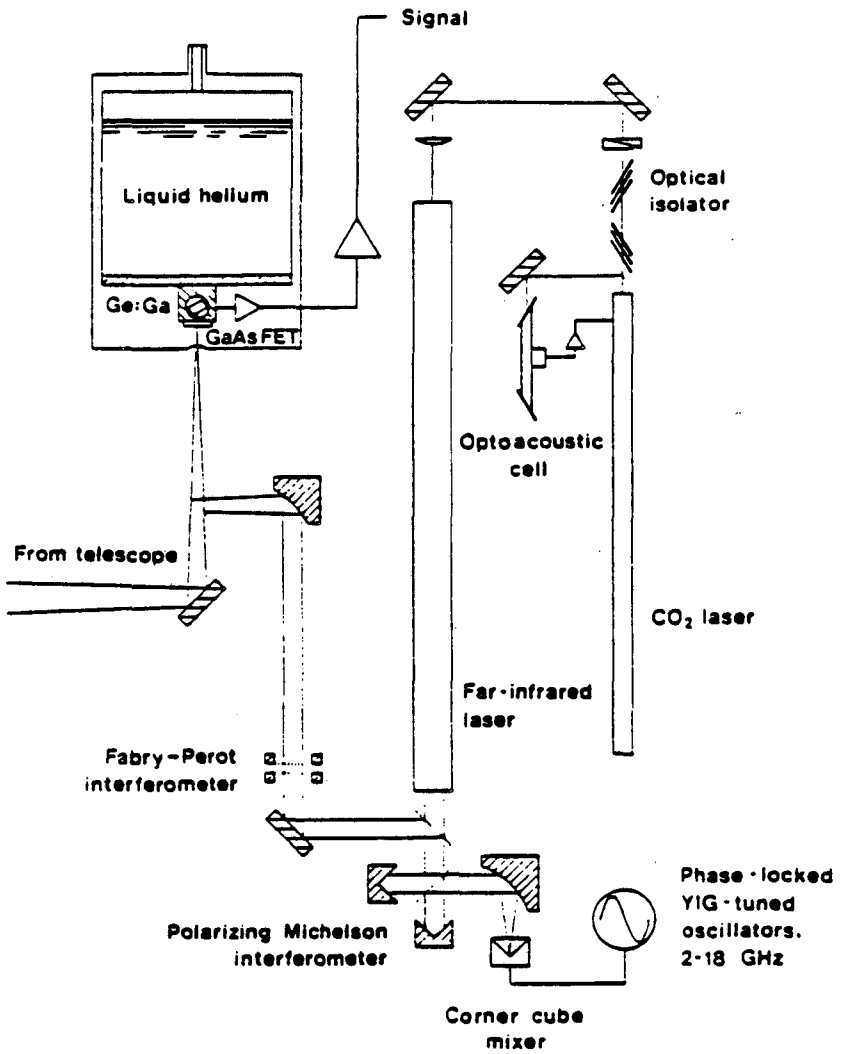

Fig. 7.10 Setup for heterodyne measurement.

critical frequency for $1/2\pi RC$ was higher than all other frequencies of interest. The rolloff of the photo-detected beat signal as a function of Schottky diode drive frequency thus gives the carrier lifetime τ directly: $\tau = 2\pi/\nu_c$, where ν_c is the frequency at which the beat power is lowered by 3 dB than its power at low frequencies. By illuminating the detector with unmodulated laser light, the noise caused by photo-generation and recombination of holes ("G-R" noise) was also observed. The rolloff of the G-R noise provides another measure of the carrier lifetime. Lifetimes determined by these two methods were found to be identical. Derivation of the photoconductive gain from these data follow either from $G = \tau/t$, where $t = L/\mu E$ is the hole transit time, or from the low-frequency G-R noise via $P_{G-R} = 4GeI_{DC}RB$, where I_{DC} is the detected photocurrent, R is the detector impedance, and B is the bandwidth of the measurement. Using derived values of G, the quantum efficiency η is obtained from the current responsivity.

It is ambiguous to distinguish the low-frequency region from rolloff region in the measured power spectrum. Therefore, it was difficult to find the -3 dB point in the signal power vs. IF frequency plot. The recombination time of carriers were obtained by obtaining a best Lorentzian fit of the measured power spectrum. Figure 7.11 shows the method of Lorentzian fit used to get the recombination bandwidth and photoconductive gain in heterodyne measurement.

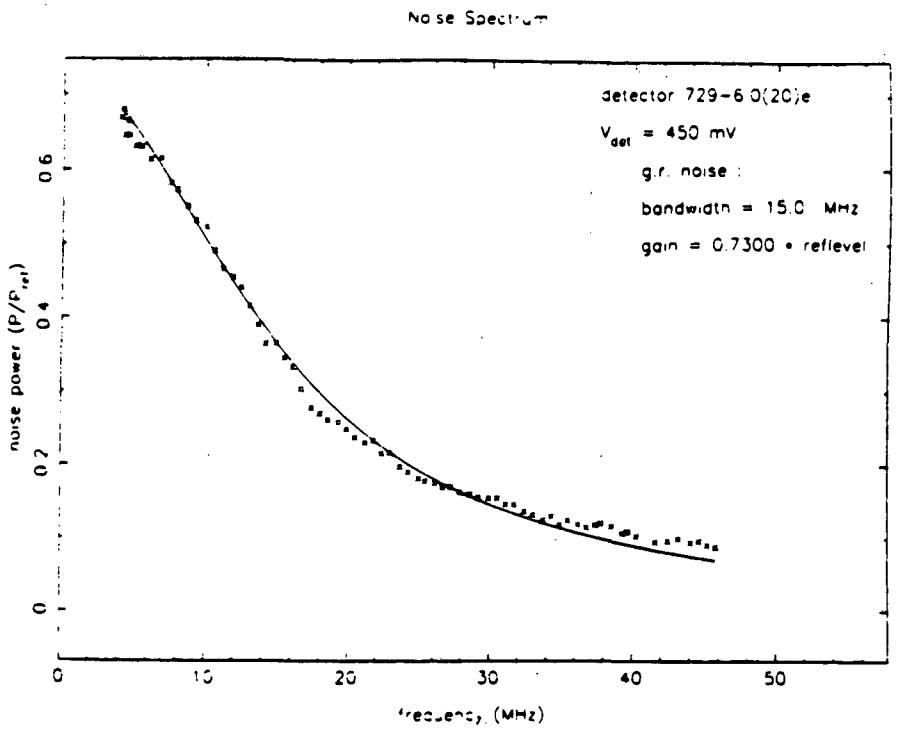

XBL 885-1666

Fig. 7.11 Example of Lorentzian fit of measured signal power vs. IF frequency.

7.4 Discussion of Results

Four separate experiments were carried out to determine the fundamental device parameters, quantum efficiency, photoconductive gain, and carrier lifetime in each photoconductor. In all cases, the detectors were mounted in cylindrical integrating cavities and were held at 4.2 K.

Figure 7.12 shows the result of modulation bandwidth vs. bias field for detector 496-5.5. The indicated error bars are somewhat

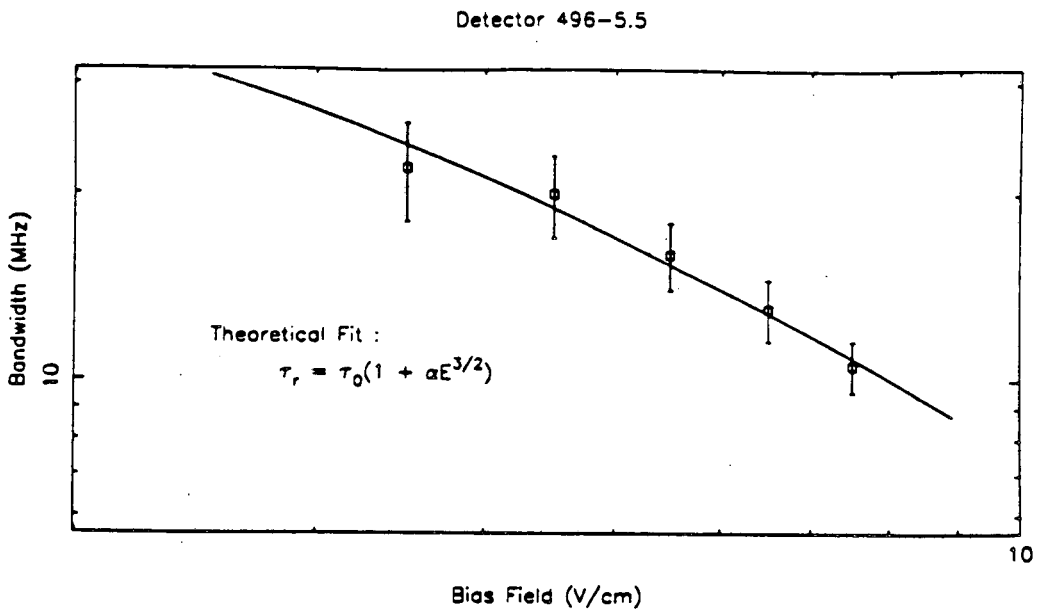

XBL 882-586

Fig. 7.12 Field dependence of the recombination bandwidth of detector 496-5.5(20).

conservative estimates of the range over which a good fit of the data to a single Lorentzian could be obtained. The rolloff in bandwidth at high bias is due to the reduction in recombination cross section that occurs as the carrier temperature T_h is elevated above the lattice temperature (hot carriers). A crude theoretical argument leads to the expectation that the recombination bandwidth should vary as $B \sim E^{-3/2}$ in the hot carrier regime and be independent of E in the thermalized regime. According to the original "giant trap" thoery of Lax [116], the recombination cross section varies with mean carrier kinetic energy U as $\sigma_r \sim U^{-2} \sim T_h^{-2} \sim v_T^{-4}$ (v_T is the

thermal carrier velocity). Thus, the recombination bandwidth is expected to vary as:

$$B = N_D \sigma_r v_T \sim N_D T_h^{-\frac{3}{2}} \tag{7.15}$$

where N_D is the concentration of ionized acceptors. In the thermalized (low bias) regime, T_h is equal to the lattice temperature, independent of field. In the hot carrier regime, the relation between v_T and bias field is given by equating the rate at which energy is imparted to the carriers by the bias field with the rate at which energy is lost via inelastic (i.e., acoustic phonon) collisions [117]. Thus:

$$eEv_d = (\frac{1}{2} m^* v_T^2)(\frac{v_T}{l_i}) \tag{7.16}$$

where l_i is the inelastic mean free path. The drift velocity v_d is limited by ionized impurity scattering (an elastic process) and is $\ll v_T$. It is given by the acceleration due to the field over an elastic scattering time:

$$v_d = \frac{eE}{m^*} (\frac{l_e}{v_T}) \tag{7.17}$$

Combining (7.16) and (7.17), one finds that $v_T \sim E^{1/2}$, or $T_h \sim E$. Thus, from equation (7.15), the theoretical expectation is that $B \sim E^{-3/2}$ in the hot carrier regime, and is independent of E in the

thermalized regime.

As shown in Fig. 7.12, such a dependence fits our data very well. One of the main reason for our wanting to determine the dependence of bandwidth on bias is to be able to normalize $B(N_D)$, the bandwidth vs. compensating impurity concentration, to a single value of E/E_{br}. Physically, the bandwidth in the low bias limit, where the carriers are thermalized, would be the most fundamental quantity to examine. However, the low bias limit is not the regime in which the photoconductors are used in practical applications, nor is it a region in which we can, with our techniques, measure the bandwidth with any accuracy (In both cases, the responsivity is too low). Therefore, we have normalized all our bandwidth measurements to a bias $E = 0.8E_{br}$ using the empirical approximation of $B \sim E^{-1}$ described above. The bandwidths were actually measured at biases that varied from about 0.7 to 0.95 times the breakdown field, so this normalization never amounted to more than about a 15% correction. the results of our measurements, using both the modulation and the G-R noise techniques, are shown in Fig. 7.13. It is clear that the two techniques employed to measure the bandwidth agree fairly well. The series 22 detectors have the highest bandwidth of all the detectors we have measured. As expected from equation (7.15), there is an approximately linear relation between bandwidth and donor (compensating impurity) concentration. The slope of the relation is a measure of the recombination cross section:

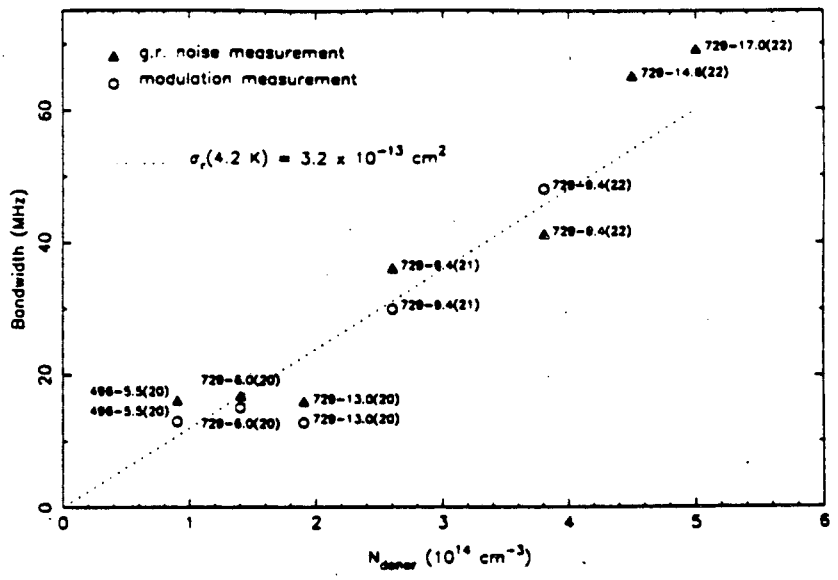

XBL 882-587

Fig. 7.13 Measured recombination of detectors.

$$\sigma_r = \frac{B(N_D)}{N_D v_T} = \frac{B(N_D)}{N_D} \left(\frac{3kT_h}{m^*}\right)^{\frac{1}{2}} \tag{7.18}$$

Taking $T_h = 4.2$ K we obtain $\sigma_r = 3.2 \times 10^{-13}$ cm^2. This is a slight overestimate of the cross section at the true carrier temperature [because of the $T_h^{1/2}$ conversion factor in equation (7.18)] but an underestimate of the cross section at 4.2 K (because of the steep rolloff of cross section with temperature). Based on the

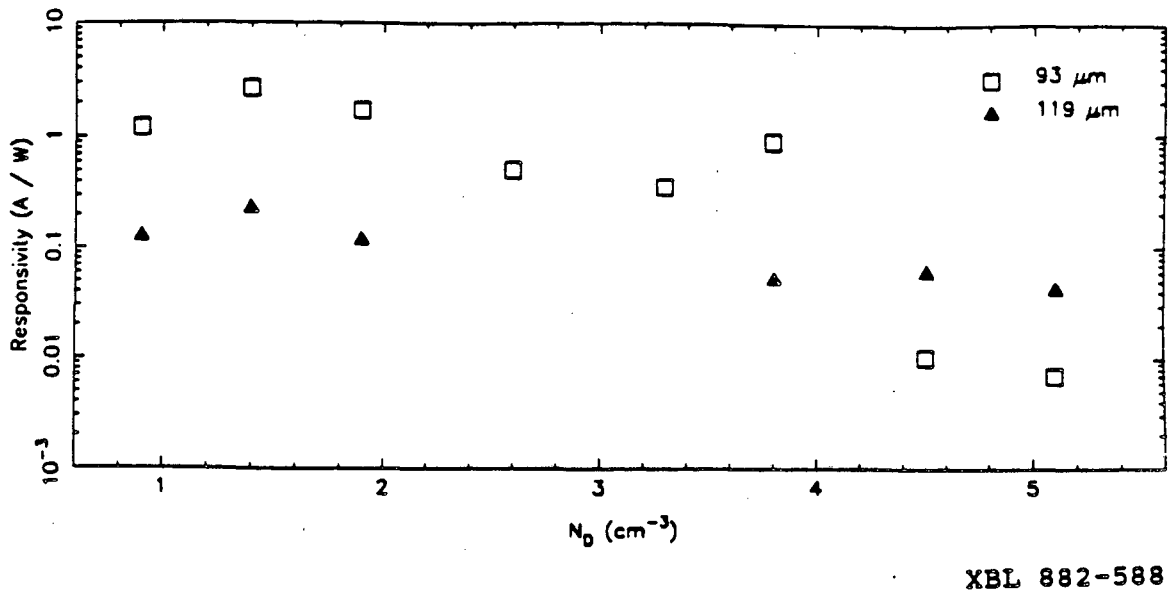

Fig. 7.14 Measured responsivity values at 93 μm and 119 μm.

measured bias dependence of bandwidth in Fig. 7.13, we do not expect the bandwidth, and therefore σ_r, in the thermalized regime (i.e., at 4.2 K) to be more than perhaps a factor of two greater than our present determination, however. Comparing with the theories discussed earlier, it is clear that our data favor the Brown and Rodriguez result [118]. However, to be fair, we note that since we do not know for certain the true carrier temperature in our experiments, the extremely steep dependence of σ_r on temperature may be used to make any of the theories fit the measured cross section.

Figure 7.14 shows the 93 μm and 119 μm responsivity measurements, The plotted values were measured at slightly different bias from 0.7 to 0.95 times the breakdown voltage of the various respective

detectors. The 93 μm measurements show a steep falloff in responsivity as N_D is increased. If n is approximately the same for all the detectors at 93 μm (since this is well shortward of the photoconductive edge in germanium), then this falloff reflects the decline in photoconductive gain at high compensating impurity concentration. Such a decline is expected, partly due to the reduced recombination lifetime, and partly due to increased ionized impurity scattering and therefore reduced carrier mobility. Our measured Hall mobilities indeed show such a decline, falling from 2.5×10^4 $cm^2/Vsec$ for detector 729-6.0(20) to 3000 $cm^2/Vsec$ for 729-14.6(21). The 119 μm responsivities also show a falloff at high doping concentrations, but it is not nearly such a steep one as that of the 93 μm responsivities. This may be understood in terms of impurity wavefunction overlap at high doping concentrations, whose existence is implied by the existence of significant dark currents. Evidently, as the doping level is raised, the photoconductive gain falls off as indicated by the 93 μm responsivity, but an increase in quantum efficiency due to broadening of the photoconductive edge partially compensates for this, so that the falloff in 119 μm responsivity is not so steep. As mentioned earlier, the absolute value of the 119 μm responsivity is highly uncertain due to the pyroelectric detector's absolute calibration. Therefore, even though some of our measurements apparently indicate that S(93 μm) > S(119 μm), these measurements do not affect this interpretation.

The photoconductive gains we have derived from the amplitude of the G-R noise are shown in Table 7.3. As discussed earlier, they are

subject to significant uncertainties that do not affect our other data. The typical values, in the range of 0.01 ~ 0.03, are more than an order of magnitude lower than those of typical detectors optimized for direct detection. In addition, there is a decline in measured photoconductive gain with increasing N_D, but it is not nearly as fast as that of the 93 μm responsivity, which, as discussed above, should track G. Indeed, the rolloff in the measured G is, at the level of uncertainty in the data, no faster than that of S(119 μm). This discrepancy in the rate at which G and S(93 μm) decline with N_D is the basic inconsistency between our different sets of data. It depends heavily on the measured 93 μm responsivities of the two most highly doped (22 series) detectors. As discussed earlier, these are

Table 7.3

Photoconductive Gain Derived from G-R Noise

Detector	(nsec)	E_{bias}(V/cm)	$G_m = (i^2)/4ei_{DC}$
496-5.5(20)	10.0	5.5	.021
729-6.0(20)	11.4	9.8	.032
729-13.0(20)	9.36	15	.028
729-9.4(21)	4.30	12	.025
729-9.4(22)	3.20	18	.022
729-14.6(22)	2.65	20	.015
729-17.0(22)	2.65	25	.014

more uncertain than the other 93 μm responsivities because they were measured in a more poorly characterized configuration, without the Fabry-Perot narrowband filter. In sum, although there is clearly a rolloff in photoconductive gain, and therefore in responsivity, with increasing concentration of compensating impurities, our data are ambiguous regarding how fast the rolloff is.

8. Summary and Conclusions

NTD germanium is used as a material for cryogenic bolometers because of its unique characteristics: uniform distribution of dopant impurities and reproducibility with same compensation ratio regradless of the doping concentration. Bolometers made of NTD germanium in LBL have been used in many areas and have shown excellent performances. Our resistivity data of NTD germanium in the hopping conduction range showed that the resistivity depends upon temperature as $\rho = \rho_0 \exp(-\Delta/T)^2$ in accordance with the theoretical prediction of Efros and Shklovskii. However, we cannot rule out the possibility of other temperature dependences of resistivity because our measurements were performed for the concentration variations of one order of magnitude ($10^{16} \sim 10^{17}$ cm^{-3}) and for a fixed compensation ratio of 0.32. Impurity conduction mechanism in highly-doped, highly-compensated semiconductors can be further understood by having data of samples with different compensation ratios and with large variation of doping concentrations.

NTD germanium has also been applied in the development of FIR

heterodyne mixers. A n-type germanium single crystal was grown and NTD technique was used to add more acceptors (gallium) into several slices of n-type single crystal. As a result of NTD, we obtained three series of detectors with each series having a fixed acceptor concentration and varying donor (compensating impurity) concentraions. Ge:Ga photoconductive mixers with recombination bandwidths as high as 60 MHz have been directly measured. The dependence of bandwidth on bias field of 496-5.5(20) detector is consistent with previous measurements of very lightly doped n-type material, and with theoretical expectations for the recombination cross section in the hot-carrier regime. At a given fraction of breakdown voltage (corresponding in practice to a normal operating point) mixer bandwidth varies approximately linearly with the concentration of compensating donors, regradless of the concentration of acceptors. The slope of the relation yields a recombination cross section of σ_r (4.2 K) = 3.2×10^{-13} cm^2. There is a marked rolloff in photoconductive gain and responsivity at higher impurity concentrations.

These results indicate that Ge:Ga mixers can be fabricated with relatively large bandwidths. The increased bandwidth is obtained at the expense of lower photoconductive gain and responsivity, however. In heterodyne applications, the LO power required in order to obtain ideal performance (i.e., LO induced G-R noise greater than other instrumental sources of noise) increases with the square of photoconductive gain. Thus, increased bandwidth is obtained at the price of greater required LO power. Optimization of a heterodyne

system thus involves a compromise between desired bandwidth and available LO power.

References

1. H. M. Janus, "Neutron Transmutation Doping in Semiconductors", J. M. Meese, ed., p37, Plenum Press, New York (1979)
2. H. Fritzsche and M. Cuevas, Phy. Rev. 119, 1238 (1960)
3. E. E. Haller, N. M. Haegel, and I. S. Park, "Proc. of the 2nd Infrared Detector Technology Workshop", NASA Ames, CA (1985)
4. A. Lange, E. Kreysa, S. E. McBride, P. L. Richards, and E. E. Haller, Int. J. IR and MM Waves 4, 689 (1983)
5. I. S. Park, E. E. Haller, E. N. Grossman, and D. M. Watson, submitted to Appl. Opt.
6. I. S. Park, E. E. Haller, and D. M. Watson, in preparation
7. I. S. Park and E. E. Haller, submitted to J. Appl. Phys.
8. see, for exapmle, "Radiation Defects in Semiconductors", F. L. Vook, ed., Plenum Press, New York (1968)
9. C. Kittel and A. H. Mitchel, Phys. Rev. 96, 1488 (1954)
10. J. M. Luttinger and W. Kohn, Phys. Rev. 97, 869 (1955)
11. N. O. Lipari and A. Baldereschi, Solid State Comm. 25, 665 (1978)
12. A. Baldereschi and N. O. Lipari, "Physics of Semiconductors", F. O. Fumi, ed., p595, Proc. of the 13th Int. Conf., Rome (1976)
13. J. H. Reuszer and F. Pisher, Phys. Rev. 135, A1125 (1965)
14. E. E. Haller and W. L. Hansen, Silid State Comm. 15, 687 (1974)
15. P. J. Price, Phys. Rev. 104, 1223 (1956)
16. W. Kohn and J. M. Luttinger, Phy. Rev. 98, 915 (1955)
17. R. A. Faulkner, Phys. Rev. 184, 713 (1969)
18. S. T. Pantelides, Rev. of Modern Phys. 50, 797 (1978)

19. A. K. Ramdas and S. Rodriguez, Rep. Prog. Phys. 44, 1298 (1944)

20. J. W. Cleland, K. Lark-Horovitz, and J. C. Pigg, Phys. Rev. 78, 814 (1950)

21. N. P. Palaio, S. J. Pearton, and E. E. Haller, J. Appl. Phys. 55, 1437 (1984)

22. K. Kuriyama, M. Yahagi, K. Iwamura, Y. Kim, and C. Kim, J. Appl. Phys. 54, 673 (1983)

23. J. M. Meese, "Neutron Transmutation Doping in Semiconductors", J. M. Meese, ed., pl, Plenum Press, New York (1979)

24. Handbook on Nuclear Physics [in Russian], Fizmatgiz, Moscow, 257 (1963)

25. H. C. Thomas and B. Covington, J. Appl. Phys. 46, 4541 (1975)

26. Table of isotopes, 7th ed. (1978)

27. Table of isotopes, 6th ed. (1967)

28. "Neutron Cross Sections", BNL-325. 2nd ed., No. 2 (1966)

29. H. C. Schweinler, J. Appl. Phys. 30, 1126 (1959)

30. S. F. Mughabghab and D. I. Garber, Nuetron Cross Sections, 1, Brookhaven National Laboratory, Long Island, New York, 325 (1973)

31. K. Lark-Horovitz, Proc. Intern. Conf. on Semi-Conducting Marerials, p47, Reading, England, 1950, Butterworths, London (1951)

32. A. G. Beda, V. V. Vainberg, F. M. Vorobkalo, and L. I. Zarubin, Sov. Phys. Semicond. 15, 916 (1981)

33. B. R. Gossick, J. Appl. Phys. 30, 1214 (1959)

34. B. R. Gossick and J. H. Crawford, Jr., Bull. Am. Phys. Soc. 3, 400 (1958)

35. J. H. Crawford, Jr. and J. W. Cleland, J. Appl. Phys. 30, 1204 (1959)

36. J. R. Parsons, R. W. Ballufi, and J. S. Koehler, Appl. Phys. Lett. 1, 57 (1962)

37. R. E. Whan, Phys. Rev. 140, A690 (1965)

38. J. A. Baldwin, J. Appl. Phys. 36, 793 (1965)

39. G. D. Watkins and J. W. Corbett, Phys. Rev. 134, A1359 (1964)

40. W. L. Brown, W. M. Augustyniak, and T. R. Waite, J. Appl. Phys. 30, 1258 (1959)

41. H. Saito and J. C. Pigg, Bull. Am. Phys. Soc. 9, 654 (1964)

42. J. C. Pigg and J. H. Crawford, Jr., Phys. Rev. 135, A1141 (1964)

43. T. A. Callcott and J. W. Mackay, Phys. Rev. 161, 698 (1967)

44. T. V. Mashovetz and V. V. Emtsev, "Lattice Defects in Semiconductors", p103, The Institute of Physics, London and Bristol (1974)

45. E. I. Blount, J. Appl. Phys. 30, 1218 (1959)

46. V. Nagesh and J. W. Farmer, to be published in J. Appl. Phys. 1988

47. C. A. Klein, J. Appl. Phys. 30, 1222 (1959) or ref. 35

48. F. L. Vook, Phys. Rev. 138, A1234 (1965)

49. A. V. Vasil'ev, S. A. Smagulova, and L. S. Smirnov, Sov. Phys. Semicond. 20, 354 (1986)

50. U. Gosele, F. Morehead, W. Frank, and A. Seeger, Appl. Phys. Lett. 38, 157 (1981)

51. V. V. Emtzev, T. V. Mashovetz, and S. M. Ryvkin, "Defects in Semiconductors", p17, The Institute of Physics (1972)

52. R. E. Whan, J. Appl. Phys. 37, 2435 (1966)

53. K. Seeger, "Semiconductor Physics", Springer-Verlag, 3rd ed., New York, 1985

54. J. H. Yee, S. P. Swierkowski, G. A. Armantrout, and R. Wichner, J. Appl. Phys. 45, 3949 (1974)

55. A. C. Beer and R. K. Willardson, Phys. Rev. 110, 1286 (1958)

56. L. J. Van der Pauw, Phillips Res. Reports, 13, 1 (1958)

57. D. Halliday and R. Resnick, "Phyiscs II", p869, John Wiley and Sons, Inc., New York (1962)

58. T. Germer, B.S. Thesis, University of California, Berkeley, 1986

59. M. van de Steeg, H. Jongbloets, and P. Wyder, Phys. Rev. Lett. 50, 1234 (1983)

60. E. E. Haller, W. L. Hansen and F. S. Goulding, Adv. in Phys. 30, 93 (1981)

61. R. J. Jones and P. Fisher, J. Phys. Chem. Solids, 26, 1125 (1965)

62. R. J. Bell, "Introduction to Fourier Transform Spectroscopy", Academic Press, New York (1972)

63. J. M. Kahn, Ph.D. Thesis, University of California, Berkeley, 1987

64. R. Winston, J. Opt. Soc. Am. 60, 245 (1970)

65. Y. Yamada, A. Mitsuishi, and H. Yoshinaga, J. Opt. Soc. Am. 52, 17 (1962)

66. K. Sakai, Y. Nakagawa, and H. Yoshinaga, Jap. J. Appl. Phys. 7, 792 (1968)

67. A. G. Kazanskii, P. L. Richards, and E. E. Haller, Appl. Phys. Lett. 31, 496 (1977)

68. B. O. Kolbesen, Appl. Phys. Lett. 27, 353 (1975)

69. D. V. Lang, J. Appl. Phys. 45, 3022 (1974)

70. E. E. Haller, P. P. Li, G. S. Hubbard, and W. L. Hansen, IEEE Trans. Nucl. Sci. NS-26, 265 (1979)

71. S. J. Pearton, Solid State Electronics 25, 499 (1982)

72. A. G. Zabrodskii, JETP Lett. 33, 243 (1981)

73. T. Lim, Berkeley Research Reactor, Berkeley, CA

74. Berkeley Research Reactor has ceased its operation in Dec. 1987

75. H. H. Woodbury and W. W. Tyler, Phys. Rev. 105, 84 (1957)

76. S. M. Sze, "Physics of Semiconductor Devices", 2nd ed., p27, John Wiley and Sons, inc., New York, (1981)

77. J. I. Pancove, "Optical Processes in Semiconductors", p93, Dover, New York (1971)

78. J. Bourgoin and M. Lannoo, "Point Defects in Semiconductors II", Springer-Verlag, New York (1983)

79. G. D. Watkins, "Lattice Defects in Semiconductors", F. A. Huntley ed., p1, The Institute of Physics, London and Bristol, (1974) or P. S. Gwozdz and J. S. Koehler, Phys. Rev. B6, 4571 (1972)

80. J. M. Kahn, L. M. Falicov and E. E. Haller, Phys. Rev. Lett. 57, 2077 (1986)

81. R. E. McMurray, Jr., N. M. Haegel, J. M. Kahn and E. E. Haller, Solid State Comm. 61, 27 (1987)

82. N. Fukuoka and H. Saito, Physica 116B, 343 (1983)

83. N. Fukuoka and H. Saito, Jap. J. Appl. Phys. 21, 930 (1982)

84. P. M. Mooney, M. Cherki and J. C. Bourgoin, J. Phys. Lett. 40, L-19 (1979)

85. N. Fukuoka and H. Saito, Jap. J. Appl. Phys. 20, L519 (1981).

86. W. Hershel, Phil. Trans. R. Soc. 90, 284 (1800)

87. S. P. Langley, Inf. Phys. 3, 195 (1963)

88. F. J. Low, J. Opt. Soc. Am. 51, 1300 (1961)

89. J. Clarke, G. I. Hoffer, and P. L. Richards, Revue de Physique Appliquee 9, 69 (1974)

90. D. H. Andrews, R. M. Milton, and W. DeSorbo, J. Opt. Soc. Amer. 36, 518 (1946)

91. E. E. Haller, Inf. Phys. 25, 257 (1985)

92. J. Farmer, University of Missouri Research Reactor Facility, Columbia, MO

93. Y. Kamiura and F. Hashimoto, Phys. Stat. Sol. 54, 697 (1979)

94. E. Kreysa, Max Planck Institute for Radioastronomy, Bonn, West Germany

95. P. Richards' group, Physics Department, University of California, Berkeley

96. Lake Shore Cryotronics, Inc., Westerville, Ohio

97. M. Rodder, M.S. Thesis, University of California, Berkeley

98. A. L. Efros and B. I. Shklovskii, J. Phys. C: Solid State Phys. 8, L49 (1975)

99. A. L. Efros, J. Phys. C: Solid State Phys. 9, 2021 (9176)

100. N. Wang, S. Davis, A. Lange, B. Sadoulet, T. Shutt, J. Beeman, E. Haller, I. Park, and R. Ross, presented at IEEE Nuclear Symphosium (Cryogenic Detectors), S.F., CA, 1987

101 A. Lange, S. Hayakawa, T. Matsumoto, H. Matsuo, H. Murakami, P. L. Richards, and S. Sato, Appl. Opt. 26, 1401 (1987)

102. A. Miller and E. Abrahams, Phys. Rev. 120, 745 (1960)

103. N. F. Mott, Phil. Mag. 19, 835 (1969)

104. F. H. Pollak, Phys. Rev. 138, A618 (1965)

105. V. Ambegaokar, B. I. Halperin and J. S. Langer, Phy. Rev. B4, 2612 (1971)

106. N. M. Haegel, M. R. Hueschen, and E. E. Haller, Inf. Phys. 25, 273 (1985)

107. M. C. Teich, Proc. IEEE 56, 37 (1968).

108. F. R. Arahms, E. W. Sard, B. J. Peyton, and F. P. Pace, IEEE J. QE 3(11), 484 (1967).

109. D. H. Seib, IEEE J. QE 10, 130 (1974).

110. P. L. Richards and L. T. Greenberg, Infrared Detectors for Low-Background Astronomy: Incoherent and Coherent Devices from One Micrometer to One Millimeter in "Infrared and Millimeter Waves", vol. 6, Academic Press, New York, (1982)

111. F. Rosengerger, "Fundamentals of Crystal Growth I", p427, Springer Verlag, New York (1979)

112. D. M. Watson, Ph.D. Thesis, University of California, Berkeley

113. B. I. Shklovskii and A. L. Efros, "Electronic Properties of Doped Semiconductors", Springer-Verlag, New York, (1984)

114. Physics Department, California Institute of Technology, CA.

115. E. N. Grossman, Ph. D. Thesis, California Institute of Technology, 1987

116. M. Lax, Phys. Rev. 119(5), 1502 (1960)

117. R. M. Westervelt and S. W. Teitsworth, J. Appl. Phys. 57(12), 5457 (1985)

118. R. A. Brown and S. Rodriguez, Phys. Rev. 153, 890 (1966)

LAWRENCE BERKELEY LABORATORY
TECHNICAL INFORMATION DEPARTMENT
UNIVERSITY OF CALIFORNIA
BERKELEY, CALIFORNIA 94720